University of Leeds
Department of Civil Engineering
Leeds, LS2 9JT

# Direct Numerical Simulation of Turbulent Open Channel Flow over Poly Disperse Particle bed

**Shahzad Sarwar**

A thesis submitted for the degree of
Doctor of Philosophy

The candidate confirms that the work submitted is his own and that appropriate credit has been given where reference has been made to the work of others

This copy has been supplied on the understanding that it is copyright material and that no quotation from the thesis may be published without proper acknowledgement.

The right of Shahzad Sarwar to be identified as Author of this work has been asserted by him in accordance with the Copyright, Designs and patents Act 1988.

©2021 The University of Leeds and Shahzad Sarwar

# Abstract

This thesis is a contribution towards a deeper understanding of turbulent open channel flow, sediment erosion and sediment transport. The thesis provides an analysis of high fidelity data from two different flow configurations, open channel flow over an array of fixed spheres and open channel flow with sediment transport of many mobile spheres. The data is generated by direct numerical simulation using an immersed boundary method to resolve the surface of fixed and mobile particles. The simulations provide a detailed picture of the flow field and particle related quantities. The results show, that simplified considerations of the relation of flow structures to force and torque on particles are useful to explain characteristics of the force and torque on particles. For the present flow configurations, the time and velocity scales of force and torque are of the order of outer flow units and the correlation of flow structures to force and torque fluctuations are of the order of the channel height. The onset of sediment erosion is discussed by the results of simulations with fixed and with mobile eroding spheres. Conditionally averaged flow fields and instantaneous flow structures related to the onset of sediment erosion agree with experimental findings from the literature. However, the prediction of the onset of sediment erosion by a critical Shields number based on instantaneous lift on a fixed sphere are not in line with the experimental evidence in the literature. An explanation of this discrepancy could be that this approach neglects possible collective effects. The few simulations with mobile particles indicate that such collective effects may play an important role at the given parameter range. Simulations of sediment transport reveal a strong influence of the mobile particles on the flow field statistics. It is found that the Rouse formula provides a good approximation of the obtained density profiles of the present cases, when the exponent of the original definition is reduced by 20% to 35%.

# Acknowledgement

My pursuit to understand the complex phenomena of particle entrainment has provided me the opportunity to create memories and build friendships that are more robust and less erodible than the mere particle beds I chase to understand.

It would be wrong of me not to list every single person who has contributed towards my PhD. Firstly, I would like to thank my supervisors, Professor Nigel Wright and Dr Peter Andrew Sleigh (Andy). I believe both would unanimously agree that I was the worst PhD student they ever supervised, and it is because of this I cannot thank both Professor Wright and Andy enough. To completely believe in me and my ability throughout and not give up. To both I am ever in-debt.

I would secondly like to thank all my University of Leeds colleagues, Bashir al Hadeethi, Dr David Dawson, Dr Amirul Khan and The ARC help desk team including John Hodrian, Mark Dixon and Martin Callahan for their underlying support and fun conversations throughout. I would like to thank Professor Simon Tait and Dr Andrew Nichols for their interesting discussions and experimental data.

I would like to express my gratitude to Professor Balachander, Dr Nadim Zgheib, Dr Georges Akkiki, David Zwick, Dr Goran Marjonavic, Dr Yash Mehta, Rahul and Miss Holly Starr for their hospitality and help throughout my time at the University of Florida. A special mention goes to Professor Balachander for his unrelenting support and contagious passion in my work.

Finally, I want to express my sincere gratitude and love to my mother, and also to my best friend, Dorothy Brazis. Your devoted support has been a cornerstone of my academic endeavor, and I am forever indebted to you. I would like to thank the late Hafiz Fateh for being the perfect role model. His selfless nature and guidance throughout my childhood provided me with the perfect guardian I could ever need.

In the end I would like to thank God and life for the opportunity to travel, learn and follow an erratic path in quest of my fascination. The reader of this thesis will not have any comprehension of the journey that this thesis has taken me on. It has been a privilege, although more often turbulent than many natural rivers, mainly due to my extremely undisciplined, irreverent manner and as a result I have learnt harsh lessons. If I could re-do this whole process again, I would repeat it in the same undisciplined and irreverent manner.

اِلَى وَالدتي لهبهَا لَا نهَاية له

*"Gone have the days when I used to*
*play with time, now time plays with me"*

---

Imam Ghazali

# Contents


**1 Introduction** 9
1.1 Background . . . 9
1.2 Research objectives . . . 10
1.3 Outline of the thesis . . . 10

**2 Literature Review** 13
2.1 Basic structure of open channel flow . . . 13
2.2 Mean velocity distribution . . . 14
2.2.1 Logarithmic layer . . . 14
2.2.2 Interfacial sublayer . . . 16
2.2.3 Bed origin in rough flow . . . 16
2.3 Flow over rough walls . . . 17
2.3.1 Particle Distribution . . . 17
2.3.2 Surface texture . . . 18
2.3.3 Particle arrangement and friction angle . . . 19
2.4 Hydrodynamic forces on fixed particles . . . 19
2.4.1 Effects of neighbouring particles . . . 22
2.5 Onset of sediment transport . . . 22
2.5.1 Sediment transport . . . 23
2.6 Outcome of literature review . . . 24

**3 Fundamentals** 25
3.1 Governing equations . . . 25
3.1.1 Continuum hypothesis and Navier-Stokes equation . . . 25
3.1.2 Boundary conditions and initial conditions . . . 26
3.2 Equations of the solid particle phase . . . 28
3.2.1 Equations of rigid-body motion . . . 28
3.2.2 Forces on a particles . . . 29
3.2.3 Torque on a particle . . . 30
3.2.4 Fluid and particle coupling . . . 30
3.3 Numerical simulation of turbulence and flow . . . 30
3.3.1 Turbulence in fluids . . . 31
3.3.2 Direct numerical simulation of turbulent flow . . . 31
3.3.3 Numerical method and validation . . . 33

**4 Open channel flow over fixed spheres at low relative submergence** 35
4.1 Numerical setup . . . 35
4.2 Flow field characteristics . . . 37
4.2.1 Flow field statistics . . . 37

4.2.2 Three-dimensional time averaged flow field distribution . . . . . 45
4.3 Statistics of particle force . . . . . 49
4.4 Statistics of particle torque . . . . . 54
4.5 Time scales of torque fluctuations on a particle . . . . . 59
4.6 Time scales of force fluctuations on a particle . . . . . 63
4.6.1 Time scales of cross-correlation between drag and lift fluctuations on a particle . . . . . 69
4.7 Summary, conclusion and recommendation for future work . . . . . 71

**5 Sediment transport in open channel flow at low relative submergence** 75
5.1 Numerical setup . . . . . 75
5.2 Results . . . . . 77
5.3 Summary, conclusion and recommendation for future work . . . . . 81

**6 Conclusions and future work** 85
6.1 Open channel flow over fixed spheres . . . . . 85
6.2 Sediment transport in open channel flow . . . . . 86
6.3 Recommendation of future work . . . . . 87

# List of Figures


2.1 Classification of different flow layers in a rough-bed open-channel (adapted from Nikora *et al.* (2001)). The sketch shows the definition of the flow depth measured between the free surface and the spatially averaged bed level, $H$; the flow depth above the roughness crests, $h$; and the roughness height, $\Delta$, used in the present study. Note also that the origin of the vertical coordinate in this study is fixed at the elevation of the roughness crests i.e. $z_c = 0$. . . . . 15

2.2 Schematic diagram illustrating the dependence of the pivoting angle ($\phi$) on the relationship between the diameter of the particle considered and that of the particle upon which it rests (Robert, 2003) . . . . . 20

4.1 Close-up of a section of the computational domain with the geometry of the bottom wall consisting of a layer of fixed randomly dispersed spheres: (a) case M1015; (b) case P800. . . . . 36

4.2 Side view of the instantaneous flow field in the case P800 at different times. . . . 38

4.3 Side view of the instantaneous flow field in the case M1015 at different times. . . 39

4.4 Two-point correlations $R_{uu}$, $R_{vv}$ and $R_{ww}$ of streamwsie and spanwise seperations 40

4.5 One-dimensional energy spectra in the spanwise $x$ and streamwise $y$ directions respectively. . . . . 41

4.6 Time and spatially averaged streamwise velocity component $\langle u \rangle$, of the case P800 and case M1015 in comparison with smooth wall open channel flow and Clemens *et al.* (2011). ($a$) Normailsed with $U_{bh}$ as a function of $(z - z_0)/h$, ($b$) in semi logarithmic scale normalised by $u_\tau$. The position of the particles top are marked with horizontal ($a$) dot and dashed line. . . . . 43

4.7 Roughness function for several transitionally rough surfaces as a function of the Reynolds number $k^+_{s\infty}$, adapted from Jimeńez (2004). . . . . 44

4.8 (a) Root-mean-square of velocity fluctuations of case M1015 and case P800 normalised by $u_\tau$ in comparison with results of Clemens *et al.* (2011) as a function of wall distance. (b) Distribution of Reynolds shear stress $u'v'$ as a function of wall distance. . . . . 46

4.9 Root-mean-square of velocity fluctuations of case M1015 and case P800 normalised by $u_\tau$ in comparison with results of Clemens *et al.* (2011) as a function of wall distance. . . . . 47

4.10 Distribution of the time averaged streamwise velocity, $\langle u \rangle$, normalised by $u_\tau$ in $z - x$ planes for the case P800 (a) and case M1015 (b). Plane through particles and not particle centres. . . . . 48

4.11 Sketch illustrating the definition of force $F_x, F_y, F_z$ and $T_x, T_y, T_z$ on a particle. . 50

4.12 Cumulative function $\ell_\phi$ of the stress contribution to the mean value of drag, lift and spanwise torque on a particle as in case M1015(a) and case P800(b) a function of $z/D$ and normalised by its maximum value, $\ell_\phi(D)$ . . . . . 52

4.13 Comparison of $\langle F_y \rangle / (\rho f \nu^2)$ as a function of $D^+$ of case M1015 and case P800 with mean lift on a sphere placed between roughness elements in a boundary layer. Here $D_r$ is the diameter of rods spaced with $D_r$ upstream and downstream of a sphere with diameter $D$. . . . . 53

4.14 Normalised probability density functions of force fluctuations in case M1015 (a) and case P800 (b). . . . . 55

4.15 Root-mean-square value (a) and kurtosis (b) of force and torque obtained from the simple model described in the text and of actual values of the corresponding torque obtained on the particles in case M1015 and P800. . . . . 58

4.16 Normalised pdfs of the quantities for which statistical moments have been shown in figure 4.15.(a,c) Case M1015 compared to simple model with $s^+ = 12$. (b,d) Case P800 compared to simple model with $s^+ = 52$. . . . . 60

4.17 Normalised pdfs of the quantities for which statistical moments have been shown in figure 4.15.(a,c) Case M1015 compared to simple model with $s^+ = 12$. (b,d) Case P800 compared to simple model with $s^+ = 52$. . . . . 61

4.18 Auto-correlation of, $R_{\phi\phi}(\tau)/\sigma_\phi^2$, of particle torque fluctuation as a function of time lag, $\nu/u_\tau^2$. The panels show the results of (a) streamwise torque fluctuation, $T_y'$, (b) wall-normal torque fluctuation, $T_z'$, and (c) spanwise torque fluctuation, $T_x'$. The smooth wall case reference is from Clemens *et al.* (2011). . . 62

4.19 Pre-multiplied spectra $\omega \hat{R}_{\phi\phi}$ of particle torque fluctuations as a function of period $\mathscr{T} u_\tau^2/\nu$. Spectra are normalised by $\mathscr{A}$ as defined in the text. . . . . 64

4.20 Auto-correlation, $R_{\phi\phi}(\tau)/\sigma_\phi^2$, of particle force fluctuation as a function of time lag, $\tau U_{bh}/h$. The panels show results of (a) drag fluctuation, $F_y'$, (b) lift fluctuation, $F_z'$, and (c) spanwise force fluctuations, $F_x'$. . . . . 66

4.21 Pre-multiplied spectra $\omega \hat{R}_{\phi\phi}/\mathscr{A}$ of particle force fluctuations as a function of period $\mathscr{T} U_{bh}/h$. Spectra are normalised by $\mathscr{A}$ as defined in the text. The solid line is M1015 and the dashed line represents the P800 case . . . . . 68

4.22 Cross-correlation of drag and lift fluctuation, $R_{FxFx}(\tau)/(\sigma_{Fx}\sigma_{Fx})$, as a function of time lag $\tau h/U_{bh}$. Figure shows the results of the case M1015 and case P800 in comparison with Hofland *et al.* (2005) and Dwivedi *et al.* (2010) . . . . . 69

5.1 Snapshot of mobile particles in turbulent channel flow . . . . . 77

5.2 Shields parameter $\theta_s$ in simulations of table 5.1 as function of particle diameter in viscous units $D^+$. . . . . 78

5.3 Wall-normal position of particle centres, $y_p(t)$, of mobile particles in case S10L3, (a) as a function of time $(t - t_0)U_{bh}/h$, (b) as a function of streamwise distance from initial position, $(x_p(t) - x_p(t_0))/h$. Here, $t_0$ is the initial time of the simulations and $x_p(t_0) = (x_p(t_0), y_p(t_0), z_p(t_0)$ the initial position of a particle. Dashed lines are introduced to guide the eye and show location of $y = 1.5D$ which is the location of a particle centre positioned on top of a particle with $y_p = D/2$. . . . . 79

5.4 Time signals of mobile particles in case S10L3. (a) Wall-normal particle position, $y_p/D$, (b) wall-normal particle velocity, $/nu_p/u_\tau$ and (c) spanwise angular velocity, $/u_tau$. Time signals are shown as a function of $(t - t_{thres}U_{bh}/h$ where $t_{thres}$ is chosen as the time the respective particle reaches a wall-normal position of 1.5D, i.e., $y_p(t_{thres}) = 1.5D$. . . . . 80

# List of Tables


4.1 Parameters for the two simulations. $U_{bH}$ denotes the bulk velocity based on the domain height $H$, $u_\tau$ is the friction velocity, $Re_b = U_{bH}H/\nu$ is the bulk Reynolds number with the kinematic viscosity $\nu$, $Re_\tau = u_\tau h/\nu$ is the friction Reynolds number, $D^+ = Du_\tau/\nu$ is the particle diameter in viscous units, $D/\Delta_x$ is the resolution of a particle, $\Delta_x^+$ is the grid spacing in viscous units, $N_x$, $N_y$ and $N_z$ denote the number of grid points in the spanwise, streamwise and wall-normal directions, $N_p$ is the total number of particles in the disperse distribution . . . . . 36

4.2 Statistics of force on particles in case M1015 and case P800, where $C_{Fi} = \langle F_i/F_R \rangle$ is the normalised mean force component in the $x_i$-direction, $\alpha = arctan(C_{Fy}/C_{Fx})$ is the angle of the resulting force with respect to the $x$-axis, $\sigma_{Fi}$ is the standard deviation of the force in $x_i$, $S_{Fi}$ and $K_{Fi}$ are the skewness and kurtosis of the respective force component. . . . . 49

4.3 Statistics of torque on particles in case M1015 and P800. $C_{Ti} = \langle T_i \rangle / T_R$ is the normalised mean torque component in the $x_i$-direction, $\sigma_{Ti}$ is the standard deviation of the torque in $x_i$ direction, $S_{Ti}$ and $K_{Ti}$ are the skewness and kurtosis of the respective torque component. . . . . 54

4.4 Time scales of force fluctuations on a particle in case M1015 and P800 normalised by $h/U_{bh}$. Considered time scales are the micro time scale, $m$, the integral time scale, $\ell$, and the time-lag related to the first local minimum $min$. . . 63

4.5 Period of local maximum in pre-multiplied spectra of force fluctuations, $\mathscr{T}_{max}$, normalised by outer flow time scale, $U_{bh/h}$. . . . . 67

4.6 Difference of time-lag related to maximum and minimum in cross correlation of drag and lift, $\tau_\Delta$, in case M1015 and P800. The difference is normalised by various time scales and compared to the value obtained from the results of Hofland *et al.* (2005) (HOF05) and Dwivedi *et al.* (2010)(DWI10). . . . . 70

5.1 Parameter of simulations to study the onset of single particle (S) and multiple particle (M) erosion. The setup is analogously to that of case M1015 and case P800 introduced in chapter 4. However here, $N_p^f$ particles are mobile and able to erode from the initial bed configuration. The ratio of particle density and fluid density is $\rho_p/\rho_f$, two ratio were considered a low value (L) of $\rho_p/\rho_f = 1.25$ and a somewhat higher value (H) of $\rho_p/\rho_f = 1.7$, $gh/U_{bh}^2$ is the normalised gravitational volume force $\theta_s$ is the Shields parameter defined by 2.2, $\tau_c U_{bH}/H$ is the total observation time of the simulation, the last column indicates whether or not particle erosion occurred. . . . . 76

*"The thing is to understand myself, to see what God really wishes me to do; the thing is to find a truth which is true for me to find the idea for which I can live and die"*

Soren Kierkegaard (1813–1855)

# 1 Introduction

## 1.1 Background

The process of sediment entrainment and sediment transport is an important fluvial geomorphic process in alluvial channels. The prediction of bed-load transport becomes an important issue, which is especially true for many processes in environmental as well as process engineering, where the design of vital infrastructure such as bridge piers, sewage or pipeline systems has to account for the nature of these flows. The ability of a river to modify the morphological characteristics of the channel in turn depends on the balance between the erosional force exerted by the river flow and the strength or resistance to entrainment of the material forming the bed. Other applications of processes involving sediment entrainment can be found in aeolian transport (dune formations), in the chemical industry (pneumatic conveying) and in biological systems (blood flow through the respiratory system).

Despite the importance of sediment entrainment in the diverse applicatory disciplines the fundamental aspects involved remains an open question. At the core there is a burgeoning requirement to understand the complex interaction of the fluid-grain interface. The concept of stability and incipient motion is central to considerations of sediment dynamics. The turbulent flow around the sediment particles exerts a hydrodynamic force which tend to initiate particle motion. Alternatively, sediment modifies the turbulence structure when entrained within the flow or by creating a rough wall boundary condition when stationary on the bed. The importance of this concept is reflected in the extensive research to date, but despite the long tradition of research on this subject a comprehensive examination of the mechanisms that are responsible for the onset of sediment entrainment in a turbulent field are far from understood.

The turbulence in an open channel flow, such as flows in a river, is unsteady, irregular and statistically in-homogenous in at least one spatial direction. The motion of every eddy is random and unpredictable, which is an essential feature of turbulent flows. This impulsive behaviour of the flow at large Reynolds numbers is of interest as it leads to a wide range of velocity fields, that vary significantly and irregularly in both position and time. Similarly, the

particle bed can be related to a range of different sizes, shapes and topology of the particle bed is in general not trivial. Far from, the individual and bulk properties of the sediment particles are what controls the transport and deposition of sediment particles by water. The complexity between the turbulent flow and the properties of the particles are increased when under certain threshold conditions the hydrodynamics forces exerted by the turbulent coherent structures moves and entrains the sediment particle.

From the considerations it follows that an investigation of fluid particle interactions is imperative to push further our understanding of the dynamics of moderately shallow open channel flows. Indeed, an exhaustive description of the flow-roughness interactions, in particular where the particle bed is close to a natural bed, is still missing and should in principle require the systematic exploration of different wall configurations and relative submergence. The roughness characteristics of a natural bed are not homogenous and can vary with time. It would be more relevant for the purpose of studying sediment entrainment in natural rivers to try and remove the condition of roughness regularity. Roughness elements of similar size and shape in a random arrangement will presumably have different interaction with the flow with respect to a systematically arranged lattice bed.

## 1.2 Research objectives

The research objective is to improve the understanding of the fundamental aspects involved in sediment entrainment. This study approaches the topic by increasing the complexity of the problem in question in three steps. First, turbulent flow over a fixed bed of mono-sized spheres in a random arrangement is investigated. Similarly, turbulent flow over a bed of fixed heterogenous spheres in a random arrangement are investigated. Special emphasis is on the characterisation of hydrodynamic force and torque on particles as well as on the flow structures related to the force and torque. In the next step, the onset of sediment entrainment is studied by simulations with mobile spheres. Focus is given on the flow structures that relate to sediment entrainment and the characterisation of the entrainment process. High fidelity data with high resolution in space and time of the flow configurations described above is generated by direct numerical simulations (DNS) employing an immersed boundary method to resolve the particle fluid interface.

## 1.3 Outline of the thesis

The remainder of this manuscript is organized in the following manner: Chapter 2 provides an exhaustive review of the current state of knowledge of flow and turbulence, particle characteristics, forces on particles and sediment entrainment. Chapter 3 presents the equations governing the flow under consideration in this thesis, and introduces the numerical framework employed throughout the following chapters.

In Chapter 4 the approach for the two DNS of turbulent open channel flows is introduced. Turbulent open channel flow over a bed of mono disperse particles and turbulent open channel flow over a bed of poly disperse particles is presented. Characteristics of the flow field, the statistics of force and torque on a particle as well as characteristics of the flow structures related to force and torque are discussed in detail.

In chapter 5 the results of the DNS of turbulent, open channel flow with sediment transport of many mobile particles are reported. Focus is given on the statistics of particles and flow field.

Finally conclusions are drawn in Chapter 6, and suggestions for future work are provided.

*"Your task is not to seek for success, but merely to seek and find all the barriers within yourself that you have built against it."*

Rumi (1207 - 1273)

# 2

# Literature Review

This chapter deals with literature that is useful as a background for the micro-scale investigation of sediment entrainment in turbulent open channel flows. The chapter begins with an introduction to flow over rough walls, with an emphasis given to the size shape, distribution and arrangement of the bed. A review of present literature on heterogeneous beds is given is followed by hydrodynamic forces on the particles. The remainder of the chapter provides an overview on the phenomenon of turbulence laws in natural channels, followed by an introduction to sediment transport and the mechanism for particle entrainment.

## 2.1 Basic structure of open channel flow

Over smooth walls, classical convention sees the subdivision of a two-dimensional turbulent open channel into two distinct flow layers, the inner layer and the outer layer. The inner layer itself is comprised of a viscous sublayer and the buffer region. The outer layer includes the intermediate region and the free surface region (Nezu & Nakagawa, 1993). The free surface is an important aspect of open channel flow which distinguishes it from other common wall bounded flows such as closed channels, pipes and flat plate boundary layers. The characteristic length scale in the inner layer is the viscous length which is defined as the ratio of the fluid kinematic viscosity to the frictional velocity, $\nu/u_\tau$, while in the outer layer it is the flow depth or boundary layer thickness, say $H$. A dimensionless ratio can be formed using these two length scales, $Re_\tau = Hu_\tau/\nu$, known as the friction Reynolds number or Karman number, which signifies the degree of separation between the inner and outer length scales. The Karman number can be interpreted as a measure of relative submergence of the viscous sublayer. As the Karman number increases, a new region appears where both inner and outer scaling are simultaneously valid, known as the overlap layer.

The presence of roughness complicates matters with the introduction of a new relevant length scale, the characteristic roughness height, $\Delta$. The influence of roughness on the structure of the boundary layer is accounted for by the roughness Reynolds number, $Re_\Delta = u_\tau\Delta/\nu$. Empirical

measurements have shown that at low $Re_\Delta(< 5)$, the influence of roughness is masked by the viscous sublayer and the flow may essentially be classified as hydrodynamically smooth. As $Re_\Delta$ increases ($5 < Re_\Delta < 70$) a new regime is established where the flow is called transitionally rough. Beyond $Re_\Delta > 70$ the effects of roughness become dominant and the flow is termed fully rough (Nezu & Nakagawa, 1993). To incorporate the roughness effects and bed permeability, Nikora *et al.* (2001) propose a modification to the subdivision of the flow in an open channel into five specific layers. This subdivision is demonstrated in figure 2.1. Flow layers 1 and 2 incorporate the outer layer and overlap layer and are identical to their smooth wall counterparts. Flow layer 3 is known as the form induced sublayer where the effects of individual roughness elements on the flow above are believed to be important. Layer 4 is located within the roughness elements themselves, between the crests and the spatially averaged bed level ($z_{mb}$) and is called the interfacial sublayer. The form induced and interfacial sublayers are collectively recognised as the roughness layer.

Finally, in the case of a permeable bed, a fifth flow layer will be present beneath the roughness layer, known as the subsurface layer, as well as depicting all flow layers, figure 2.1 also defines the origin of the vertical coordinate at the roughness crests, $z_c = 0$; the flow depth measured between the water surface and the spatially averaged bed level, $H$; the flow depth measured between the water surface and the roughness crests, $h$; and the roughness height, $\Delta$, adopted in this study. From these definitions another distinctive feature of rough bed flow can be introduced, termed the relative submergence, which is given by the ratio of the flow depth to the roughness height, $H/\Delta$. The relative submergence indicates the degree of separation between the inner and outer layers. Nikora *et al.* (2001) suggests reclassifying flow in open channels into four main types according primarily to their submergence. Firstly, flow type ($I$) is of high relative submergence and all flow layers depicted in figure 2.1 exist. Flow type ($II$) is of intermediate submergence such that the subsurface layer (if applicable), the roughness layer and the outer layer are present. The existence of an overlap layer, where the velocity distribution is logarithmic, is questionable in type ($II$) flows and requires clarification. Flow type ($III$) is of low submergence where the roughness layer extends across the entire flow depth. Finally, flow type ($IV$) is at the extreme end of the scale, but not necessarily uncommon in natural river systems, where the roughness elements protrude through the free surface such that the interfacial sublayer covers the entire flow depth. The experimental conditions examined in this study pertain to flow type ($II$).

## 2.2 Mean velocity distribution

### 2.2.1 Logarithmic layer

The universal logarithmic law for describing the distribution of mean streamwise velocity above a rough-bed is given by equation 2.1.

$$\frac{\langle \overline{u} \rangle}{u_\tau} = \frac{1}{\kappa} \ln \left( \frac{z + d}{\Delta} \right) + C \tag{2.1}$$

where $\kappa$ is known as von Karmans constant (thought to be universal), d is the zero plane displacement (see 2.4.4) and $C$ is some constant (also assumed to be universal). Equation 2.1 remains a cornerstone of turbulence theory. One of the central underlying assumptions in its

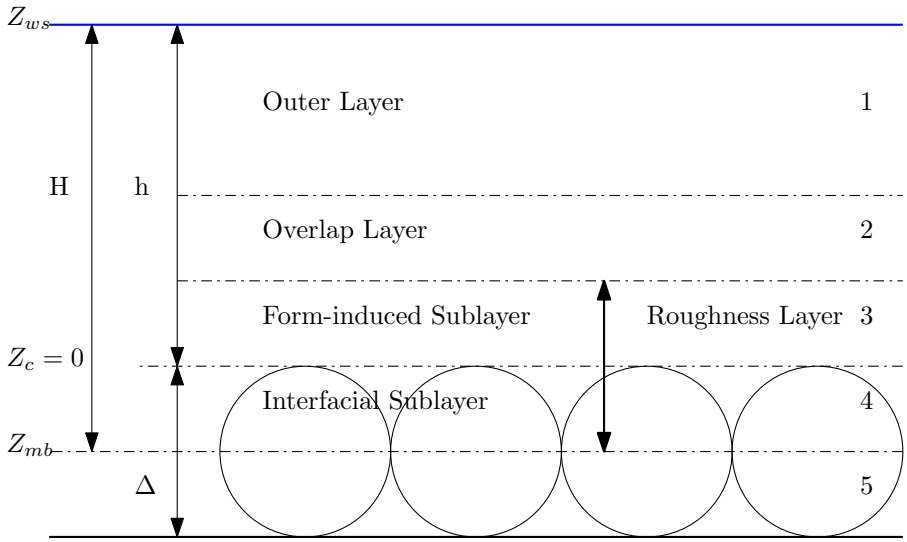



Figure 2.1: Classification of different flow layers in a rough-bed open-channel (adapted from Nikora *et al.* (2001)). The sketch shows the definition of the flow depth measured between the free surface and the spatially averaged bed level, $H$; the flow depth above the roughness crests, $h$; and the roughness height, $\Delta$, used in the present study. Note also that the origin of the vertical coordinate in this study is fixed at the elevation of the roughness crests i.e. $z_c = 0$.

derivation is that there must exist a region in the flow where the only relevant length scale is the distance from the wall. In other words, there needs to be a region far enough from the bed for the roughness scales to be negligible and simultaneously far enough from the outer edge of the boundary layer to escape the influence of outer length scales. Adopting an empirically justified value of $3\Delta$ for the upper extent of the roughness layer and $0.15H$ for the upper extent of the logarithmic layer, Jimeńez (2004) argues that a relative submergence of at least 40 is then required for less than half of the near bed layer to be affected by the roughness. Despite this limitation, numerous attempts have been made to apply the logarithmic law to measured data in flows with low to intermediate submergence, albeit with mixed success. One common point of disagreement is the supposed universal value of $\kappa$. While some studies support the validity of equation 2.1 at low submergence (e.g. Nakagawa & Tsujimoto (1980)) there are others which have found contrasting results. For example, Bayazit (1976) found that $\kappa$ fell from approximately 1.6 to 0.41 for a change in submergence of 1 to 4. Conversely, Koll (2006) collated a variety of low submergence experiments and plotted $\kappa$ as a function of $h/\Delta$. While there is a large degree of scatter in the results, the general trend is for $\kappa$ to decrease as $h/\Delta$ decreases, even reaching a value as low as 0.18 when $4 < h/\Delta < 7$. With such considerations in mind, Nikora (2007) has proposed a modified overlap approach to derive the logarithmic law for type $II$ flows in which $\kappa$ is a function of the relative submergence. Aside from open-channels, Nagib & Chauhan (2008) have recently demonstrated clear variations in the magnitude of between channel and pipe flow using composite velocity profiles of experimental and DNS data. It is expected that at least part of the disagreement between the studies mentioned above is a reflection of inconsistency in the fitting procedures. Not only are accurate velocity measurements required across a range of $h/\Delta$ but the data must be backed up by robust techniques to define the parameters of the log law, namely $d$, $u_\tau$, $\kappa$ and $C$.

### 2.2.2 Interfacial sublayer

Despite extensive research into rough-bed flows, not much is known about the velocity distribution within and around the roughness elements. Perhaps this is in part due to the technical challenges it poses to experimentalists while numerical simulations are still restricted to low Reynolds number and simplified roughness geometries. Nikora *et al.* (2004) put forward three models to describe the distribution of double-averaged streamwise velocity in the interfacial sublayer. The models correspond to constant, linear and exponential velocity distributions respectively. These models await further validation from experimental and numerical data. Measurement limitations in the present study prevents the investigation of the flow below the roughness crests, consequently, features of the interfacial sublayer are not considered further.

### 2.2.3 Bed origin in rough flow

In smooth bed flows, the choice of origin for the mean velocity profile appears straightforwardly to coincide with the elevation of the bed. However, over rough bed flows the choice of which elevation to use as the origin is more complicated. Nikora *et al.* (2002) distinguish between three different bed levels. These origins do not necessarily coincide but equally they do not exclude each other with each being useful for specific situations. Bed type 1 corresponds to the spatially averaged bed level, which is useful for defining the bed shear stress and the flow depth. Origin types 2 and 3 correspond to the bed level for plotting the logarithmic velocity distribution and the spatially averaged velocity distribution in the roughness layer respectively. Bed origin type 2 in particular is a source of uncertainty in studies over rough-beds (Nikora *et al.* (2002)). Originally, an offset was introduced to the vertical coordinate to improve the fit of the velocity data to the universal logarithmic law. This offset is known as the zero-plane displacement and is denoted $d$. The position of the zero-plane is often empirically taken between $0.17 - 0.354\Delta$ below the crests (e.g., Ein (1958) and Bayazit (1976)) or sometimes at the level of the roughness crests (e.g., Nakagawa *et al.* (1991); Manes *et al.* (2007)) but in most cases without seemingly any physical justification. The technique of Nikora *et al.* (2002) suggests a physically meaningful method for obtaining $d$ from the distribution of $d\langle\bar{u}\rangle/dz^{-1}$ against distance from the wall. Theoretically, a region of linearity in the profile is indicative of the presence of a logarithmic layer. Regression analysis then allows calculation of $d$. Physically, this elevation is proposed to be the level at which large wall attached eddies sense as the bed and hence the distance from which they scale.

While the correct bed origin for the mean velocity profile remains unclear, there is also, uncertainty regarding the bed level of higher order statistics such as the turbulent intensities. It may be conjectured that the instantaneous features of the flow that give rise to the mean velocity distribution should also control the distribution of all related higher-order statistics. Therefore, any offset applied to the mean velocity should apply to other statistical distributions. This practice is rarely adopted but there are examples of studies applying a zero-plane offset to the vertical coordinate when plotting turbulence intensities (e.g., Cameron *et al.* (2008)). In order to maintain consistency and comparability between studies this issue should be resolved.

## 2.3 Flow over rough walls

A large body of literature exists that deals with the characteristics of flow over rough surfaces. A reference for the earlier work on roughness is Schlichting (1936*b*); a comprehensive review on the subject, including numerical studies is given by Jimeńez (2004). Some consequences of roughness for high Reynolds number experiments have recently been reviewed by Marusic *et al.* (2010). Some of the key questions of interest in the research on rough wall turbulence are how roughness influences the turbulence structure, what are the consequences for scaling, and how can the effect on the fluid be estimated from the roughness geometry. Thus, the focus is almost exclusively on the effect of the rough wall on the fluid and the nature of the fluctuating force and torque acting on individual roughness elements is mostly not investigated.

Much of the literature before 1990 concerns itself with the universal aspects of flows over rough walls. After the pioneering systematic work of Nikuradse (1933) on rough pipe flows, Schlichting (1936*a*) was the first who experimentally investigated the effects on open channel flow of combining different (regular, homogeneous) arrangements of spheres mounted on a smooth wall and varying their size. Since then, large efforts have been devoted to investigating the relevance of the roughness geometrical features on the turbulence structure. Recent research has emphasized the differences between different types of roughness. It has been postulated that the details of the wall may influence the flow across the whole boundary layer therefore, in the last decade numerous authors have dedicated themselves to examining these claims and their significance in understanding wall turbulence. One common approach to account for wall roughness has been to resolve the flow around the individual roughness elements, specifying as boundary condition the no-slip condition (zero velocity) at the walls of these elements.

Direct numerical simulation of flow over a wavy wall have been carried out by De Angelis *et al.* (1997), Cherukat *et al.* (1998) and more recent by Yang & Shen (2010). Direct numerical simulation of channel flow over a wall roughened by spanwise-oriented square bars have been carried out by Orlandi *et al.* (2003), Leonardi *et al.* (2007) and Ikeda & Durbin (2007). Turbulent flow over spanwise oriented square bars with heat transfer was investigated by Miyake *et al.* (2001) and Nagano *et al.* (2004). Orlandi & Leonardi (2008) have simulated plane channel flow including different layouts of wall-mounted cubes. Direct numerical simulations of channel flow with wall velocity disturbances (acting as artificial roughness) have been carried out by Orlandi *et al.* (2003) and Flores & Jimeńez (2006). More in line with the present setup, Singh *et al.* (2007) have performed simulations of open channel flow over spheres in hexagonal arrangement using the Immersed Boundary Method (IBM), Clemens *et al.* (2011), Mazzuoli & Uhlmann (2017) and Ji *et al.* (2013) have performed simulations of open channel flow over spheres in a lattice arrangement and the later in a random array of mono disperse spheres.

Majority of the research has been dedicated to understanding the turbulent structures around mono disperse particles. Although this is an acceptable approximation of the different shaped and sized particles found it does not represent the reality of the problem and thus limits the problem from being completely understood.

### 2.3.1 Particle Distribution

Bulk sediment particle characteristics refer to the properties of a volume of heterogeneous material on the bed of an alluvial channel. Bed roughness represents a fundamental issue of river

hydraulics and fluvial geomorphology. It influences the properties of the average flow, turbulence and particle motion. The effect of the bed roughness is one of the key problems in understanding near-bed processes important for benthic organisms. However, the appropriate quantitative description of bed roughness is still a problem. Current methods for quantifying bed roughness can be categorised into two main groups: (1) a characteristic particle size approach and (2) a random field approach. The first appeals to the detail where the surface of sediment bed is composed of discrete particles forming bed roughness, while the second considers the bed surface as a random field $z(x, y)$ of bed elevations. Both approaches have attracted many studies in the field of river hydraulics and fluvial geomorphology.

Most natural bed sediments are dominantly heterogeneous. The frequencies of various particle sizes usually differ from the individualities of a normal distribution, i.e., particle size distributions are usually asymmetrical. For that reason, the use of a logarithmic unit is useful in the sense that it transforms the frequency distribution of particle sizes into a normal or near-normal distribution. However, the assumption of a log-normal distribution of grain sizes is frequently only a rough approximation (Rice & Church (1998)). A normal distribution in turn can be characterised by its mean and standard deviation. These two indices are frequently used in fluvial geomorphology. That is, the mean of a log-normal distribution is equivalent to the median of the original distribution of particle sizes. The median particle size of a sample of bed sediment is traditionally identified by the particle size distribution percentiles, $d_5$, $d_{90}$, $d_{84}$ and $d_{16}$ (Bathurst *et al.* (1985)). The motivation to describe bed roughness with a single particle scale originates from the classical work of Nikuradse (1933). Because of the simplicity of the single particle scale approach, it is widely used in river hydraulics and fluvial geomorphology and is well documented in literature. However, the bed roughness in natural rivers can be characterised by a single percentile, say $d_{84}$, only if we assume that the shape of the particle size distribution, bed arrangement, particle shape and orientation, packing, spacing and sorting, particle clusters are universal. Natural beds are highly heterogeneous and include a wide range of geomorphological features

If an attempt is to be made to describe a relationship between the characterisation of riverbed morphology and its interrelations with flow then it is important that closer attention is given, than has been done so previously, to the detailed features of the geometrical properties and roughness characteristics of alluvial beds. Recent comparison of various methods is given by Nikora *et al.* (1998), whom proposes an alternative way to describe the bed roughness by considering it as a random field of bed elevations $z(x, y)$. in this method, the use of moment functions is employed for a quantitative evaluation of the bed roughness. Indeed, if the bed elevation field is stationary, homogenous, and Gaussian, the moment functions of the second order will provide full information about the roughness. Coleman *et al.* (2011) has developed this method which evaluate statistical moments of measured bed elevation fields as quantitative measures of riverbed geometry that provide a better insight into the characteristic scales and kinematics for alluvial beds.

### 2.3.2 Surface texture

Mixtures of heterogeneous particles act in fundamentally different ways from mono sized particle mixtures. Fenton & Abbott (1977), experimentally showed that relative protrusion into the flow has an important effect on the mobility of a single particle. Their work indicated that for a particle exposed on a sediment bed the dimensionless shear stress required to entrain it was

approximately $5-6$ times smaller than values found by Shield's curve. Conversely, they found that critical dimensionless shear stresses of the order of 0.15 were required to move grains with no protrusion i.e., approximately three times higher than for a similarly sized grain per the Shield's criteria. The variation in resistance to dislodgement, with respect to relative position in the sediment bed, contributed to the difference in behaviour between heterogeneous and mono sized particles. These packing effects begin to explain why a mixture of particle sizes cannot be considered as a collection of individual particle sizes because of the way in which they affect each other. Therefore, it is clear that the mechanics of entrainment of a mixture differs greatly from that of a single size particle. Their work gives indications of how important a particle's near neighbours are to the threshold of dislodgement. The relationship between entrainment and bed texture lies not only in the sheltering and exposing abilities of a roughened surface but also in the effect that surface particle resting geometries have on the near bed flow.

This occurs through the generation of turbulence within the flow and alterations of mean flow pattern close to the bed caused by irregularities in the bed surface. This adjustment of the near bed flow field has been studied for isolated hemispheres used to simulate the effect of large stable particle, Brayshaw *et al.* (1983). The existence of protruding particles also increased peak values and modified the spatial pattern of the mean turbulence intensity around the obstacle. Characteristics of the bed surface which are important in the entrainment of a particle are the spacing, arrangement and size of the larger elements, which may be composed of a single large particle or groups of particles. Such bed surface organisations and geometric arrangements has been observed in the laboratory by Tait *et al.* (1992).

### 2.3.3 Particle arrangement and friction angle

The packing arrangement of sediment particles is a significant bulk particle property. Qualitative observations are reported on the packing arrangement of coarse grains, and how this may affect the properties of the average flow, turbulence and near-bed processes. Packing arrangement refers to the organisation of the particles on the stream bed. This is especially important with coarse gravels, irregular particles and poorly sorted sediment (Brayshaw (1985)).

Loosely defined frictional forces can be defined as a measure of the ability of a grain to entrain. In the context of sediment transport, it refers to the contact angle between superimposed particles and how easily it moves from its resting position. The frictional angle is depicted in figure 2.2. In uniform sediment distributions, this angle would be of the order of $30-32$. In heterogeneous sediments, it varies tremendously with the particle sizes involved. Figure 2.2 clearly illustrates that, for the simple case of spheres, the pivoting angle varies with the ratio of the size of the spherical grain to the size of the grain upon which it rests (Kirchner *et al.*, 1990).

## 2.4 Hydrodynamic forces on fixed particles

Providing reliable predictions of the riverbed evolution requires a clear picture of the interaction between the flow and the bottom roughness due to sediments particles. An imperative aspect in the investigation of particles immersed in a turbulent fluid is the consideration of the hydrodynamic force exerted by the fluid upon the particles. This area has gained the attention of numerous authors over the last century and still appeals to the scientific and engineering

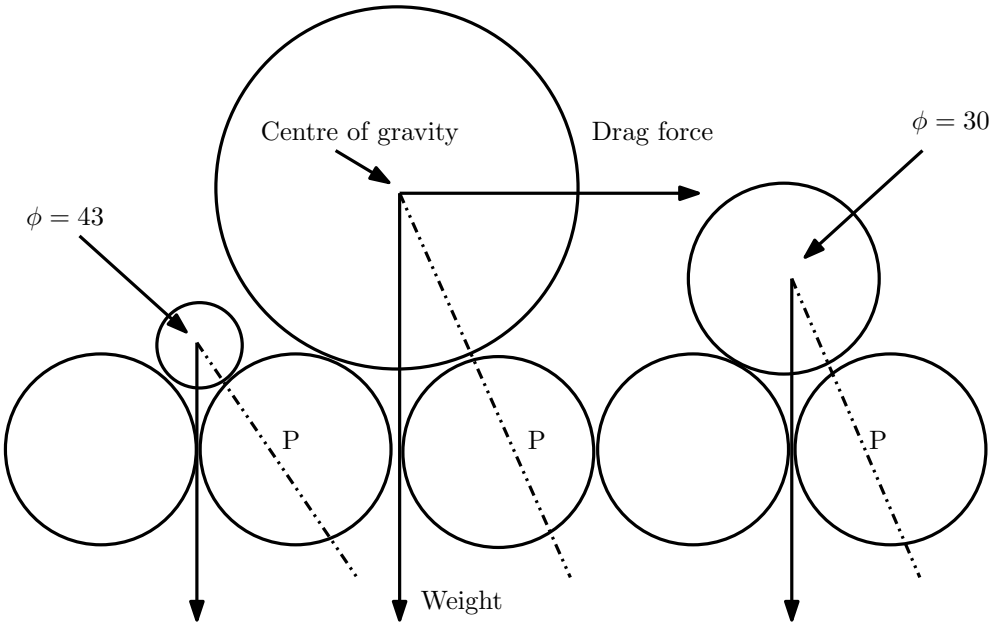



Figure 2.2: Schematic diagram illustrating the dependence of the pivoting angle ($\phi$) on the relationship between the diameter of the particle considered and that of the particle upon which it rests (Robert, 2003)

community, for applications in a diverse range of disciplines. One of the earliest systematic study provided a theoretical description of the hydrodynamic force for creeping flows. The works of Poisson (1831), Stokes (1845), Basset (1888), Oseen (1911, 1913), Faxn (1922), Gatignol (1983), Maxey & Riley (1983) and Hall (1988) contributed significantly to the knowledge and understanding of the hydrodynamic force in flows.

On the opposite, for flows with finite or large particles and fluid velocities it was not possible to obtain an analytical expression for the hydrodynamic force. Thus, most of the works were initially experimental and later with the rise of computing, numerical. In the absence of suitable theoretical based methods, Hall (1988) experimentally investigates the lift force on a sphere on both rough and smooth surfaces, five particle geometries are considered to gain a limited understanding of the influence of substrate geometry upon the forces acting on particles on rough surfaces. Hall (1988) observes that surface roughness can significantly change the mean fluid-induced lift forces acting on particles on surfaces, reducing the force when a particle is deposited between roughness elements and increasing it when a particle is on top of a single rod. Increases of a factor of 2 and decreases of a factor of 6 in lift forces were observed.

Amir *et al.* (2014) investigated the hydrodynamic force exerted on spheres mounted in hexagonal patterns on the wall, by instrumenting several spheres with four-point pressure probes. They computed the statistics of pressure fluctuations for several cases differing in the bed slope and flow depth and were able to estimate the integral time scale of drag and lift fluctuations on the basis of measurements made from spheres equally paced in a row. However, by adopting the four-point pressure technique, Amir *et al.* (2014) did not consider the distribution of the stress on the surface of individual spheres, and they could not account for the distribution of the shear stress and how it is affected by Reynolds number effects. Also, this task can be achieved more easily numerically.

Direct measurements of the fluid hydrodynamic force acting on a particle present consider-

able, if not insurmountable, technical difficulties, something that can now be achieved easily through numerical computations. Direct numerical simulations of open channel flow have been performed over a bed of spheres in square arrangement by Mazzuoli & Uhlmann (2017). The work extends the results obtained by Clemens *et al.* (2011) for an open channel flow in the transitionally rough regime, Mazzuoli & Uhlmann (2017) show how the flow structure changes as the fully rough regime is attained and directly compare the experimental data from Amir *et al.* (2014) with their observations. The convective velocity and turbulent structures are estimated from the hydrodynamic forces acting on the neighbouring particles, the values observed show fair agreement with those obtained by Amir *et al.* (2014). This supports the observation that the convective velocity depends only on the relative submergence while it is independent of the Reynolds number and, on that basis, it also appears largely independent of the precise arrangement of the roughness elements.

A comprehensive examination of the hydrodynamic mechanisms responsible for the entrainment of particle beds with a focus on the dynamics occurring at the small scale have been investigates by Derksen & Larsen (2011). The authors consider the drag and lift forces on fixed, random assemblies of fine mono-sized particles, where the size of particles is comparable to the smaller than the smallest flow length scales. As a result, the particles experience laminar flow. The average drags and lift forces on a sphere in a layer of particles are described as monotonically decaying functions of the surface occupancy. At larger occupancies, the flow largely skims over the layer, which reduces drag to skin friction drag and which deteriorates the lift force. The sphere-to-sphere variability of the drag and lift forces is significant. Derksen & Larsen (2011) postulate that the variability of the force is due to wall-normal forces on spheres in a monolayer are due to hydrodynamic interactions of the spheres, inducing a hydrodynamic environment around spheres with significant wall-normal velocity components. As the authors increase the surface occupancy of the bed by generating additional layers of mono-sized particles the drag and lift forces get weaker as these hydrodynamic effects decay with increasing surface coverage.

The wall normal position where the mean dynamics become inertial is an irreducible function of roughness and Reynolds number, as it is an inherent function of the relative scale separations between the inner roughness, and outer lengths. Mehdi *et al.* (2013) indicate that, for any given roughness, new dynamical regimes will typically emerge as the Reynolds number increases.

Lee & Balachandar (2010) performed direct numerical simulations using a variant of the immersed boundary method to understand the characteristics of the hydrodynamic forces on a finite-sized particle moving against a wall. The drag and lift forces and torque on such a particle can be considered to arise from the superposition of three different mechanisms: forces due to shear, forces due to particle translation and forces due to particle rotation. The limitation of the study by Lee & Balachandar (2010) is the low Reynolds numbers considered (1 to 100), over this limited range of Reynolds number the, the flow around the particle remains in all the alternate configurations considered by the authors remains steady. The asymmetric effects of linear shear and the presence of a nearby wall are to decrease the critical Reynolds number, while the added viscous effect due to the wall will tend to delay the onset of unsteadiness to higher Reynolds number. Motivated by the low-Reynolds-number drag and lift superpositions, Lee & Balachandar (2010) propose functional relations for drag and lift forces. The expressions are physically motivated and rely on superposition of the individual mechanisms and their cross-coupling-effects.

### 2.4.1 Effects of neighbouring particles

It has been well established that an agglomerate of particles interact with the flow, and the nature and extent of the interactions depend on the flow characteristics, fluid properties and bed properties such as its density, topology, particle size (distribution) and inter-particle forces. Secondly the turbulent flow over the bed has a spectrum of length scales interacting with the bed. Together these dynamics have been thoroughly investigated on a global level by Clemens *et al.* (2011); Mazzuoli & Uhlmann (2017); Kidanemariam & Uhlmann (2017), Lee & Balachandar (2010), Mehdi *et al.* (2013) and Milici *et al.* (2014). On a micro-scale the local hydrodynamic mechanisms and the influence of neighbouring particles, associated with the entrainment of natural bed-forms remains unclear.

Akiki *et al.* (2017) introduces a new point-particle force model that attempts to account for the hydrodynamic influences of the neighbouring particles. In point particle models the force on a particle depends only on the Reynolds number and the mean volume fraction, hence, if the mean volume fraction is the same, the force on the alternate particles will be estimated to be the same, even though the local packing arrangement of the particles and neighbouring particles can change vastly from bed-to-bed. An example of this variation in force on neighbouring particles is provided by Akiki *et al.* (2017), where a nominally uniform flow over a random distribution of stationary particles at varying Reynolds number and volume fraction was considered. The drag calculated drag force showed a significant variation from particle to particle and the root mean square drag force fluctuation was measured to be as high as 25% of the mean value. This significant variation is predominately down to each individual particle within the distribution observing a local distribution of neighbouring particles. Although Akiki *et al.* (2017) provides a very comprehensive and concrete study of the effect of neighbouring particles, one primary limitation of the study is the random arrangement of particles and the relatively low Reynolds number and volume fractions considered. However, the study provides a foundation to relate the point particle model to sediment beds and develop a greater understand by investigating the effects adjacent particles and packing arrangements in the entrainment of particles.

## 2.5 Onset of sediment transport

The start of modern research on the onset of sediment erosion is commonly linked to the doctoral thesis of Shields (1936). He proposed to define the onset of sediment erosion by the parameter that now bears his name. The Shields parameter is defined as

$$\theta_s = \frac{\tau_w}{(\rho_p - \rho_f)gD} \tag{2.2}$$

where $\rho_p$ is the density of the sediment particles, $\rho_f$ is the density of the fluid, $g$ the value of the gravitational acceleration and $\tau_w$ the wall shear-stress which needs to be further defined in the context of geometrically rough wall. Shields suggested that the value of $\theta_s$ related to the onset of erosion, i.e. $\theta_{thres}$, is a function of the particle Reynolds number, $Du_\tau/\nu$, where $u_\tau = \sqrt{\tau_w/\rho_f}$ is the friction velocity, $D$ is the particle diameter and $\nu$ the kinematic viscosity. The doctoral thesis remained the only contribution of Shields to the subject, albeit with a strong impact on the hydraulic community, which lead to that his work and also his life has been a matter of various discussions (see Kennedy (1995), and Buffington (1999), for an overview).

Several studies related to sediment erosion follow the approach of Shields. A review of the literature, that can also serve as an introductory text, can be found in manuals and textbooks on the subject, e.g. Vanoni (1975); Yalin (1977); Van Rijn *et al.* (1993) Garcia (2008). A compilation and discussion of experiments in the style of Shields is given by Buffington & Montgomery (1997). Some recent studies focused on the onset of sediment erosion in low Reynolds numbers (e.g., Charru *et al.* (2007); Quadrio & Luchini (2003); Lobkovsky *et al.* (2008); Peysson *et al.* (2009). It should be noted that a good approximation to the data of Shields can be derived from assuming a relation between mean drag on a exposed particle and the law of the wall (Ikeda (1982); Garcia (2008)).

Despite the widespread use of Shields approach to define the onset of sediment erosion, the scatter of $\theta_{thres}$ obtained in experiments remains unsatisfactorily large. This might be related to challenges inherent to the problem of defining the onset of erosion (see for example Naden (1987) for a discussion). As has been argued in the beginning, the geometrical properties of the bed are in general not trivial due to the wide range of particle size, shape, densities and the complexity related to particle arrangements. Being additionally linked to a highly turbulent flow field the characteristics of force and torque on particles are even more complex and might be considered as random variables. Some authors argue that when described as a function of a random variable the onset of sediment erosion has a certain probability which can never be precisely zero (Garcia (2008) Papanicolaou *et al.* (2002)). In addition to this probabilistic aspect, the definition of what is considered as erosion of a particle cannot be made unambiguously. For example, the motion of a particle across a bed is often classified into saltation and rolling, where the latter might not be considered as erosion. Also, Charru *et al.* (2007) found that the mean distance of a particle moving over an array of spheres from one resting position to the next is related to the Shields number. Thus, the definition of what is considered as erosion of a particle might influence the value of the critical Shields number.

Realising the limitations of defining the onset of erosion by a single global parameter, some studies concentrate on the flow structures that relate to high force events on fixed particles or the flow structures that lead to the onset of sediment erosion. Sutherland (1967) was among the first to investigate flow structures related to the onset of sediment erosion. More recent studies employing truly mobile particles are those by Niño & García (1996), NiÑo *et al.* (2003), Hofland *et al.* (2005), Cameron *et al.* (2008), Dwivedi *et al.* (2010). Experiments on flow structures related to possible sediment erosion predicted based on fixed particle data have been carried out by Detert *et al.* (2010), Dwivedi *et al.* (2010). The results of the recent experiments based on fixed and mobile particles indicate that sediment erosion is often related to regions of positive streamwise velocity fluctuations in the vicinity of the eroding particle.

### 2.5.1 Sediment transport

Performing experiments in multi-phase flow is difficult as the solid phase can interfere with the measurement device. In spite of these difficulties, several configurations related to particle laden open channel flow were investigated experimentally over the last two decades (Kaftori *et al.* (1995); Taniere *et al.* (1997); citerighetti2004particle; Muste *et al.* (2009)). Most of these experiments were performed using dilute suspensions, with a volumetric concentration of order $\Theta(10^{-3})$, and various kinds of sediments. For example, in the study of Taniere *et al.* (1997) the density ratio between the solid and fluid phase was very high since they employed glass and polymer particles in air. The density ratio was lower in the rest of the studies, ranging

from values as low as 1.05 in the experiments of Kaftori *et al.* (1995) (polystyrene particles in water) to 2.6 in Kiger & Pan (2002) and Righetti & Romano (2004) (both used glass particles in water), while Muste *et al.* (2009) covered the range 1.03 to 2.65 using natural sand and neutrally buoyant sand (crushed nylon) in water. These experiments have shown the existence of a velocity lag (in the mean) between particle and fluid velocities, and modifications to the turbulence characteristics of the flow due to the presence of the suspended particles.

Computational studies are only now beginning to appear. An exception is the pioneering work of Pan & Banerjee (1997), who conducted resolved direct numerical simulations of turbulent particulate flow in a horizontal channel using 160 stationary and mobile particles. Since then, numerous authors have carried out work on this subject, most notably Clemens *et al.* (2011), Mazzuoli & Uhlmann (2017) and Kidanemariam & Uhlmann (2017).

## 2.6 Outcome of literature review

This review of the literature has shown that although simulation methodologies have reached a high degree of sophistication, understanding of the basic physical processes associated with heterogenous, unsteady, sediment transport is still poor. This lack of knowledge of the basic physical processes has been obscured by the use of empirically derived simple multiplicative adjustment factors for the use with single sized transport and entrainment formulae. Present day numerical models have indicated that these relationships do suffer from serious deficiencies, although novel numerical techniques for the measurement of bedload transport rates at a grain scale are now being developed. The importance of detailed mathematical modelling of specific features of a sediment transport system is clear. This will allow for improvements in prediction techniques because they will simulate the actual physical processes more faithfully.

*"One solitary person cannot help or save an age; he can only make it clear that it is on its way to a downfall"*

Soren Kierkegaard (1849)

# 3 Fundamentals

This chapter provides a summary of some fundamental aspects related to this thesis. On one hand, it serves as a reference for the following chapters, on the other hand it provides references for further reading. Section 3.1 provides a review on the governing equations of fluid flow 3.1.1, solid body motion 3.2 and the coupled fluid-solid system 3.2.4. An overview on the phenomenon of turbulence is given 3.3.1, followed by an introduction to numerically studying turbulent flow 3.3.2. A description of the numerical method used in this thesis and some validation aspects is given in 3.3.3.

## 3.1 Governing equations

### 3.1.1 Continuum hypothesis and Navier-Stokes equation

In the process of deriving a mathematical description of fluid flow several assumptions are made. One of the most fundamental assumptions is the treatment of fluids as a continuum, i.e., that its macroscopic behaviour can be described by being continuous in space. Thus, the molecular structure of the fluid is neglected and the effect of it is taken into account only in an average sense. A measure for when the continuum hypothesis can be considered appropriate is the Knudsen number, $Kn$, which is defined as the ratio of a characteristic molecular length scale, e.g., the mean free path of molecules, and a characteristic length scale of macroscopic flow properties, e.g., a length scale of the smallest scales of fluid motion. In most engineering applications is it found that $Kn << 1$ by several orders of magnitudes, which indicates that the continuum hypothesis holds (Batchelor (1976); Pope (2000)). Other assumptions concern the variations of the fluids density, $\rho_f$, and the relation of shear stress to rate-of-strain. In the present study only incompressible fluids are considered, that is the density of the fluid is independent of space and time, $\rho_f = \text{const}$. Furthermore, the fluid is considered to be Newtonian, that is the relation between the non-isotropic part of the shear stress and the rate-of-strain tensor is linear (Batchelor (1976)).

$$\tau_{ij} = \mu \left( \frac{\partial u_i}{\partial x_j} + \frac{\partial u_j}{\partial x_i} \right), \qquad \text{for } i, j = 1, 2, 3 \tag{3.1}$$

where $\tau_{ij}$ is the viscous stress tensor, $\mu$ is the dynamic viscosity of the fluid, defined as the product of the density of the fluid, $\rho_f$ and the kinematic viscosity of the fluid $\nu$, $\mu = \nu\rho_f$, $\mathbf{u}$ is the velocity vector $\mathbf{u}$=$(u, v, w)$ in Cartesian coordinates with axis $x, y$ and $z$ in the spanwise, streamwise and wall-normal direction respectively. Note, that in the following bold symbols are used to denote tensor or vector quantities and indices 1, 2, 3 or $x$, $y$, $z$ to denote vector components in the Cartesian reference frame, e.g., $f_x$ or $f_1$ denote the streamwise component of a vector $\mathbf{f}$. Based on the principle of conservation of mass, the continuity equation for an incompressible fluid reads

$$\nabla \cdot u = 0 \tag{3.2}$$

where $\nabla$ is the Nabla operator, i.e. in Cartesian coordinates $\nabla = \partial/\partial x, \partial/\partial y, \partial/\partial z$, and $\cdot$ denotes the dot product between two vectors. Based on the principle of conservation of momentum, the momentum equation for an incompressible Newtonian fluid can be written as

$$\frac{\partial u}{\partial t} + (u \cdot \nabla)u = -\frac{1}{\rho_f}\nabla p + \nu\nabla^2 u + f \tag{3.3}$$

with time $t$, pressure $p$, Laplace operator, $\nabla^2 = \nabla \cdot \nabla$, $\mathbf{f}$, on the fluid. The set of equations 3.2 and 3.3 are called NavierStokes equations in the following. A detailed derivation of the NavierStokes equations can be found for example in Schlichting (1936*b*), Batchelor (1976) or Pope (2000). With reference scales for length, time, velocity and pressure the NavierStokes equation 3.2 and 3.3 can be written in dimensionless form. This shows that only a single non-dimensionless parameter governs the characteristics of the NavierStokes equations, namely the Reynolds5 number, defined as

$$Re = UL/\nu \tag{3.4}$$

where $U$ and $L$ are a characteristic velocity and length scale of the flow, respectively. The Reynolds number represents the ratio of convective terms to viscous terms, i.e., for small values of $Re$ the viscous terms dominate the fluid motion, and the flow is commonly found to be laminar. For large values of $Re$ the convective terms dominate the fluid motion, and the flow is commonly found to be turbulent.

### 3.1.2 Boundary conditions and initial conditions

The Navier-Stokes equations 3.2 and 3.3 are a set of four partial differential equations; one momentum equation and one continuity equation in each coordinate direction, for four unknown variables, $u, v, w$ and $p$. For a given set of appropriate boundary and initial conditions the evolution of a velocity field in time can be determined by integration; initial conditions for the flow variables are specified in the entire domain $\Omega$ at the initial time, boundary condition need to be specified always along the boundary $\Gamma$ of the domain $\Omega$ being considered. The boundary

conditions that are relevant to this study are described below, followed by description of some aspects of the initial conditions.

### Dirichlet and Neumann boundary conditions

A boundary condition for a variable, $\phi$ can be to specify its value for a given position $\mathbf{x}$ in time, $t$, i.e. $\phi(\mathbf{x}), t = c$, where $\mathbf{x}$ is located on the domain boundary $\Gamma$ and $c$ is a certain value. A boundary condition implemented this way is called a Dirichlet boundary condition. An example of a Dirichlet boundary condition is a stationary plane wall at $z = 0$. In case of a no-slip condition for the fluid at the wall, i.e., at the boundary the velocity of the fluid on the boundary is equal to the velocity of the boundary at each point, the velocity boundary condition always can be written as

$$\mathbf{u}(x, y, 0, t) = (0, 0, 0) \tag{3.5}$$

Another alternate boundary condition is to specify the gradient of a variable, e.g., $\partial\phi/\partial\mathbf{n} = c$, where $\mathbf{n}$ is the normal vector of $\Gamma$. Such a boundary condition is called Neumann boundary condition. An example of a Neumann boundary condition is the boundary condition for pressure at domain boundaries of a computational domain which is defined as zero

$$\frac{\partial p}{\partial \mathbf{n}} = 0. \tag{3.6}$$

### Periodic boundary conditions

In turbulent flows the domain can often be considered to be un-bounded in one or more directions. For example, in the case of open or closed channel flow the domain is infinite in the streamwise and spanwise periods. However, infinite domain dimensions can lead to mathematical and numerical instabilities. A method to simplify matters is to consider the flow field to be periodic in the respective homogenous directions. In the example of channel flow with wall-normal $z$ extension $L_z$ and periodic boundary conditions in the streamwise and spanwise direction with periodicities $L_x$ and $L_y$ can be written as

$$\begin{aligned} \mathbf{u}(x, y, z, t) &= \mathbf{u}(x + nL_x, y, z + mL_y, t), \\ \mathbf{p}(x, y, z, t) &= p(x + nL_x, y, z + mL_y, t), \end{aligned} \tag{3.7}$$

for any integer $n, m$ and $0 \leq x$ ¡ $L_x$, $0 \leq y$ ¡$L_y$, $0 \leq z$ ¡ $L_z$. The case of a non-periodic infinite flow field can be recovered by letting the periodicity go to infinity, i.e., $L_x \to \infty$ and $L_y \to \infty$. Therefore, for large ratios $L_x/L_z$ and $L_y/L_z$, the effect of the periodic boundary condition with respect to the infinite solution to the problem might be considered small. However, for small ratio $L_x/L_z$ and $L_y/L_z$, the effect can be large and influence the results considerably. This is because the largest scales of turbulent motion in the periodic direction are limited to the length of periodicity. Some studies make use of this aspect, to isolate certain scales of turbulent motion (Jimnez & Moin (1991)).

**Free-slip boundary condition and rigid-lid assumption**

a boundary condition relevant to the present research is the so called free-slip boundary condition. This boundary condition consists of a zero-velocity condition for the velocity component normal to the boundary, and a condition of zero-gradient for the other velocity components. For example, a free-slip condition at location $z = H$ can be specified via

$$\frac{\partial u(x,H,y,t)}{\partial z} = 0, \quad \frac{\partial v(x,H,y,t)}{\partial z} = 0, \quad w(x,H,y,t) = 0. \tag{3.8}$$

Although such a boundary condition is difficult to realise experimentally, it is of relevance to the simulation of open channel flow. In an open channel flow an interface exists, that separates lighter fluid, e.g., air, from a heavier fluid, e.g., water. The interface varies in height with time and thus is not fixed at a certain position. If the surface deformation is small, the variation of the surface might be neglected. this is called rigid-lid assumption and is equivalent to impose a free slip condition for the fluid velocity as described above. A more detailed discussion of the rigid-lid assumption can be found in Komori *et al.* (1993).

**Initial conditions**

For steady boundary conditions, that is the boundary conditions are constant in time, the flow can reach a state in which its statistics become independent of time, although, the flow field itself might be highly time dependent. The flow is then called to be in a statistically stationary state. It is generally assumed that for a given flow configuration the same statistically stationary state is reached independently from the initial conditions. Thus, the specific definition of initial conditions is often of minor interest when the characteristics of the statistically stationary state are considered. In numerical simulations the integration of the flow field in time until a statistically stationary state is reached can be very costly. The time needed is influenced strongly by the flow configuration under consideration and the choice of the initial conditions. It can be beneficial to specify the initial condition by interpolation of a flow field from a coarser simulation that reached a statistically stationary state. In a coarser simulation, the computational costs to overcome initial effects can be considerably smaller.

## 3.2 Equations of the solid particle phase

### 3.2.1 Equations of rigid-body motion

Similarly, to fluids, solids can be described as continua. This is of particular interest when the deformation of solids or the stress distribution within solid are important. Here, the deformation of solid particles due to hydrodynamic stress is much smaller than the particle dimension and is therefore neglected. Instead of a continuum approach, the particles are described by the mechanics of a rigid body. A rigid body can be defined as a solid for which the distance between two points of the solid does not change in time. This corresponds to assuming that the modulus of elasticity approaches infinity. The equations of rigid-body motion can be derived from Newtons second law for linear and angular momentum. For spherical particles these read

$$\frac{d\mathbf{x}_p}{dt} = \mathbf{u}_p, \quad m_p \frac{d\mathbf{u}_p}{dt} = \mathbf{F} \tag{3.9}$$

$$\frac{d\Omega_p}{dt} = \omega_p, \quad I_p \frac{d\omega_p}{dt} = \mathbf{T} \tag{3.10}$$

where the position of a particle is $\mathbf{x}_p$, the velocity of a particle is $\mathbf{u}_p$, the force on the particle is $\mathbf{F}$, the mass of the particle is $m_p$, the angular position of a particle with respect to the Coordinates axes is $\Omega_p$, the angular velocity of the particle is $\omega_p$, the torque on a particle is $T$ and the moment of inertia is $I_p$. The quantities above are defined with respect to the centre of mass of the spherical particle. Note, that for arbitrarily shaped rigid bodies the moment of inertia is a tensor quantity not a scalar as denoted above for the case of spherical particles. For arbitrarily shaped bodies the time derivation in 3.10 would need to consider the product of moment of inertia tensor and angular velocity. The equations 3.9 and 3.10 can be solved for the four quantities $\mathbf{x}_p$, $\mathbf{u}_p$, $\Omega_p$ and $\omega_p$ when appropriate initial and boundary conditions are specified, i.e. the initial conditions for $\mathbf{x}_p$, $\mathbf{u}_p$, $\Omega_p$ and $\omega_p$ need to be specified as well as the force and torque on the particle at each time as boundary conditions.

### 3.2.2 Forces on a particles

In the context of the present work the force on a particle, $\mathbf{F}$, is considered as the sum of (a) the hydrodynamic force, $\mathbf{F}^{\Gamma}$, defined as the integral of hydrodynamic stress on the particle surface, (b) the particle body force, $\mathbf{F}^{\Omega}$, due to the acceleration of the particle by a volume such as gravity. Both individual forces are described in detail below.

#### Hydrodynamic force

Hydrodynamic stresses on the surface of an impermeable particle in a fluid develops because of the no-slip condition between the fluid velocity and the velocity at the particle surface, i.e., the velocity of the fluid and particle surface are identical at every point of the particles surface. The hydrodynamic force can be defined as

$$\mathbf{F}^{\Gamma} = \int_{\Gamma} \tau \cdot \mathbf{n} \, \mathrm{d}\Gamma - \int_{\Gamma} p^{tot} \mathbf{n} \, \mathrm{d}\Gamma, \tag{3.11}$$

where $\Gamma$ denotes the particle-fluid interface and $p^{tot}$ denotes the hydrodynamic pressure.

#### Body force

the resulting force on a particle in a constant density fluid because of volume force, $\mathbf{f}$, acting on the fluid as well as on the particle, can be expressed as

$$\mathbf{F}^{\Omega} = \int_{\Omega} (\rho_p - \rho_f) \mathbf{f} \, d\Omega, \tag{3.12}$$

where $\rho_p$ is the density of the solid particle and $\Omega$ denotes the volume of the particle. In case $\mathbf{f}$,$\rho_p$ and $\rho_f$ are constant, thus equation 3.12 simplifies down to

$$\mathbf{F}^{\Omega} = (\rho_p - \rho_f) V_p \mathbf{f}, \tag{3.13}$$

where $V_p$ is the volume of the particle, i.e., $V_p = \int_\Omega d\Omega = 1/6\pi D^3$ in case of a spherical particle with diameter $D$.

### 3.2.3 Torque on a particle

Like the hydrodynamic and body forces, torque on a particle can be due to hydrodynamic stresses, volume forces and a model torque. The torque on a spherical particle as a result of hydrodynamic stress on its surface is defined as

$$\mathbf{T} = \int_\Gamma \mathbf{r}_p \times (\tau \cdot \mathbf{n}) \, \mathrm{d}\Gamma, \tag{3.14}$$

where $\mathbf{r}_p$ is the distance vector from the particle centre to an element of the particles surface $\Gamma$, and $\times$ denotes the cross product of two vectors. Contrary to the definition of the hydrodynamical force on a particle equation 3.11, the pressure does not enter the integral equation 3.14, since in the case of spherical particles the differential pressure force $-p^{tot}\mathbf{n}ds$ on a surface element $ds$, is always directed towards the centre of the sphere. This thesis is limited to consider force and torque on spherical particles with constant densities under the influence of constant volume forces. Hence, the volume force does not contribute to torque on the particles. Also, the contact model does not consider tangential contact forces, and thus does not contribute to torque on a particle. In conclusion, the torque on a particle in this thesis is only due to relation equation 3.14.

### 3.2.4 Fluid and particle coupling

Fluid flow with submerged mobile rigid bodies can be described by the two sets of equations discussed in sections 3.1.1 and 3.2. The coupling of the equations is established over the boundary conditions. A no-slip condition at the fluid-solid interface requires the velocity of the two phases to be equal and thus poses a boundary condition for the fluid. Similarly, hydrodynamic force and torque on the particle surface jointly with body force and model force pose boundary conditions for the rigid particle motion. With the requirement, that all conditions need to be satisfied at each instant in time, the coupling between the two sets is established and the problem is well defined.

## 3.3 Numerical simulation of turbulence and flow

In the previous section, the governing equations of fluid flow have been introduced. The present section gives a summary of the phenomenon of turbulence that can emerge from these equations, of the available tools to numerically study turbulent flow of a single-phase fluid as well as a brief description of the numerical method employed in this thesis to simulate fluid flow, as well as fluid flow with mobile rigid bodies.

### 3.3.1 Turbulence in fluids

Turbulence is a complex phenomenon that has been studied intensively for several decades in various fields of research, including mathematics, physics, engineering and biology. Often the questions related to turbulence differ from field to field, which might be one of the reasons, why a common definition of turbulence does not exist.

Turbulence in fluids is often introduced as a state of the flow, being either laminar or turbulent. The laminar state is characterised by a smooth variation of the flow variables and well-defined flow characteristics. Following the ideas of Tennekes & Lumley (1972), the state of turbulent flow can be characterised by a large range of scales of irregular, diffusive, dissipative and highly three-dimensional motions. Furthermore, the state of flow is related to large Reynolds numbers. Despite this somewhat loose definition, it appears to be sufficient to describe the turbulent flow. Examples to observe turbulent flow in everyday life are cumulus clouds, smoke rising from a chimney, the mixing of milk in the morning tea or flames of a bonfire. It is not hard to believe that the beauty of turbulent flow has fascinated mankind from the beginning. Indeed, some authors see the importance of turbulence to the hydraulic structures in the ancient civilisation as an indication that the responsible engineers must have had some understanding of turbulence and its effects (e.g., Rouse (1963)). One of the oldest documents on the study of turbulent flow dates back to the work of Leonardi Da Vinci (e.g., book cover Tennekes & Lumley (1972); Frisch (1995)). In spite of these references, the advent of modern turbulence research is commonly related to the mid 19th century, when detailed measurements of the pressure drop in turbulent pipe flow were carried out by Hagen (1854) and Darcy (1857). Two decades later, Boussinesq (1877) suggested a statistical treatment of turbulent flows and introduced the concept of an enhanced eddy viscosity. A detailed study on the transition from the laminar to the turbulent flow regime, was carried out by Reynolds (1883) who proposed the criterion that now bears his name. Later, Reynolds (1895) introduced the concept of flow decomposition. With the beginning of the 20th century, it became more and more clear how a phenomenon such as turbulence can emerge from a set of deterministic equations and it is now commonly accepted, that the NavierStokes equations are appropriate to describe turbulent flow. A major step in understanding the nature of turbulence was made by the work of A. N. Kolmogorov (e.g., Kolmogorov (1941)). In his work Kolmogorov advanced and quantified the energy cascade concept described by Richardson (2007). According to the concept, turbulent energy is injected in the large scales and transferred to smaller scales by an inviscid process. The Reynolds number of the smallest scales is low, such that viscosity becomes important and dissipates all energy in the small scales. Thus, this model provides an explanation of the way the rate of dissipation might be specified by the inviscid processes related to the large scales and not by the viscosity itself. A review of the work of Kolmogorov can be found in the book by Frisch (1995). The above introduction on the phenomenon of turbulence is far from being complete. A more detailed introduction can be found in review articles such as the one by Jimeńez (2004) or more detailed in form of textbooks on the subject (for example in Tennekes & Lumley (1972), Pope (2000) or Davidson (2015).

### 3.3.2 Direct numerical simulation of turbulent flow

Many textbooks classify the numerical approaches to study turbulent flow in direct numerical simulation (DNS), large eddy simulation (LES) and Reynolds averaged NavierStokes equations (RANS). These definitions are made according to the governing equation in each approach

which are the NavierStokes equations, the filtered NavierStokes equations or the time-averaged NavierStokes equations, respectively. An overview on the three approaches can be found for example in the textbook by Pope (2000). The present section provides an overview on DNS, which is the method used to study the flow configurations in this thesis. It is now generally accepted that, although being deterministic and based on a continuum approach, the Navier-Stokes equations (equations 3.2 and 3.3) are appropriate to describe turbulent flow. Therefore, the simplest numerical approach to study turbulent flow is to solve the NavierStokes equations without further modelling assumptions for the flow variables by integration in time. This requires, that all scales of the turbulent flow are resolved jointly with appropriate boundary and initial conditions. In particular, the largest scales need to be resolved by considering domains large enough to minimise boundary effects as well at a resolution fine enough to simulate the dissipation of energy at the smallest scales. It is important to note, that the scales of turbulence have to be resolved not only in space but also in time. That is, the time discretisation needs to be fine enough to resolve the smallest time scales in the flow while at the same time the flow needs to evolve long enough to assess the influence of the largest time scales.

The duration of a simulation depends on several aspects. When the statistically stationary state of a flow configuration is of interest, the flow field must evolve long enough from its initial state for the initials effects to be small (cf. section 3.1.2). Once the statistically stationary state of a flow configuration is reach, the flow field often needs to be advanced in time over a certain period to obtain converged statistics. The duration of the latter depends on the statistics of interest, on the flow configuration and also on the discretisation of the flow field. For example, the number of samples of one-dimensional flow statistics in open channel flow can be increased by additionally averaging over the homogeneous direction. Therefore, the needed observation time of the simulation might be small for large computational domains.

The requirements regarding the resolution in time and space and the duration to obtain converged statistics make DNSs computationally expensive. For example, the total number of grid points to meet the required spatial resolution in homogeneous isotropic turbulence is approximately proportional to the square of Reynolds number, $Re$, (i.e., more precisely $Re^{9/4}$ Pope (2000)). The computational effort scales with $Re^3$ when the efforts related with the required duration to collect statistics are included. This shows that the costs of DNS increase rapidly with the Reynolds number. The major limitation related to study turbulent flow phenomena by DNS comes from the amount of computational expenses one is willing or able to spend. Despite the immense costs, latest DNS for channel flow (Hoyas & Jiménez (2006)) or for boundary layer (Jiménez *et al.* (2010)), reached Reynolds numbers that can be considered moderate. The total costs of each of those simulation is immense and of the order of several millions of CPU hours. Commonly, these simulations require a run-time of several months up to a year on high performance computers. The reward of these efforts is a wealth of data which is difficult, if not impossible, to obtain otherwise.

Since the papers of Kim *et al.* (1987) and Spalart (1988) DNS has been established as a research tool. It was shown that the results of experiments and DNS are indistinguishable for a common setup, although the problem of realising boundary conditions in an experiment or a simulation remains (Moin & Mahesh (1998)). In recent years, experimental and numerical studies complement each other and both approaches inspired research activities. Certain questions that arose from, but could not be answered within, experiments, were answered by numerical studies and vice versa. Each approach has its strength and unique possibilities. On one hand, the range of Reynolds numbers that can be explored in experiments is generally larger compared to the one in DNS. Similarly, a parameter study for a certain flow configuration can often be carried

out at lower costs in experiments. On the other hand, a DNS provides a detailed high-fidelity picture of the flow. In particular, all flow quantities are provided in high resolution in space and time. Another benefit of DNS is that modified equations or artificial boundary conditions can be realised to test a hypothesis or study certain aspects of turbulence (Jimnez & Moin (1991); Jiménez & Pinelli (1999); Flores & Jimeńez (2006)).

To conclude, direct numerical simulation has been established as a research tool since many years (Moin & Mahesh (1998)). The computational costs and time requirements related to DNS are immense and limits its use to low or moderate Reynolds numbers. However, the simulations provide a wealth of data which would be difficult to obtain otherwise. In that sense, DNS complement experiments and are equally important to advance the understanding of turbulent flows.

### 3.3.3 Numerical method and validation

This thesis presents direct numerical simulations of turbulent flow over fixed heterogeneous and mono-dispersed particles. The simulations were carried out with the numerical code CHNL developed by Sivaramakrishnan Balachandar. The numerical method is documented in several journal publications (Balachandar (1989); Balachandar & Maxey (1989); Zhou *et al.* (1996)) as well as in a series of technical reports that provide additional detailed information on the numerical method (Balachandar & Maxey (1989); Balachandar (1989)).

The numerical method is based on a fractional-step method to numerically solve the incompressible NavierStokes equation. The temporal discretisation is semi-implicit, based on the CrankNicolson scheme for the viscous terms and a low-storage three-step RungeKutta procedure for the non-linear part (Verzicco & Orlandi (1996)). The spatial operators are evaluated by central finite differences on a staggered grid. The temporal and spatial accuracy of this scheme is of second order.

A variant of the immersed boundary technique (Peskin (1973)) proposed by Uhlmann (2005) is employed to discretise a wall roughened by spheres or mobile spheres moving freely in the flow. This method employs a direct forcing approach, where a localised volume force term is added to the momentum equations 3.3. The additional forcing term is explicitly computed at each Runge-Kutta sub-step as a function of the no-slip condition at the particle surface, without recurring to a feed-back procedure. The necessary interpolation of variable values from Eulerian grid positions to particle related Lagrangian positions (and the inverse operation of spreading the computed force terms back to the Eulerian grid) are performed by means of the regularised delta function given by Roma *et al.* (1999).

All simulations carried out with CHNL in this thesis employ a Cartesian grid with uniform isotropic mesh widths, i.e., $Dx = Dy = Dz$. This ensures that the regularised delta function verifies important identities, such as the conservation of the total force and torque during interpolation and spreading (Roma *et al.* (1999)). For reasons of efficiency, forcing is only applied to the surface of the spheres, leaving the flow field inside the particles to develop freely.

In cases with freely moving particles the particle motion is determined by the Runge-Kutta discretised Newton equations of 3.9 to 3.10, which are explicitly coupled to the fluid equations. The hydrodynamic forces on a particle are readily obtained by integrating the additional volume forcing term over the particles boundary. Thereby, the exchange of momentum between the two phases cancels out identically and no spurious contributions are generated. The analogue

procedure is applied for the computation of the hydrodynamic torque driving the angular particle motion.

During the course of a simulation, particles can approach each other closely. However, very thin inter-particle films cannot be resolved by a typical grid and therefore the correct build-up of repulsive pressure is not captured which in turn can lead to possible partial overlap of the particle positions in the numerical computation. In the present study a contact model is applied to prevent such nonphysical situations.

The numerical methodology has undergone most extensive testing in order to guarantee high quality results (Uhlmann (2005, 2006)). Further credibility of the numerical method can be gained from the work of other researches which implemented the immersed boundary method in similar numerical frameworks (Lucci *et al.* (2010); Lee & Balachandar (2010)). In particular Lee & Balachandar (2010) provide detailed validation studies on the numerical method and give information on the accuracy of drag and lift with respect to spatial resolution. The authors compare the results from the immersed boundary method with the results of a spectral element code. It might be noted that the immersed boundary method employed to discretise the particles in the present study became popular in the past years, in particular it is described in a recent textbook on the subject (Loth (2008)). In addition to the validations above, an effort was made to compare the result in this thesis to data from the literature wherever possible to further validate the present approach. The agreement is generally good and consistent with the literature.

*"Study hard what interest you the most in the most undisciplined, irrelevant and original manner possible"*

Richard Feynman (1918 - 1988)

# 4

# Open channel flow over fixed spheres at low relative submergence

In this chapter turbulent open channel flow over an array of fixed monodispersed articles are studied and compared to systematic lattice bed by Clemens *et al.* (2011). The results of two direct numerical simulations are analysed with special focus on the characterisation of force and torque on particles as well as the characterisation of flow structures related to force and torque. The setup of the simulations is described. The flow field is analysed in terms of flow field statistics and the three-dimensional time-averaged flow field. Sections 4.3 focus on the characteristics of force and torque and the characterisation of flow structures related to force and torque by discussing the statistics of particle force and torque, correlation functions of particle quantities in time and space-time and correlation functions between flow field and particle quantities. A summary, conclusions and recommendation for future work are given at the end.

## 4.1 Numerical setup

The flow configuration consists of turbulent open channel flow over a geometrically rough wall. The wall is formed by multiple layers of fixed spheres which are dispersed randomly (see figure 4.1). The distance between the particle centres is $D + 2\Delta x$, where $D$ is the particle diameter and $\Delta x$ is the grid spacing. The physical and numerical parameters of the simulations are summarised in table 4.1. The computational domain dimensions are $L_x/H \times L_y/H \times L_z/H = 4 \times 2 \times 1$, in streamwise, wall-normal and spanwise direction, respectively (cf. figure 4.1). An equidistant Cartesian grid with $512 \times 1024 \times 488$ grid points is employed.

One important parameter for the present flow configuration is the ratio between the domain height, $H$, and the spheres diameter, $D$. Ideally, a large $H/D$ is desirable to ensure that the spheres can be considered as roughness and not as obstacles in a channel (Jimeńez (2004)). However, from a practical point of view it is difficult to reach large values of $H/D$ without

| Run | $\frac{U_b h}{u_\tau}$ | $\frac{H}{D}$ | $Re_{bH}$ | $Re_\tau$ | $D^+$ | $\Delta_x^+$ | $\frac{L_x}{H}$ | $\frac{L_y}{H}$ | $\frac{L_z}{H}$ | $\frac{D}{\Delta_x}$ | $N_p$ | $\phi$ |
|---|---|---|---|---|---|---|---|---|---|---|---|---|
| P800 | 6.3 | 4 | 1875 | 300 | 84 | 1.1 | 2 | 4 | 1 | 14-70 | 800 | 0.43 |
| M1015 | 5.9 | 4 | 1760 | 300 | 77 | 1.1 | 2 | 4 | 1 | 40 | 1015 | 0.63 |

Table 4.1: Parameters for the two simulations. $U_{bH}$ denotes the bulk velocity based on the domain height $H$, $u_\tau$ is the friction velocity, $Re_b = U_{bH}H/\nu$ is the bulk Reynolds number with the kinematic viscosity $\nu$, $Re_\tau = u_\tau h/\nu$ is the friction Reynolds number, $D^+ = Du_\tau/\nu$ is the particle diameter in viscous units, $D/\Delta_x$ is the resolution of a particle, $\Delta_x^+$ is the grid spacing in viscous units, $N_x$, $N_y$ and $N_z$ denote the number of grid points in the spanwise, streamwise and wall-normal directions, $N_p$ is the total number of particles in the disperse distribution

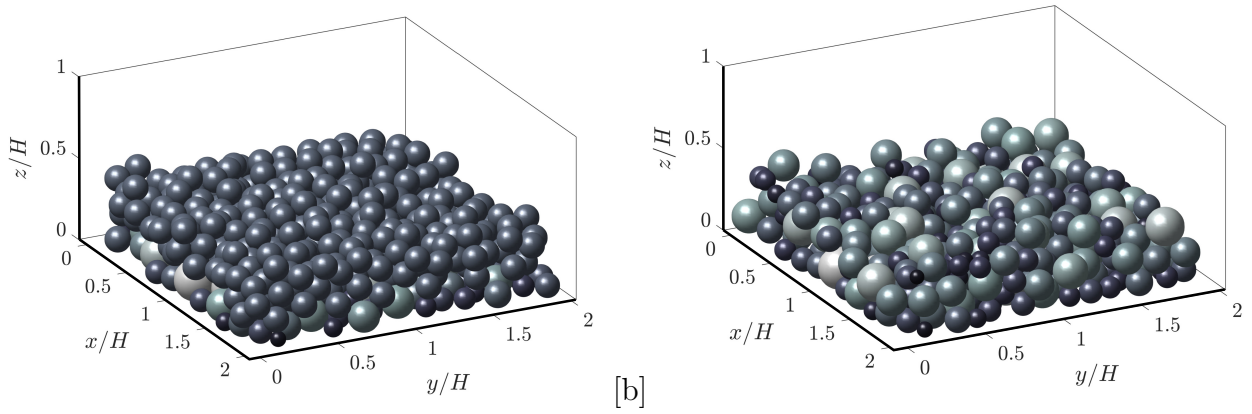



Figure 4.1: Close-up of a section of the computational domain with the geometry of the bottom wall consisting of a layer of fixed randomly dispersed spheres: (a) case M1015; (b) case P800.

increasing excessively the computational cost. Here, two cases are considered: Polydisperse case P800 with $H/D = 3$ and a total of 800 particles and Monodisperse case M1015 with $H/D = 2.7$ and a total of 1015 particles above the wall. Periodic boundary conditions are applied in streamwise and spanwise directions. At the upper boundary a free-slip condition is employed. At the bottom boundary a no-slip condition is applied. The spheres are resolved using the immersed boundary.

Figures 4.2 show the complexity of the flow in both cases. The flow field is visualised by a slice of the instantaneous streamwise velocity. Although the size of the spheres in case P800 are different than in case M1015, the overall picture is similar. In order to scale the results, two quantities need to be specified: the friction velocity, $u_\tau$, and the location of the virtual wall, $z_0$, since for a geometrically rough wall the position of the wall cannot be unambiguously defined (Townsend (1965); Raupach *et al.* (1991)). Here we have chosen to define the position of the virtual wall as $z_0 = 0.8D$ throughout this study. The value of $u_\tau$ is defined by extrapolating the total shear stress $\tau_{tot} = \rho_f \nu \partial\langle\bar{u}\rangle/\partial z - \rho_f\langle u'v'\rangle$ from above the roughness layer (where it varies linearly) down to the location of the virtual wall, $z_0$. Here, $\nu$ is the kinematic viscosity and $\rho_f$ is the fluid density.

The effective flow depth, $h$, can be defined as the distance from the virtual wall to the top boundary, $h = H - z_0$. The bulk velocity based on the domain height, $H$, is defined as $U_{bH} = 1/H \int_0^H \langle\bar{u}\rangle dz$, the bulk velocity based on the effective flow depth is defined as

$U_{bh} = 1/h \int_0^H \langle \bar{u} \rangle dz$. In the following angular brackets with sub-indexes, $\langle \cdot \rangle_{t,x,y,z,b,p}$, are used for averaging over time ($t$) along a certain coordinate direction ($x, y, z$) over periodically repeating boxes of geometry ($b$) and over the particle related data ($p$) respectively. Angular brackets without additional indexes, $\langle \cdot \rangle$, refer to quantities which are averaged over time as well as spatially over wall-parallel planes, i.e., along the $x$ and $y$ directions. The deviation of the instantaneous value of a quantity, $\phi$, to the averaged value $\langle \phi \rangle$ is indicated by a prime as super index, e.g. $\phi'$. When the root mean square value of a quantity is considered the sub-index rms is used, e.g. $\phi_{rms}$.

The frictional Reynolds number, $Re_\tau = u_\tau h/\nu$, was kept constant at a value of 300 in cases P800 and M1015, respectively. The grid resolution of the simulation was in both cases approximately equal to the viscous length $\delta_v = \nu/u_\tau$ in all spatial directions. The resolution can therefore be qualified as exceptionally fine away from the wall and as reasonably fine in the vicinity of the rough wall. In the following, normalisation of a quantity, $\phi$, with wall units will be denoted by a superscript +, e.g. $\phi^+$. Examples of two-point correlations of velocity and pressure at indicated $z^+$-location and energy spectra are shown in figure 4.4 and 4.5 to illustrate the adequacy of the computational domain and grid resolutions. In figures 4.5, $k_x$ and $k_y$ are the wavenumbers in the spanwise and streamwise directions respectively. In figure 4.4, the two-point correlation in the $x$ and $y$ directions at two $z^+$ locations, one very close to the wall and the other close to the centreline show that they fall to zero values for large separations, indicating that the computational domain is sufficiently large. The energy spectra shown in figure 4.5, illustrate that the grid resolution is adequate, since the energy density associated with the high wavenumbers is several decades lower than the energy density corresponding to low wavenumbers, and there is no evidence of energy pile-up at high wavenumbers.

The initial turbulent flow field of each simulation was taken from a similar simulation on a coarser grid. Subsequently, the simulation was run until the flow reached a statistically stationary state. The simulation was then continued for $\tau_c U_{bH}/H$ as shown in table 4.1 during which flow field statistics as well as particle data such as forces and torques were collected. Entire flow fields jointly with the particle data were stored at intervals of about $H/U_{bH}$. Based on these data a statistical analysis has been carried out. If not explicitly stated otherwise, the statistics shown for cases $P800$ and $M1015$ stem from the data collected during the runtime of the simulation and are averaged over the entire domain including the region within the particles.

## 4.2 Flow field characteristics

### 4.2.1 Flow field statistics

Figure 4.6 shows the profiles of the time and plane averaged streamwise velocity component, $\langle u \rangle$, as a function of the vertical coordinate. The results of case P800 and case M1015 are compared with the reference case of Clemens *et al.* (2011) and S180 of a smooth wall open channel flow at $Re_b = 2880$ and $Re\tau = 180$, which has been taken from Kim *et al.* (1987). The profiles show the expected effect of roughness that is described in various textbooks (Schlichting (1936*b*) and Pope (2000)). As the particle diameter $D$ increases, while keeping the value of the frictional Reynolds number $Re_\tau$ constant, the streamwise velocity profile normalised by outer scales flattens (figure 4.6a), and the streamwise velocity profile normalised by viscous

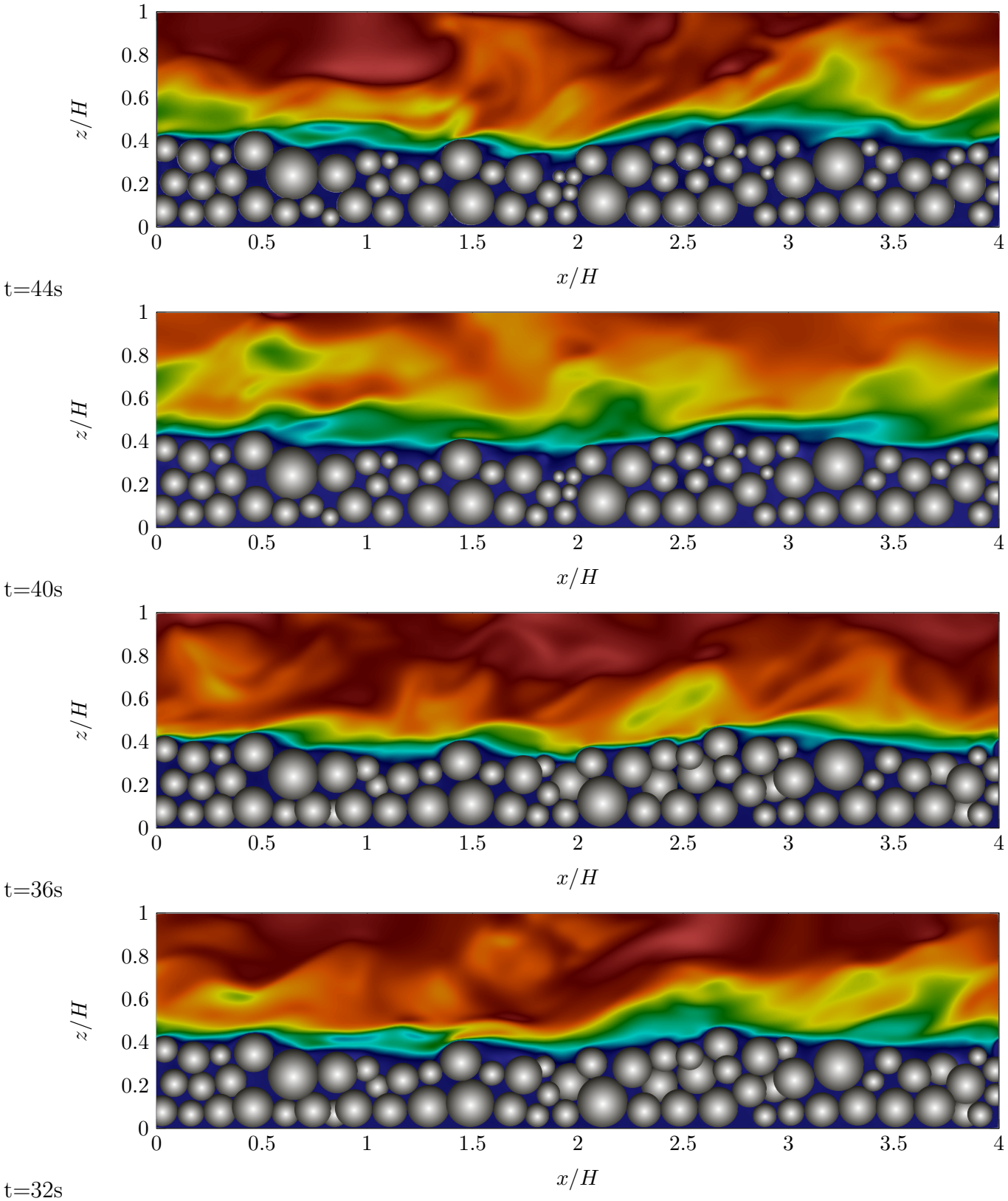



Figure 4.2: Side view of the instantaneous flow field in the case P800 at different times.

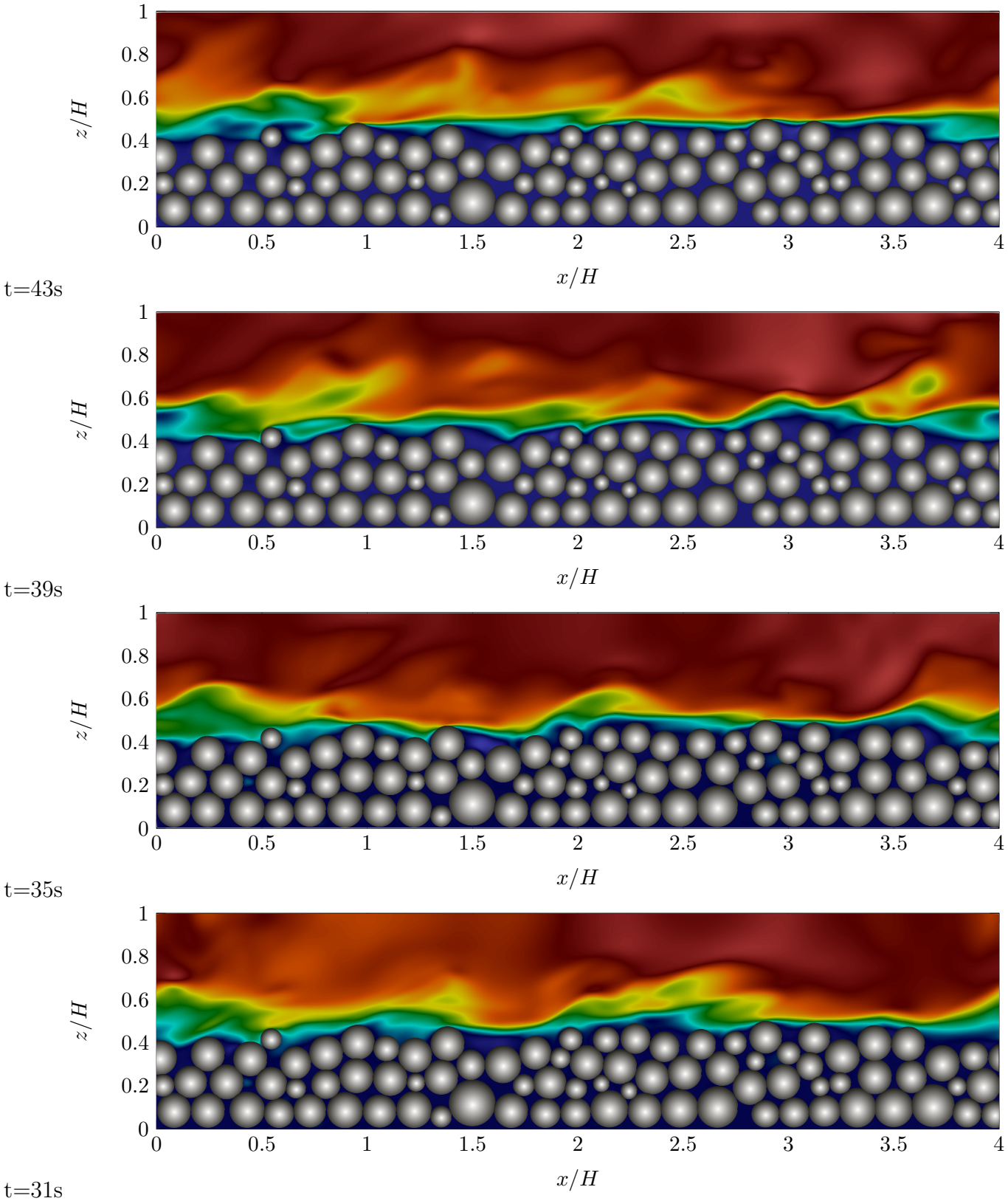



Figure 4.3: Side view of the instantaneous flow field in the case M1015 at different times.

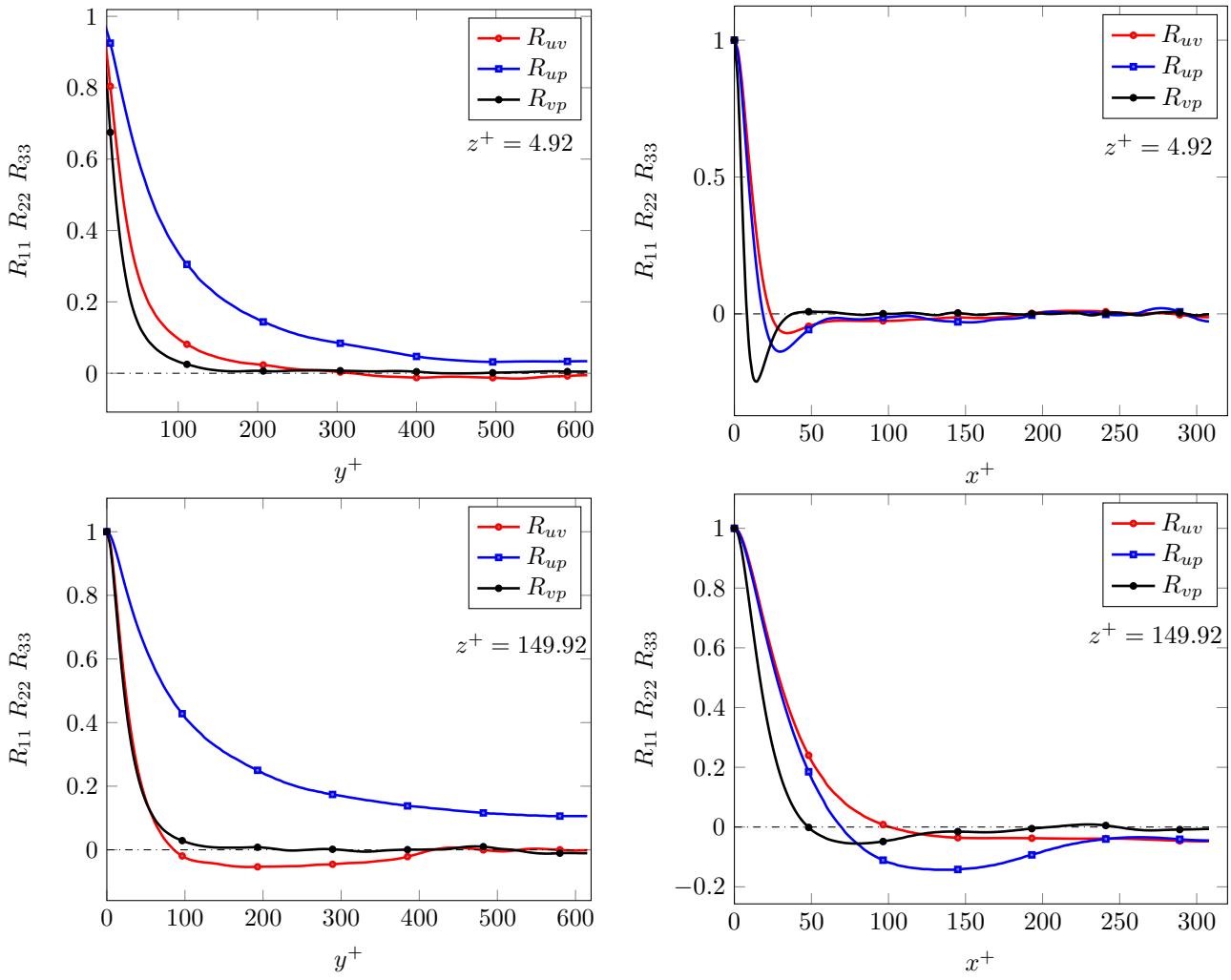



Figure 4.4: Two-point correlations $R_{uu}$, $R_{vv}$ and $R_{ww}$ of streamwsie and spanwise seperations

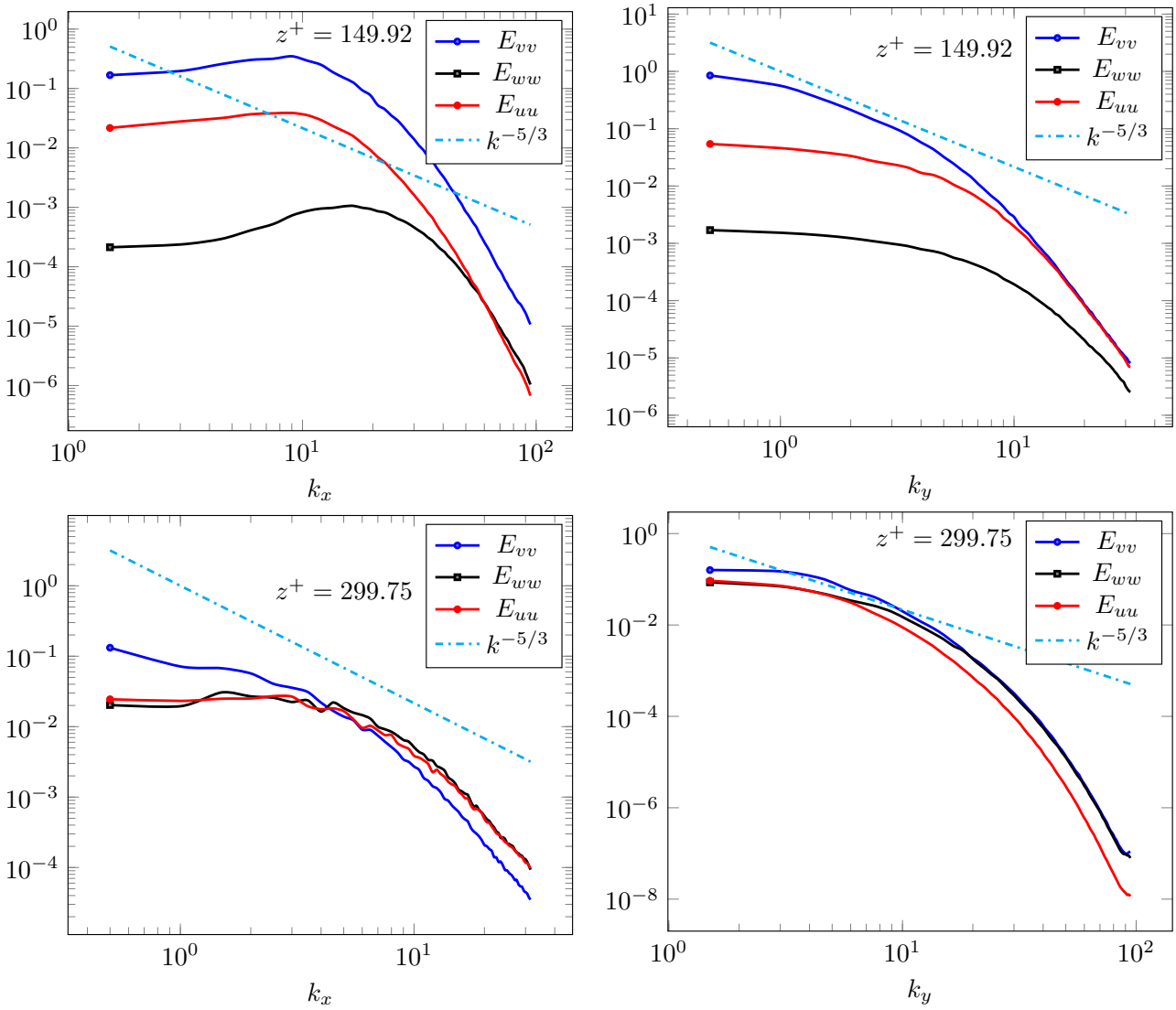



Figure 4.5: One-dimensional energy spectra in the spanwise $x$ and streamwise $y$ directions respectively.

scales increasingly shifts towards lower values of $\langle u \rangle^+$ (figure 4.6b). Figure 4.6 shows that a logarithmic layer exists, if at all, only over a small range due to the low Reynolds number considered. The logarithmic law for the flow over a rough wall can be written as in the case of a smooth wall with an additional offset $\Delta U^+$ that accounts for the roughness effect

$$\langle \bar{u}^+ \rangle = \frac{1}{k} \ln \left( \frac{z - z_0}{\delta_\nu} \right) + A - \Delta U^+ \tag{4.1}$$

where the von Karman constant, $\kappa$, and $A$ are constants obtained empirically to be $\kappa \approx 0.4$ and $A \approx 5.1$ (according to experimental findings summarised e.g. in Jimeńez (2004)). From the profiles in figure 4.6 it appears that in case M1015 the roughness effect is weak, while in case P800 a stronger roughness effect can be seen. It is customary to quantify the roughness effect by using the equivalent sand grain roughness $k_s$ (Schlichting (1936*a*)). It can be obtained by a fit to the mean velocity profile in the logarithmic layer using the following equation

$$\langle \bar{u}^+ \rangle = C \log_{10} \left( \frac{z - z_0}{k_s} \right) + B \tag{4.2}$$

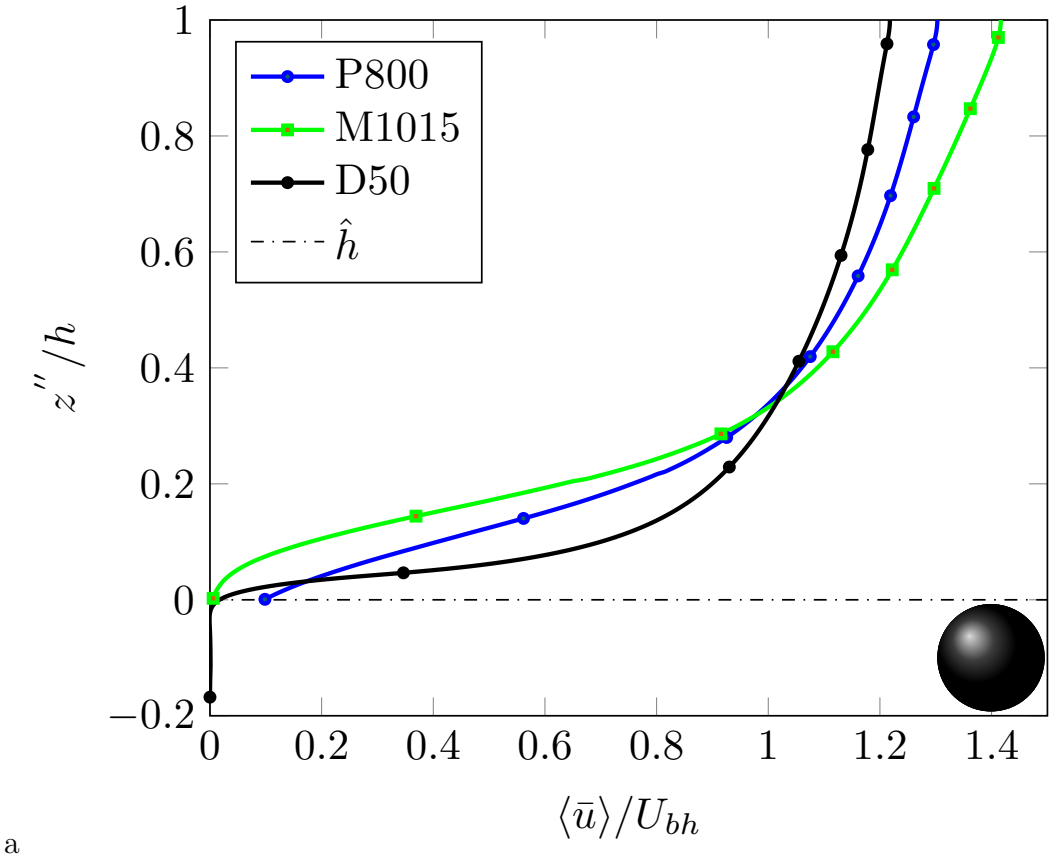
Here, the values of $B \approx 48$ and $C = 1/\kappa \ln(10) \approx 5.75$ are empirically obtained (Shockling *et al.* (2006). At high enough Reynolds numbers $k_s$ becomes constant, i.e. $\lim_{Re \to \infty} = k_{s\infty}$, defining the so called fully rough flow regime. The specific value of $k_{s\infty}$ is a quantity of the surface that depends on the characteristics of the roughness, such as shape, arrangement or roughness area ratio. Flow over roughness can be classified as hydraulically smooth, transitionally rough or fully rough according to a small, moderate or high value of $k_{s\infty}$. Nikuradse (1933) gave values of $5 < k_{s\infty} < 70$ to define the transitionally rough flow regime. However, these values should be taken with care as the transition might be influenced by the specific characteristics of the roughness (discussion in Bradshaw (2000); Jimeńez (2004); Shockling *et al.* (2006), among others). In particular, it has been speculated that a uniformly sized, structured arrangement of roughness elements as in the present case might lead to a sharp transition from hydraulically smooth to the fully rough regime (Colebrook *et al.* (1939); Jimeńez (2004)).

Figure 4.7 shows the transition from the hydraulically smooth flow regime to the fully rough flow regime obtained in different experiments. It shows the offset $\Delta U^+$ as a function of $k_{s\infty}$. At low values of $k_{s\infty}$ the effect of roughness should be negligible and correspondingly $\Delta U^+$ approaches zero. In the fully rough flow regime, the roughness effect should purely depend on k+ s. By comparison of equation 4.1 and 4.2, a formula for $\Delta U^+$ can be derived for the fully rough regime,

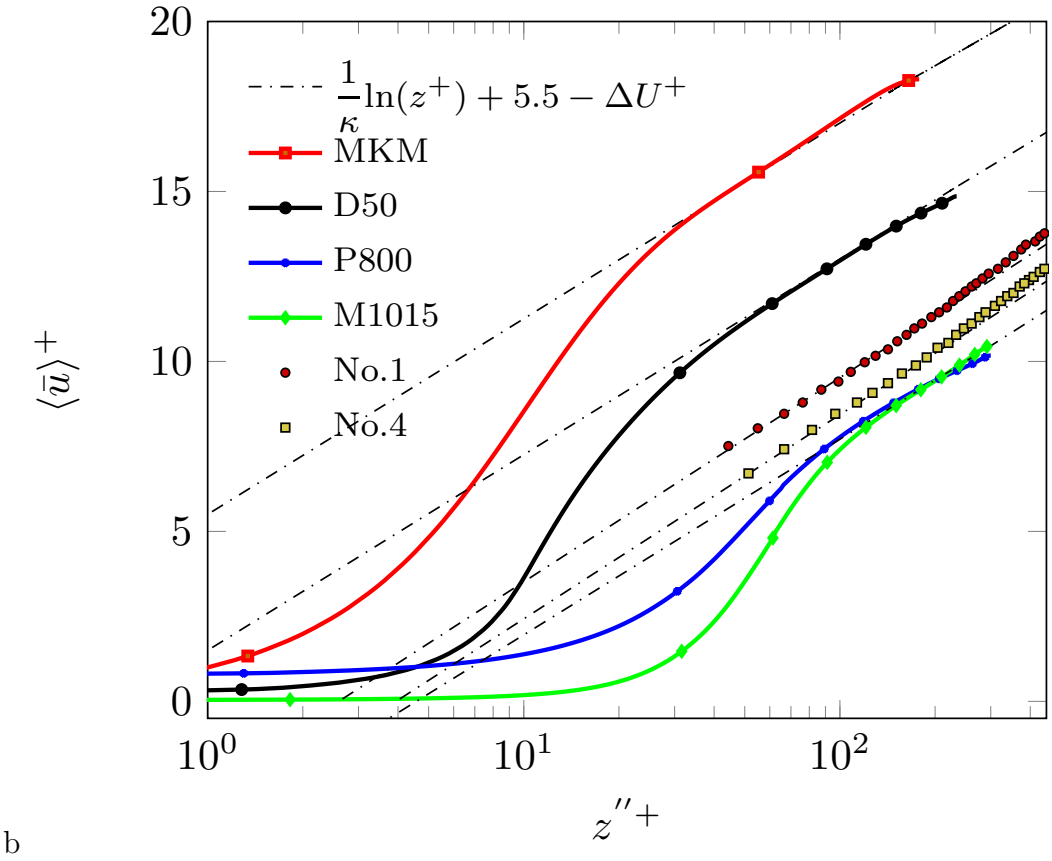
$$\Delta U^+ = C \ \log_{10}(k_{s\infty}) - B + A \tag{4.3}$$

with the constants A, B and C as above. The relation 4.3 above is shown in figure 4.7 jointly with results from experiments.

For the present simulations the values of $\Delta U^+$ can be obtained by the vertical shift of the mean velocity profiles in the log-region of figure 4.6b. They are 1.03 and 4.85 for cases M1015 and P800, respectively. However, the value of $k_{s\infty}/D$ for the present arrangement of spheres is unknown. Schlichting (1936*a*), Ligrani & Moffat (1986) and Pimenta *et al.* (1975) found a value of $k_{s\infty}/D = 0.63$ for flow over spheres in hexagonal packing, while somewhat larger values were obtained by Singh *et al.* (2007) ($k_{s\infty}/D = 0.77$) and Detert *et al.* (2010) ($k_{s\infty}/D = 0.81$). For




a




b

Figure 4.6: Time and spatially averaged streamwise velocity component $\langle u \rangle$, of the case P800 and case M1015 in comparison with smooth wall open channel flow and Clemens *et al.* (2011). (*a*) Normalised with $U_{bh}$ as a function of $(z - z_0)/h$, (*b*) in semi logarithmic scale normalised by $u_\tau$. The position of the particles top are marked with horizontal (*a*) dot and dashed line.

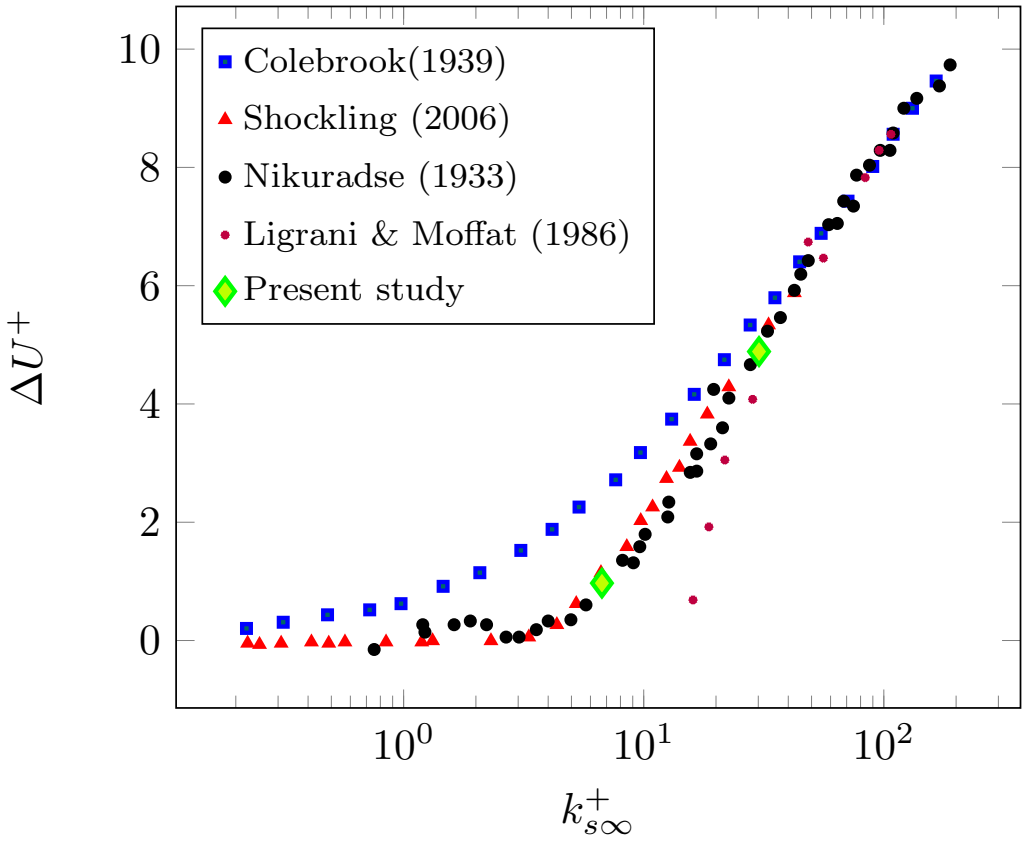



Figure 4.7: Roughness function for several transitionally rough surfaces as a function of the Reynolds number $k_{s\infty}^+$, adapted from Jimeńez (2004).

flow over spheres in random packing, the obtained values vary in the range of $k_{s\infty}/D = 0.55$ to 0.85 (Grass *et al.* (1991)). Few studies exist that use values of $k_{s\infty}/D = 1$ for structured (Einstein & El-Samni (1949)) or random arrangements (Nakagawa & Nezu (1977)). Figure 4.7 shows the pair of values $(k_{s\infty}^+/\Delta U^+)$ for cases M1015 and P800 when approximating $k_{s\infty}/D$ by the value found for a hexagonal packing, i.e. $k_{s\infty}/D = 0.63$. It can be seen that case M1015 approaches the hydraulically smooth flow regime while case P800 is in the transitionally rough flow regime.

A similar conclusion can be reached by analysing the profiles of the root-mean-square of the velocity fluctuations normalised with $u_\tau$ that are shown in figure 4.8a, and 4.9a and b. In case M1015 and P800 the profiles of the three velocity components, where the differences with respect to the case of Clemens *et al.* (2011) are evident. The near wall peak in the streamwise fluctuation profile decreases but it is still visible. This indicates that the flow is in the transitionally rough flow regime, since experiments in the fully rough flow regime present no clear peak (see for example figure 5 of Jimeńez (2004)). The wall-normal and spanwise fluctuations present slightly higher values near the wall than the corresponding ones in the case of Clemens *et al.* (2011). Therefore, the anisotropy of the fluctuations near the wall is smaller than in the smooth wall case. This tendency of roughness to make the fluctuations more isotropic is a phenomenon which has been often reported in the literature (Poggi *et al.* (2003); Orlandi & Leonardi (2008)).

Orlandi & Leonardi (2008) discuss the velocity shift $\Delta U^+$ as a function of the root mean square value of the wall-normal velocity fluctuations, $\nu_{rms}$, at the roughness crest. The present

simulations result in pairs $(\nu_{rms}, \Delta U^+)$ of (0.10; 1.03) (0.46; 4.85) for case M1015 and P800 respectively which agree well within the scatter of the reported data (graph not shown).

Figure 4.8b shows the profiles of the Reynolds stress, $\langle u'v' \rangle$, normalised by $u_\tau^2$. The Reynolds stress profile $\langle u'v' \rangle$ of case M1015 nearly collapses with the profile of the P800 case. In case Clemens *et al.* (2011) a slight increase and a small shift towards the wall of the near-wall peak can be seen which could be an effect of the higher value of $Re_\tau$ in this case.

### 4.2.2 Three-dimensional time averaged flow field distribution

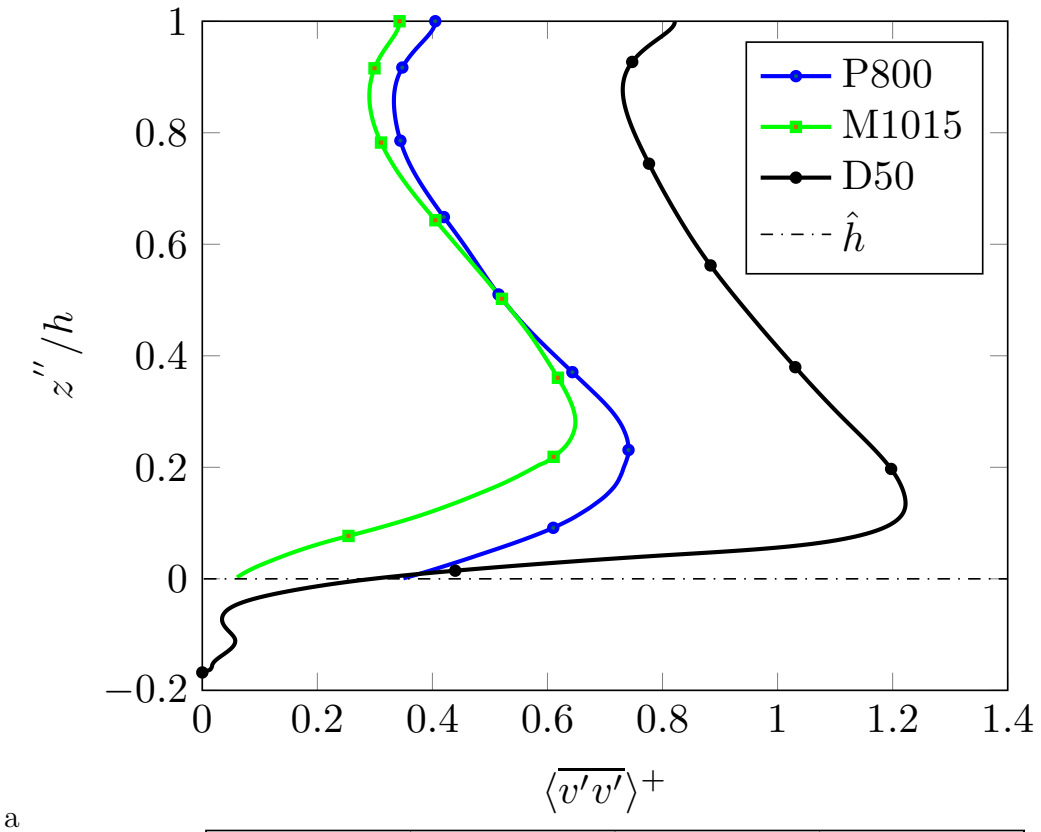
Since the geometry of the roughness is three-dimensional, the time-averaged flow field in the near wall region also varies in all three directions. In the following some characteristics of the time averaged flow field obtained from the flow fields collected during run-time of case M1015 and case P800 are discussed. In addition to the averaging in time the fields were averaged over periodically repeating boxes centered on the particles (henceforth indicated by the symbol $\langle \cdot \rangle_{tb}$). For simplicity, this will be simply referred to as time averaging below. Figure 4.10 shows the distribution of the three-dimensional time-averaged streamwise velocity, $\langle u \rangle_{tb}$, for both cases. As can be expected the flow field is very different from a single sphere in an unbounded turbulent flow or in a channel close to a wall (Bagchi & Balachandar (2003) and Zeng *et al.* (2008)).

The sheltering effect of the neighbouring particles causes the flow velocity to decrease rapidly close to the roughness tops and leads to marginal flow velocities within the roughness layer. The highest velocity gradients are produced near the roughness tops. Similar observations were made in the experiments of Pokrajac & Manes (2009) who studied a comparable particle arrangement at bulk Reynolds numbers of order $10^4$ and a ratio of $h/D \approx 3.5$. Also, like their results is the formation of a re-circulation between two spanwise rows of spheres that extends over the entire spanwise direction. The shape of the re-circulation is similar in both of our present cases; however the strength differs. In case P800, the backflow velocities reach values as low as $\langle u \rangle_{tb} \approx -0.4u_\tau$ and $\langle u \rangle_{tb} \approx -0.2u_\tau$. In case M1015 the magnitude of the backflow velocity is below $0.05u_\tau$.

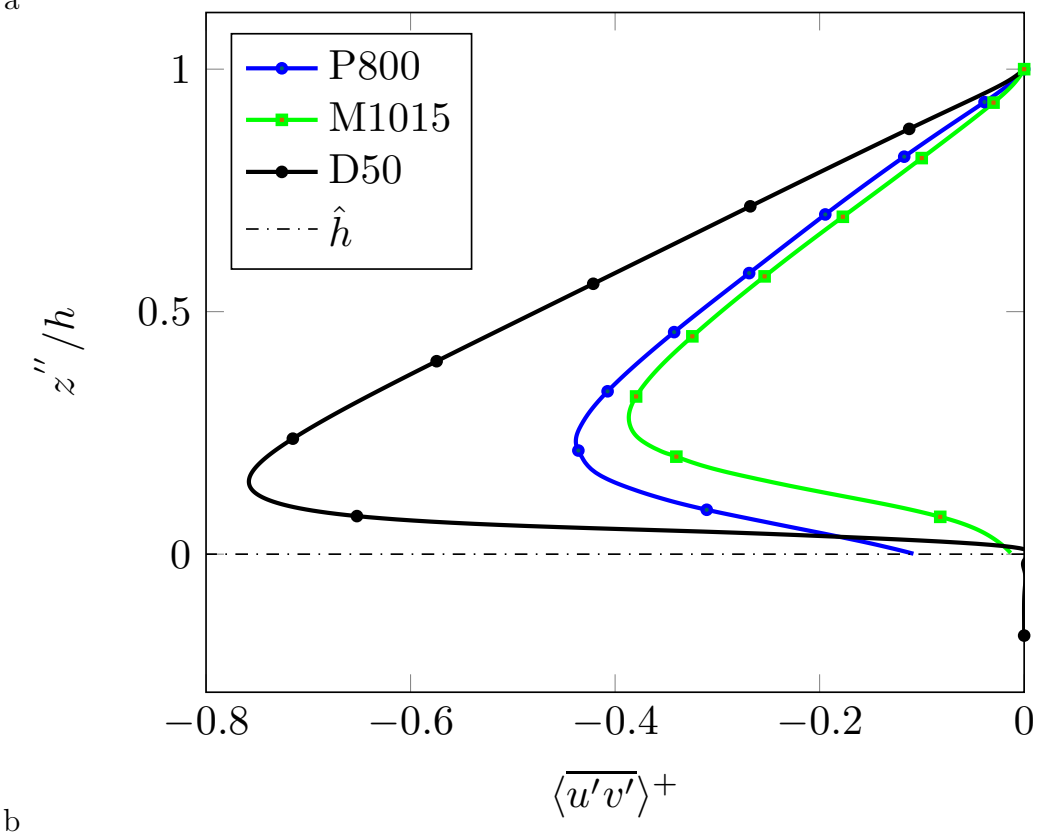
A question of interest is how far the three-dimensionality of the bottom wall directly influences the flow. Figure 4.10 already shows that one particle diameter above the roughness tops the time averaged pressure field is still visibly affected. To quantify the effect of three-dimensionality, the difference between the time-average of a field $\langle \phi \rangle_{tb}$ (where $\langle \phi \rangle$ can stand for either pressure or one of the velocity components) and its time and plane-averaged value, $\langle \phi \rangle$, can be defined:

$$\phi'' = \langle \phi \rangle_{tb} - \langle \phi \rangle \tag{4.4}$$

Note, that the quantity, $\phi''$, as defined by 4.4 is sometimes called spatial disturbance in the context of the double-averaging methodology (Nikora & McLean (2001)). The corresponding root-mean-square value of $\phi''$ can be computed using equation (4.4) as $\phi''_{rms} = \sqrt{\langle \phi'' \phi'' \rangle}$. In both cases, M1015 and P800, the standard deviation of velocity drops by several orders of magnitude in between $y = D$ and $y = 2D$. The same is true for the pressure field (not shown). Therefore, the time-averaged flow statistics appear to be essentially one dimensional beyond wall distances of 2D. This is somewhat smaller than the values reported in previous investigations of flow over rough walls (Jimeńez (2004)) which might be related to the low values of $D^+$ and $Re_\tau$ considered.

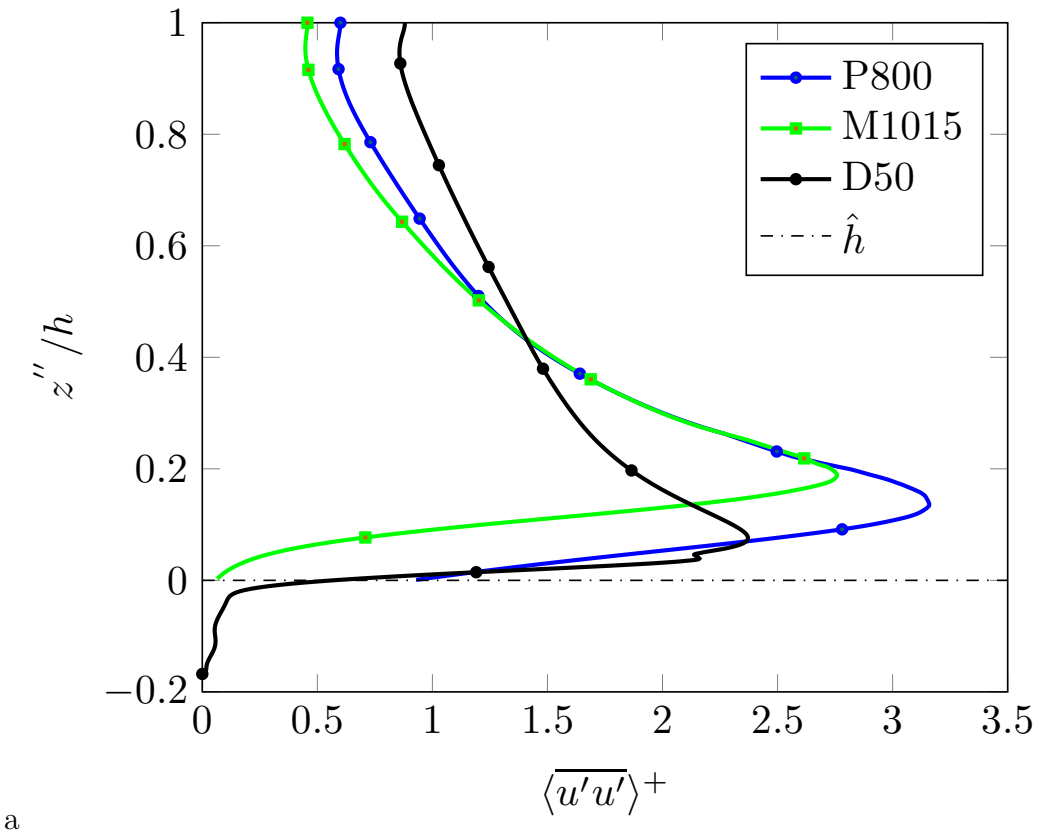



a

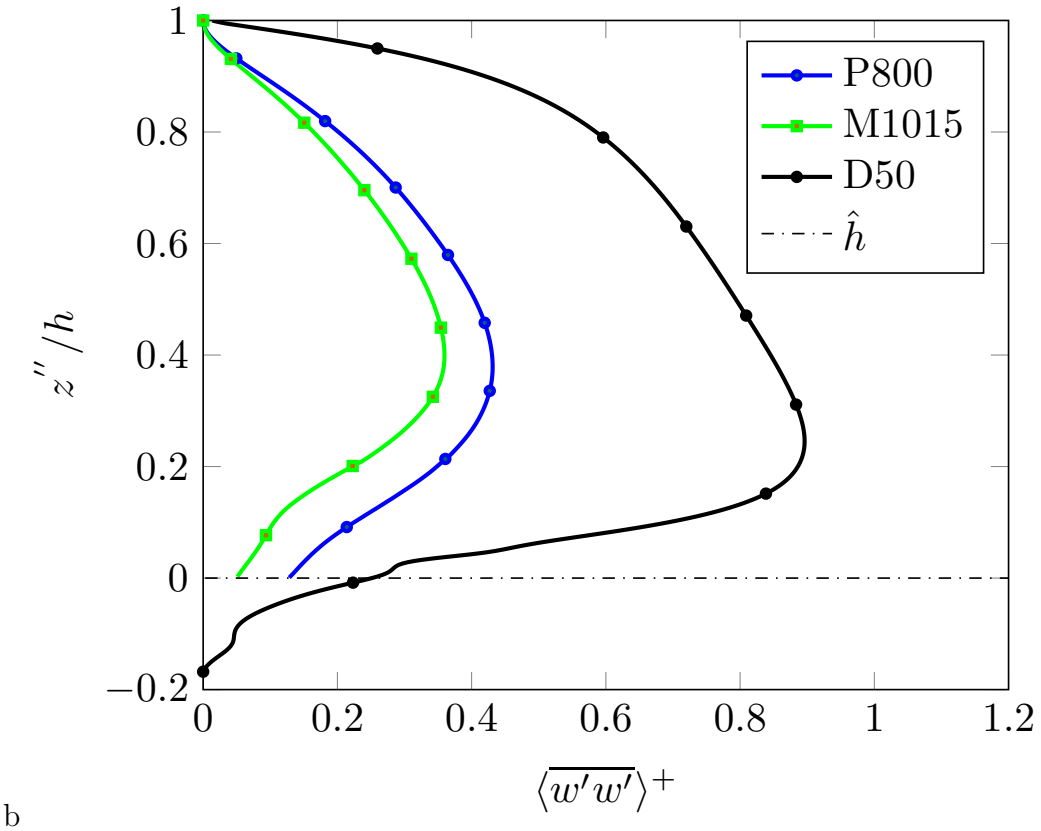



b

Figure 4.8: (a) Root-mean-square of velocity fluctuations of case M1015 and case P800 normalised by $u_\tau$ in comparison with results of Clemens *et al.* (2011) as a function of wall distance. (b) Distribution of Reynolds shear stress $u'v'$ as a function of wall distance.




a




b

Figure 4.9: Root-mean-square of velocity fluctuations of case M1015 and case P800 normalised by $u_\tau$ in comparison with results of Clemens *et al.* (2011) as a function of wall distance.

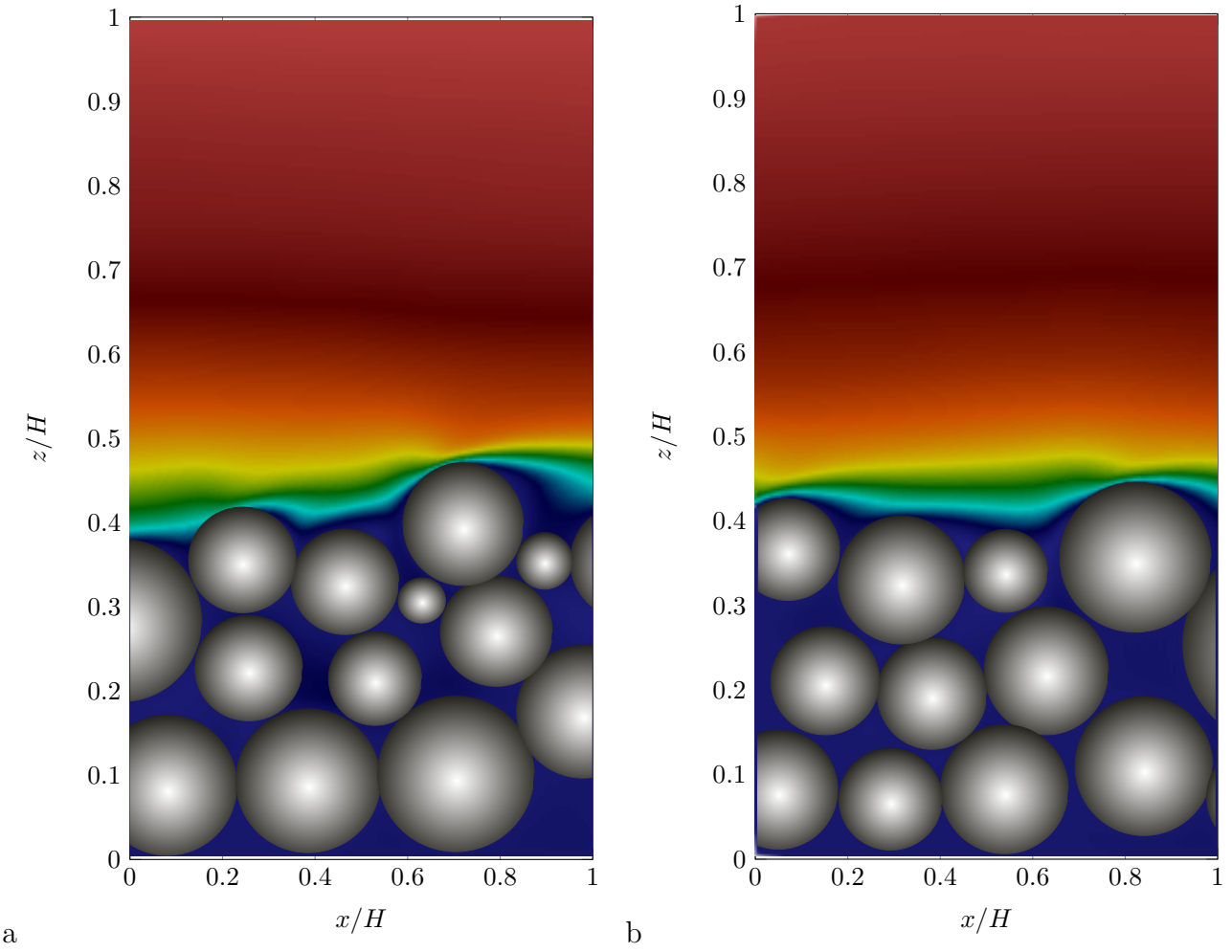



Figure 4.10: Distribution of the time averaged streamwise velocity, $\langle u \rangle$, normalised by $u_\tau$ in $z-x$ planes for the case P800 (a) and case M1015 (b). Plane through particles and not particle centres.

| Run | $C_{Fx}$ | $C_{Fy}$ | $C_{Fz}$ | $\alpha_F$ | $\sigma_{Fx}/F_R$ | $\sigma_{Fy}/F_R$ | $\sigma_{Fz}/F_R$ | $S_{Fx}$ | $S_{Fy}$ | $S_{Fz}$ | $K_{Fx}$ | $K_{Fy}$ | $K_{Fz}$ |
|---|---|---|---|---|---|---|---|---|---|---|---|---|---|
| M1015 | 1.04 | 0.19 | 0.00 | 11° | 0.57 | 0.20 | 0.66 | 0.18 | 1.80 | 0.01 | 10.13 | 19.08 | 9.92 |
| P800 | 1.15 | 0.37 | 0.00 | 18° | 1.32 | 0.66 | 1.26 | 0.06 | 0.26 | 0.01 | 4.98 | 5.68 | 4.29 |

Table 4.2: Statistics of force on particles in case M1015 and case P800, where $C_{Fi} = \langle F_i/F_R \rangle$ is the normalised mean force component in the $x_i$-direction, $\alpha = arctan(C_{Fy}/C_{Fx})$ is the angle of the resulting force with respect to the $x$-axis, $\sigma_{Fi}$ is the standard deviation of the force in $x_i$, $S_{Fi}$ and $K_{Fi}$ are the skewness and kurtosis of the respective force component.

## 4.3 Statistics of particle force

The hydrodynamic force, **F**, acting on a particle is defined as

$$F = \int_\Gamma \tau \cdot n d\Gamma - \int_\Gamma P^{tot} n d\Gamma \tag{4.5}$$

where $\Gamma$ is the spheres surface, **n** is the surface normal vector, $\tau = v\rho_f(\partial_j u_i + \partial_i u_j)$ is the viscous stress tensor and $P^{tot}$ is the pressure. The latter can be split into two parts $p^{tot} = p + p_l$, where $p_l$ represents the linear variation in streamwise direction which results from the imposed pressure gradient that drives the flow, and $p$ corresponds to the three-dimensional instantaneous fluctuation. The first term on the right-hand side of equation (4.5) is the force due to viscous stresses, the second term is the force due to pressure. A sketch that illustrates the definition of the force on a particle can be seen in figure 4.11

In order to scale the hydrodynamic forces, reference quantities need to be defined. For the present case of particles within a roughness layer the subject is a matter of discussion and several definitions have been proposed in the literature (see Hofland *et al.* (2005)). Here, the reference force is defined as $F_R = \rho_F u_\tau^2 A_R$ with the reference area $A_R = L_x L_z / N_p$.

Table 4.2 summarises the particle force statistics of the two cases, where $C_{Fi}$ is the mean force on a particle in $x_i$-direction normalised by $F_R$. As can be seen, the mean values of the forces acting in the streamwise direction (henceforth also called drag) and the wall-normal direction (lift) are positive. Since the mean forces are directly related to the mean flow through the time-averaged version of equation (4.5), it is possible to shed some light onto the mechanisms that lead to mean drag and lift by analysing figures 4.10.

The distribution on the spheres surface of the stress leading to drag, $\tau_D$, and lift, $\tau_L$, are calculated from

$$\tau_D = \Big( \langle \tau \rangle_t \cdot n - \langle p^{tot} \rangle_t n \Big) \cdot e_x, \tag{4.6}$$

$$\tau_D = \Big( \langle \tau \rangle_t \cdot n - \langle p^{tot} \rangle_t n \Big) \cdot e_y, \tag{4.7}$$

where $e_i$ is the unit vector in the $x_i$-direction.

The drag coefficient as defined in the present study can be approximated as:

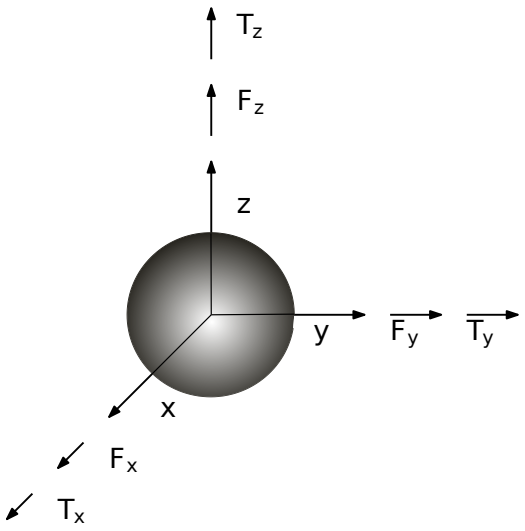



Figure 4.11: Sketch illustrating the definition of force $F_x, F_y, F_z$ and $T_x, T_y, T_z$ on a particle.

$$C_{Fx} \approx \frac{V_{fb} + V_p}{hA_R} \tag{4.8}$$

where $V_{fb}$ is, the total volume occupied by fluid in a periodic box around a particle, Vp is the volume occupied by a particle. The approximation 4.8 neglects the streamwise component of the shear force acting on the bottom wall in addition to the drag due to the periodic part of the pressure acting on the spherical caps. Evaluating this geometrical relation (4.8) yields 1.04 and 1.15 for case M1015 and P800.

Positive values for the lift coefficient, as observed in the present simulations (table 4.2), can be explained by two mechanisms. The approaching flow accelerates in the frontal part until the top of the sphere and from then on it decelerates. This fact is reflected in the curvature of the streamlines (figures 4.10a,b), yielding a pressure distribution which exhibits lower values of pressure near the particles tops, and therefore a positive lift. In addition to pressure, shear might lead to a positive lift. As can be seen in figure 4.10, the flow field above the spheres is asymmetric (with respect to a cross-sectional plane through the particle centres) because of the re-circulation behind the particles. Therefore, the friction on the upstream side of the particle (in the upper hemisphere) is expected to be higher compared to the corresponding friction on the downstream side, contributing positively to the lift on the particle. The pressure differences as well as the asymmetry of the flow seem to be more pronounced in case P800 than in case M1015 and might explain the observed increase in the lift coefficient.

In order to quantify the contribution integrated from the bottom of a particle up to a certain fraction of its diameter, we can define a cumulative function

$$\ell_\phi(z) = \frac{D}{2} \int_0^y \int_0^{2\pi} \tau_\phi(y, \theta) d\theta dy \tag{4.9}$$

where $\tau_\phi(y, \theta)$ stands for either $\tau_L$ or $\tau_D$ evaluated at a position on the spheres surface given by the wall-distance $y$ and an azimuthal angle $\theta$ in the wall-parallel plane. Figure 4.12 $\iota_D$ and $\iota_L$ normalised by the net values of lift and drag, respectively. The contribution to the net drag by the flow in the lower half of the sphere is small in both cases, the cumulative

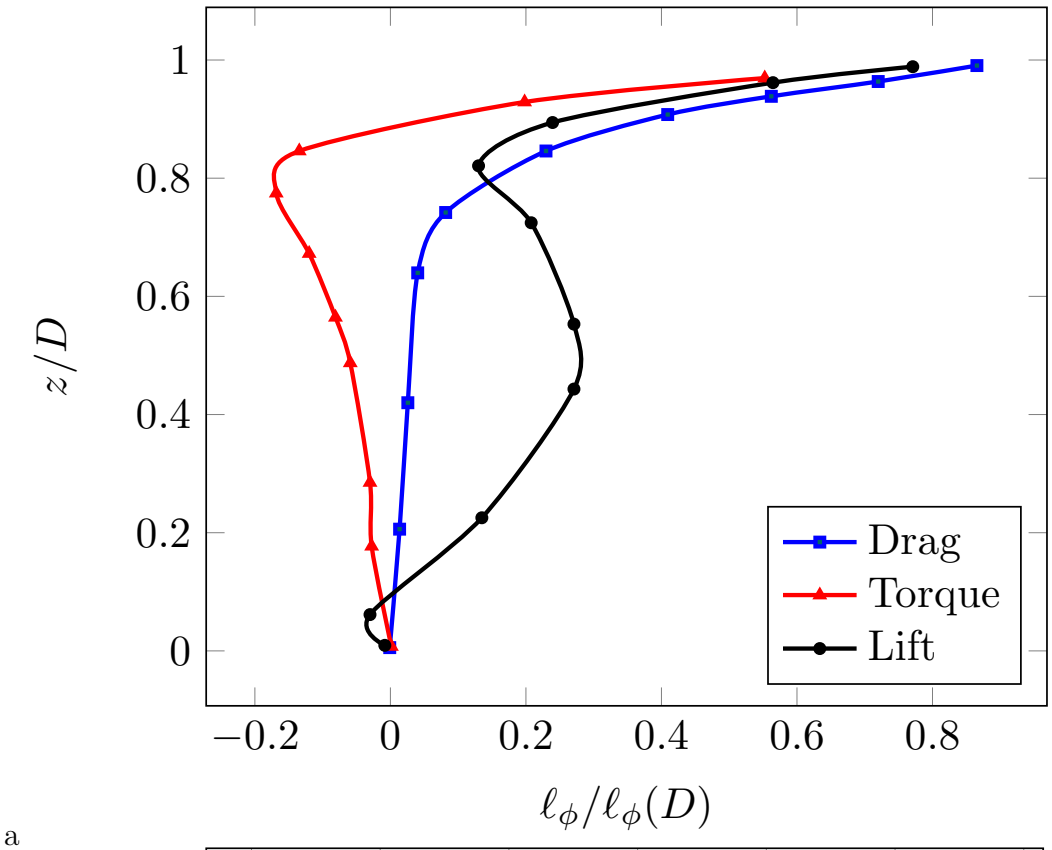
drag value increasing monotonically and with increasing slope from the wall to the top of the sphere. Conversely, the cumulative contribution to the lift first increases with increasing wall-distance up to values of approximately 25% (40%) of the total in case M1015 (P800) at $y \approx 0.5D$, before decreasing again to a small value at $y \approx 0.9D$. Beyond that, in a small area surrounding the top of the sphere, is where most of the net lift is generated. In case P800, the lift increases with respect to case M1015 more than the drag, which leads to a higher angle, $\alpha = arctan(C_{Fy}/C_{Fx})$, of the resulting force (table 4.2). The spanwise force should be zero for symmetry reasons. In both cases the calculated mean spanwise force coefficient is more than two orders of magnitude lower than the drag coefficient. This fact provides confidence in the convergence of the statistics.

Additional support to the mean forces just discussed is provided by comparison to experimental measurements performed in a somewhat similar configuration by Hall (1988). In that study, the mean lift on a particle near a boundary was measured in a wind tunnel with smooth as well as rough walls. The interesting case for the present discussion consisted of a sphere of diameter $D$ placed in between spanwise rods of diameter $D_r$ evenly spaced out with a distance $D_r$. Figure 4.13 presents the comparison of the mean lift normalised by $\rho_f v^2$ as a function of $D^+$, between the values obtained in the experiments of Hall (1988) and the present simulations. Despite the different setups, the lift obtained in case M1015 is perfectly consistent with the measurements while the lift obtained in case P800 is somewhat lower. The reason for this might be that in the setup of the simulations the neighbouring spheres are closer producing an increased sheltering effect. This is also supported by the experimental observation that lower lift values are obtained when the value of $D_r/D$ is increased (Hall (1988)).

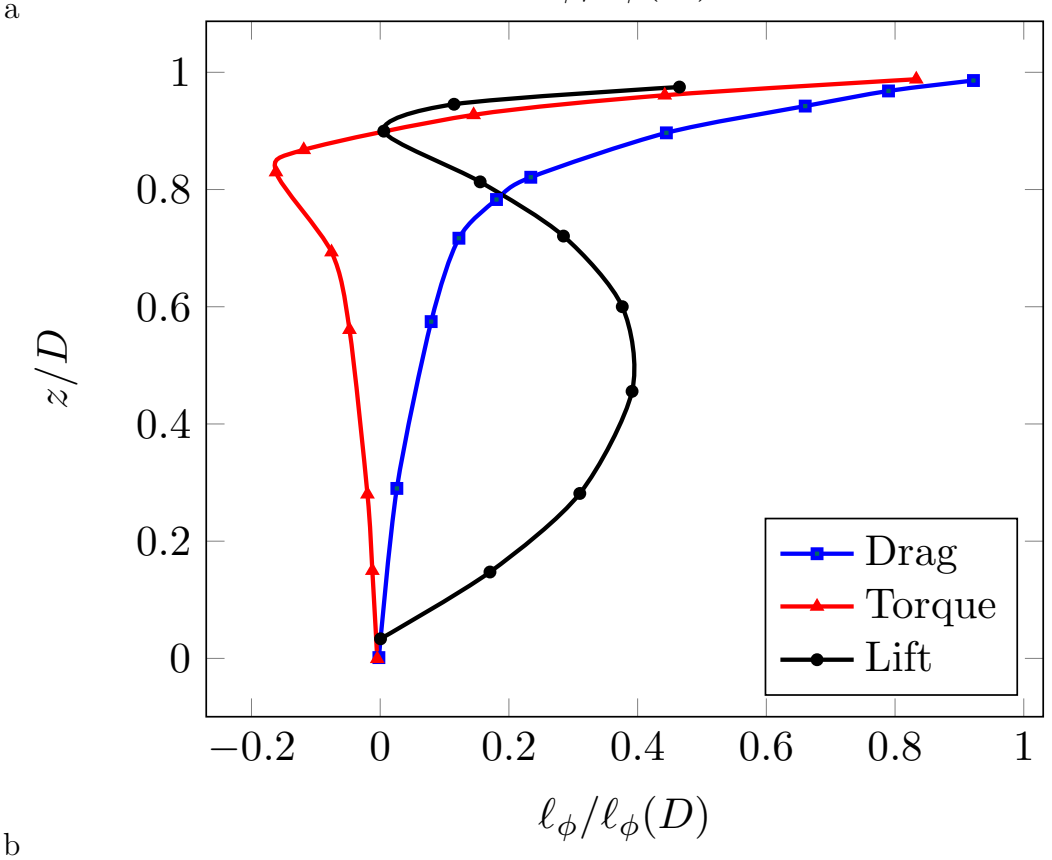
In contrast to the direct relation between the mean flow field and the mean forces on a particle, a similar straightforward relation between the statistics of the fluid velocity fluctuations and of the particle force fluctuations cannot be derived from equation 4.5. This is due to two factors. First, the definition of the standard deviation (and higher order moments) of the force fluctuations is non-linear. Second, the integrals in equation 4.5 act like a filter in the sense that not all scales participate in creating force fluctuations on a particle. For example, flow scales much smaller than $D$ might cancel out in the integral sense. Despite this observation, a direct relation between flow velocity statistics above the bed or behind an obstacle is often assumed in the literature to estimate the intensity of force fluctuations on a particle (Papanicolaou *et al.* (2002); Garcia (2008)).

In the present simulations, it is observed, that the standard deviations for the streamwise and spanwise components of the particle forces are of similar magnitude in both cases M1015 and P800. It is also found that the standard deviation of lift in both cases is roughly half the value of the other two components. Overall, the intensity of the fluctuations in case P800 is more than a factor of two larger than in case M1015. Thus, the particle force fluctuations in the present case do not seem to scale directly with the intensity of the plane- and time-averaged fluid velocity fluctuations, since $u_{rms}$ is larger than $w_{rms}$ over most of the flow depth, and especially close to the wall. Furthermore, the difference in the fluid velocity fluctuation intensities between case M1015 and P800 is very small compared to the above stated difference in the particle force fluctuation intensities. It can therefore be concluded that a direct link between fluid and particle force fluctuation intensities cannot be inferred in the present cases.

The results of skewness and kurtosis of the force distributions (table 4.2) are now discussed jointly with the probability density function (pdf) of the particle force fluctuations shown in figure 4.14. For both case M1015 and case P800 the highest skewness is obtained for lift, i.e.,




a




b

Figure 4.12: Cumulative function $\ell_\phi$ of the stress contribution to the mean value of drag, lift and spanwise torque on a particle as in case M1015(a) and case P800(b) a function of $z/D$ and normalised by its maximum value, $\ell_\phi(D)$

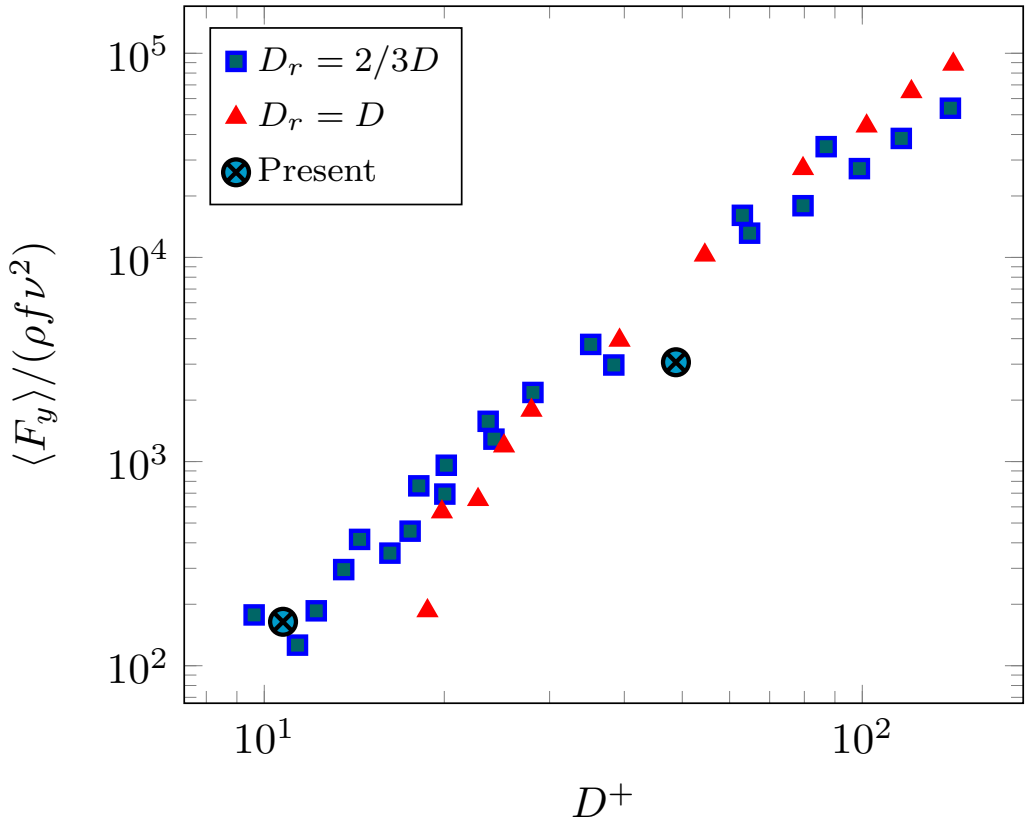



Figure 4.13: Comparison of $\langle F_y \rangle / (\rho f \nu^2)$ as a function of $D^+$ of case M1015 and case P800 with mean lift on a sphere placed between roughness elements in a boundary layer. Here $D_r$ is the diameter of rods spaced with $D_r$ upstream and downstream of a sphere with diameter $D$.

| Run | $C_{Tx}$ | $C_{Ty}$ | $C_{Tz}$ | $\sigma_{Tx}/T_R$ | $\sigma_{Ty}/T_R$ | $\sigma_{Tz}/T_R$ | $S_{Tx}$ | $S_{Ty}$ | $S_{Tz}$ | $K_{Tx}$ | $K_{Ty}$ | $K_{Tz}$ |
|---|---|---|---|---|---|---|---|---|---|---|---|---|
| M1015 | 0.00 | 0.00 | -0.98 | 0.21 | 0.04 | 0.36 | 0.01 | -0.01 | -1.04 | 6.46 | 6.17 | 4.72 |
| P800 | 0.00 | 0.00 | -0.73 | 0.17 | 0.11 | 0.27 | -0.01 | -0.01 | -0.76 | 3.75 | 4.91 | 3.37 |

Table 4.3: Statistics of torque on particles in case M1015 and P800. $C_{Ti} = \langle T_i \rangle / T_R$ is the normalised mean torque component in the $x_i$-direction, $\sigma_{Ti}$ is the standard deviation of the torque in $x_i$ direction, $S_{Ti}$ and $K_{Ti}$ are the skewness and kurtosis of the respective torque component.

$S_{Fy}$. In other words, large positive lift fluctuations are significantly more likely to occur than large negative lift fluctuations. This is clearly visible in figure 4.14(a), where lift events of several standard deviations higher than the mean have a non-negligible probability of occurrence. In case P800, this effect is not as strong as in case M1015 (cf. figure 4.14b, and accordingly the value of the skewness $S_{Fy}$ is lower in the former case. The small positive skewness of the drag indicates similarly that instantaneous high drag events are more likely compared to low drag events. For this component, however, the effect appears to be much weaker as compared to lift. Finally, symmetry arguments again lead to the conclusion that $S_{Fz}$ should be zero, and this is indeed the case.

The kurtosis of all profiles is rather large, indicating a strong intermittency of the forces, i.e. the pdfs in figure 4.14 exhibit much longer tails than a Gaussian distribution. However, as the spheres become larger the values of skewness and kurtosis approach the Gaussian values of zero and three. This trend might be since the force on the particle is an integral quantity, and as mentioned before, small intermittent events might be averaged out.

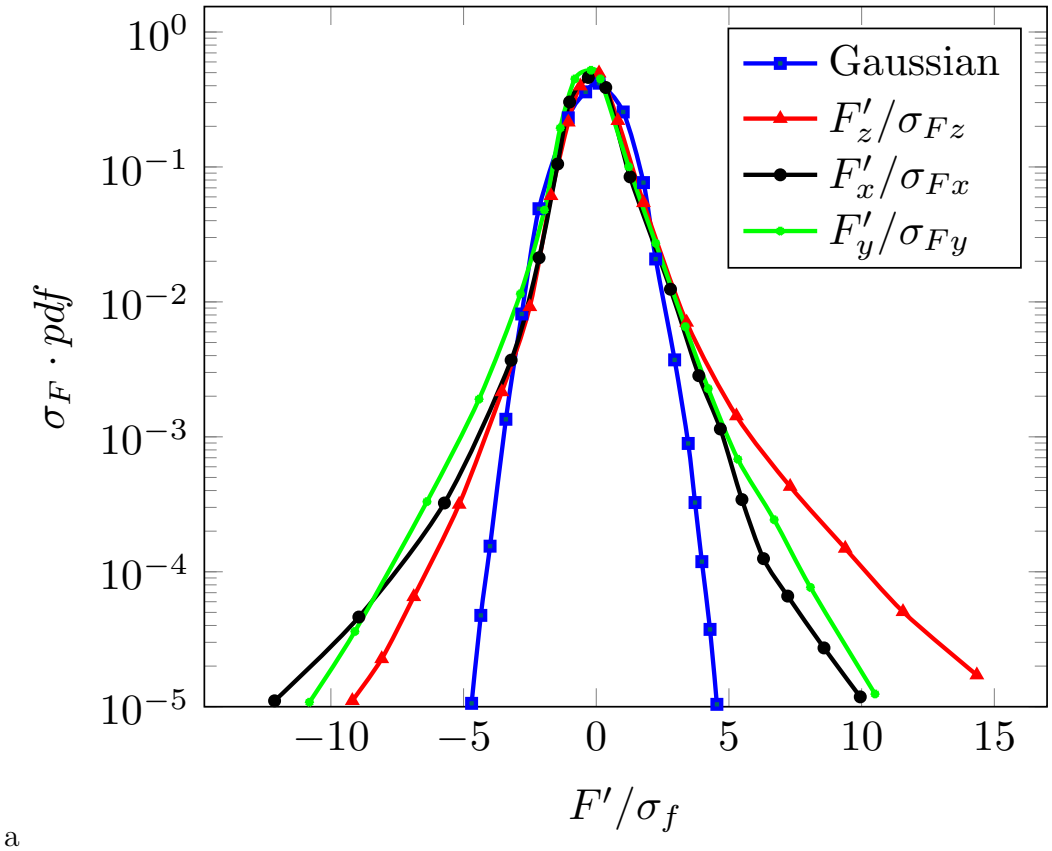
The results above might be compared to the experiments of Mollinger & Nieuwstadt (1996) on lift fluctuations on a single sphere with $D^+ = 2.9$ positioned on top of a smooth wall. Although their flow configuration is somewhat different (no sheltering effect, turbulent boundary layer) they also report positive values for the skewness ($S_{Fy} = 1.2$) and high values of flatness ($K_{Fy} = 7.0$). Furthermore, the pdf of the lift fluctuations in their study is of similar shape to the one obtained in the present case M1015. This qualitative agreement suggests that the present results might be relevant to a broader range of flow configurations, e.g., different sphere arrangements or packing densities.

## 4.4 Statistics of particle torque

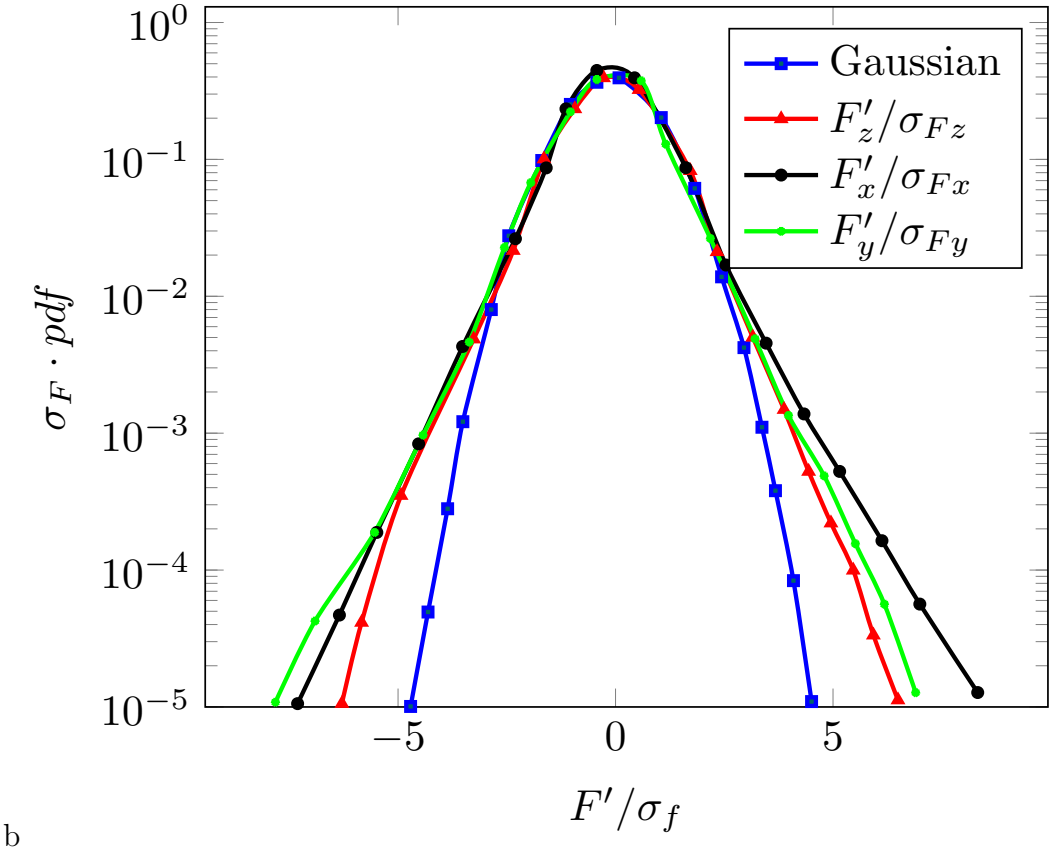
The hydrodynamic torque $\mathbf{T}$ on a spherical particle with respect to its centre is defined as

$$T = \int_\Gamma r_p \times (\tau \cdot n) d\Gamma \tag{4.10}$$

where $r_p = (r_x^p, r_y^p, r_z^p)$ is the distance vector from the particle centre to an element of the surface $\Gamma$. It should be noted that contrary to the definition of the hydrodynamic force on a particle (4.5) the pressure does not enter the integral (4.10, since in the present case the differential pressure force $p_{tot} n ds$ on a surface element $ds$, is always directed towards the particle centre.




a




b

Figure 4.14: Normalised probability density functions of force fluctuations in case M1015 (a) and case P800 (b).

Based on the reference force $F_R$, the reference torque is defined as $T_R = F_R r_R$ where $r_R$ is the distance from the particle centre to the virtual wall, $r_R = y_0 - D/2$. The quantity $T_R$ will be used in the following for the normalisation of the various torque related statistical values. A sketch that illustrates the definition of the torque on a particle can be seen in figure 4.11.

Table 4.3 shows the statistical moments of the torque on the particles. Here, $C_{Ti}$ is the mean torque in the $x_i$-direction normalised by $T_R$. Once more, due to symmetry the only non-zero component of the mean torque is expected to be $C_T^z$. The table shows that negative mean values for the spanwise component are obtained. These negative values of $C_T^z$ are expected for the torque on a particle in positive shear. The torque coefficient as defined above takes values close to $-1$ for case M1015, while it is approximately 25% lower in magnitude in case P800.

Before turning to the discussion of the torque fluctuations, first a simple model is introduced, which allows us to elucidate some of the characteristics of torque by considering flow structures related to the torque fluctuations on a particle. It should be noted that other authors have previously investigated the relation between flow structures at different scales and the forces/torque exerted upon sediment particles (Hofland *et al.* (2005)). Here we employ a somewhat different approach which allows us to use data from a smooth wall flow. We first analyse drag and torque fluctuations experienced by a square wall-element in channel flow with a geometrically smooth wall, systematically varying the linear dimension of the wall-element. Subsequently, the obtained statistical results are related to the corresponding statistics of the components of the torque on a spherical particle in the fixed sphere simulations. Analogously to the definition of force and torque on a particle the force in $x$ and $z$ direction on a square surface element in a smooth wall channel with area $A_s = s^2, F_x$ and $F_z$, can be defined as:

$$F_x \int_{-s/2}^{+s/2} \int_{-s/2}^{+s/2} \tau_{xy} \mid_{y=0} dxdz, \quad F_x \int_{-s/2}^{+s/2} \int_{-s/2}^{+s/2} \tau_{zy} \mid_{y=0} dxdz, \tag{4.11}$$

where $s$ is the side length of the element and $\tau_{ij} \mid_{y=0}$ are the components of the stress tensor at the wall. The torque on the element with respect to its centre, $F_y$, can be defined as:

$$F_y \int_{-s/2}^{s/2} \int_{-s/2}^{s/2} \left( r_x^s \tau_{zy} \mid_{y=0} - r_z^s \tau_{xy} \mid_{y=0} \right) dxdz, \tag{4.12}$$

where $r_s$ is the direction vector with respect to the centre of the area element.

Drag and spanwise force on the smooth wall element are expected to be mostly affected by velocity scales in streamwise and spanwise direction, respectively, that are of sizes similar or larger than s. The effect of velocity fluctuations at length scales much smaller than s will tend to cancel out, due to the integral quality of the force. Thus, the highest value of force fluctuation should be expected for smallest values of $s$, as the contribution of the smaller scales is lost for larger values of s. Conversely, due to the cross-product the torque on a smooth wall surface element is mostly affected by wall-normal vortical motions of sizes comparable to s. The effect of much smaller and much larger scales will cancel out or lead to only small values of torque. Thus, for small as well as high values of $s$ small values of $T_y$ are expected. At some intermediate value of $s$, the characteristics of wall-normal vortical motions should be most efficient in generating torque, leading to maximum values of $T_y$. Figure 4.15(a) supports that hypothesis. It shows the standard deviation of the forces and torque on the surface element, $\sigma_{fx}$, $\sigma_{fz}$ and $\sigma_{fy}$ normalised by $\rho_f u_\tau^2 s^2$ and $1/2\rho_f u_\tau^2 s^3$, respectively. On a square element with

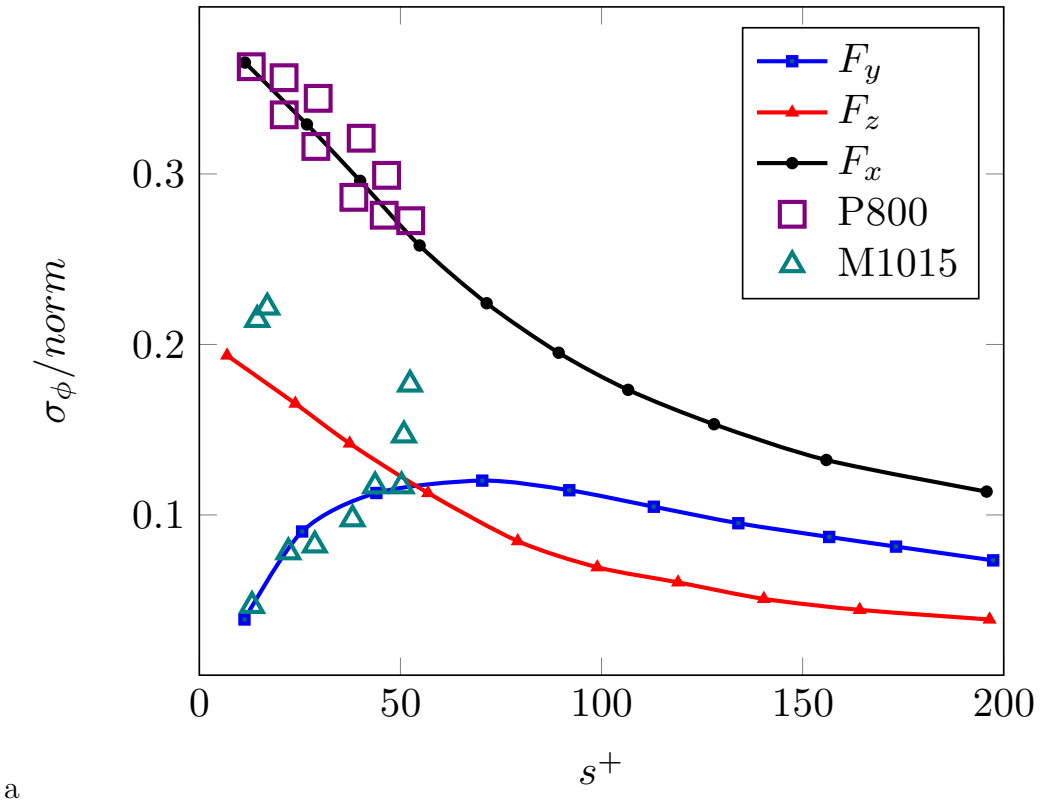
$s^+ \approx 70$ torque appears to be most efficiently produced. This value is somewhat larger than the average distance between the low speed and high speed streak close to the wall which is commonly found to be of order $50\nu/u_\tau$. As can be seen in figure **??**b, the kurtosis of the above quantities monotonically decreases with the size of the surface element indicating that the intermittency of the small scales is larger than that of the large scales.

A direct analogy between this smooth wall model and the force and torque on a particle is not fully justified, as the flow and the geometry are more complex in the present case. However, some of the characteristics of the particle torque statistics obtained for the present cases can be explained with the aid of such a simple model as will be discussed in the following. Please note that only one torque component can be defined for a plane wall element (here $T_y$), in addition to the two in-plane forces considered ($F_x$ and $F_z$). Some correspondence with the three torque components on a spherical particle is established when considering the plane wall element as being located at the top (i.e. the pole located at $y = D$) of the particles in case M1015 and P800. The component-wise correspondence is then: $F_x \rightarrow -T_z, F_y \rightarrow T_y, F_z \rightarrow T_x$.

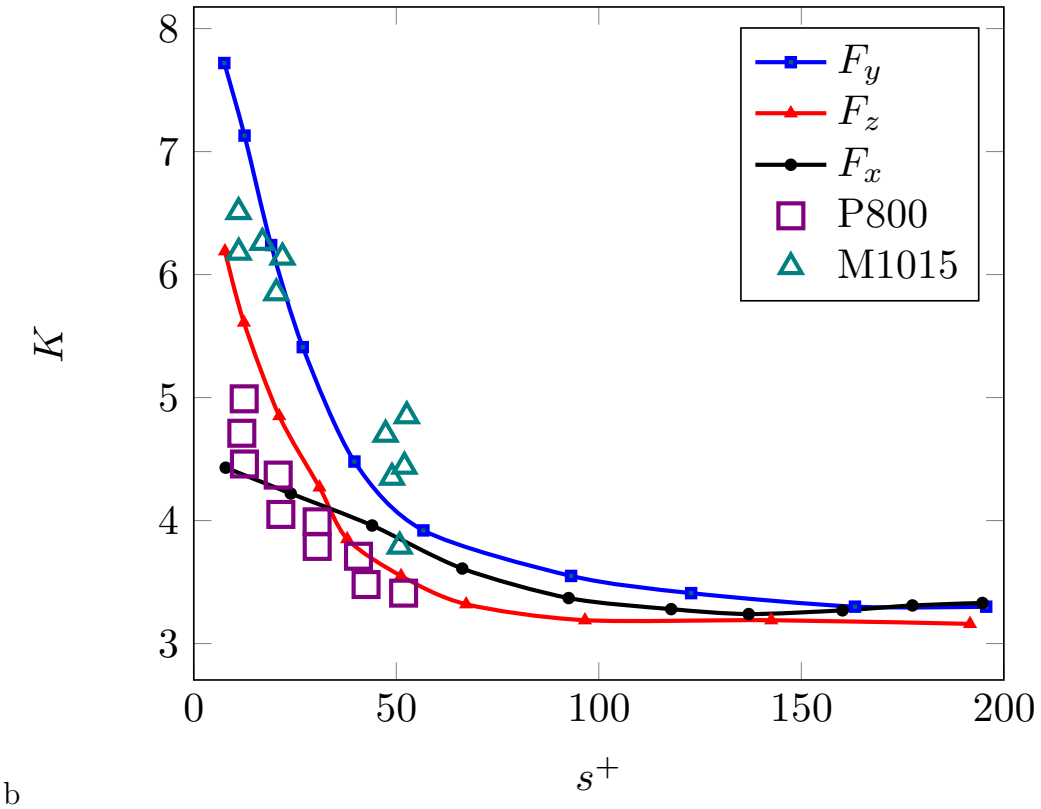
The normalised standard deviations of the particle torque components shown in table 4.3 are all non-zero as can be expected. The amplitudes of the fluctuations of the streamwise and spanwise torque components are found to be the largest, while the wall-normal component is significantly weaker. Compared to the small-sphere case (M1015), the streamwise and spanwise components are smaller in the large sphere case (P800), by 20% ($\sigma_{Tx}/T_R$ and 25% ($\sigma_{Tz}/T_R$), respectively. Contrarily, the wall-normal value $\sigma_{Ty} = T_R$ is significantly larger in case P800 than in case M1015 (nearly by a factor of three).

Figure 4.15, which has already been partially discussed above, also shows the second and fourth statistical moments of particle torque fluctuations as a function of particle size. As can be seen, the standard deviation (figure 4.15a) of the wall-normal torque on the particles, $T_y$, matches rather well the standard deviation of the wall-normal torque exerted on a comparable-size square element in the reference smooth wall flow, $T_y$. In addition, the figure shows that the standard deviation of the spanwise torque, $T_z$, compares very well to the standard deviation of the drag exerted on a square element in the smooth wall case, $F_x$. Concerning the streamwise component of particle torque, $T_x$, it is found that its standard deviation is somewhat larger than the standard deviation of the spanwise force fluctuations in the smooth wall model, $F_z$; however, both exhibit a similar decreasing trend with increasing values of the length scale. The overall good agreement between fluctuation intensity of forces/torque on an element of a smooth wall and the corresponding torque components of the particle in case M1015 and case P800 is interesting for several reasons. First, it suggests that the significant torque fluctuations are generated in a rather limited region around the particle tops where apparently to some extent the analogy with the hydrodynamic action on a wall-parallel square element holds. The present simulations M1015 and P800 provide two data points in the hydraulically smooth and transitionally rough flow regime, which are fully consistent with the existence of a length scale/particle size of maximum wall-normal torque generation, as suggested by the simplified model. Secondly, if the above analogy is accepted, then it implies that the response of the particle torque fluctuations to the near-wall turbulent flow can indeed be described as a selective filtering effect, mainly characterised by a single length scale (the particle diameter).

Normalised pdfs of the particle torque fluctuations are shown in figure 4.16(a,b) and 4.17(c,d) The curves for all three torque components in both cases M1015 and P800 approximately match the curves of the corresponding force and torque components of the smooth wall model (evaluated with a side-length matching the respective length $\sqrt{A_R}$), thereby further corroborating




a




b

Figure 4.15: Root-mean-square value (a) and kurtosis (b) of force and torque obtained from the simple model described in the text and of actual values of the corresponding torque obtained on the particles in case M1015 and P800.

the analogy. Concerning the shape of the particle torque pdfs themselves, it is observed that the two symmetric components (streamwise $T_x$ and wall-normal $T_y$) have significantly longer tails than a Gaussian function, and consequently exhibit higher than Gaussian values of kurtosis. The kurtosis is found to decrease with increasing particle size, consistent with the above filtering argument.

The pdf of the fluctuations of the spanwise component of particle torque, $T_z$, is clearly asymmetric with a pronounced negative skewness. Now, it is well established that the pdf of streamwise velocity fluctuations $u^{'}$ in smooth wall channel flow is positively skewed close to the wall (Kim *et al.* (1987); Hoyas & Jiménez (2006)). In the limit of a wall-element with vanishing size, the pdf of $F_x$ is directly related to the pdf of the streamwise velocity fluctuations just above the wall. Since, as found above, the particle torque component $T_z$ behaves similarly as the smooth wall force $F_x$ (note the changed sign), the observed negative skewness of the former is consistent with the positively skewed streamwise velocity pdf previously found in smooth wall channel flow.

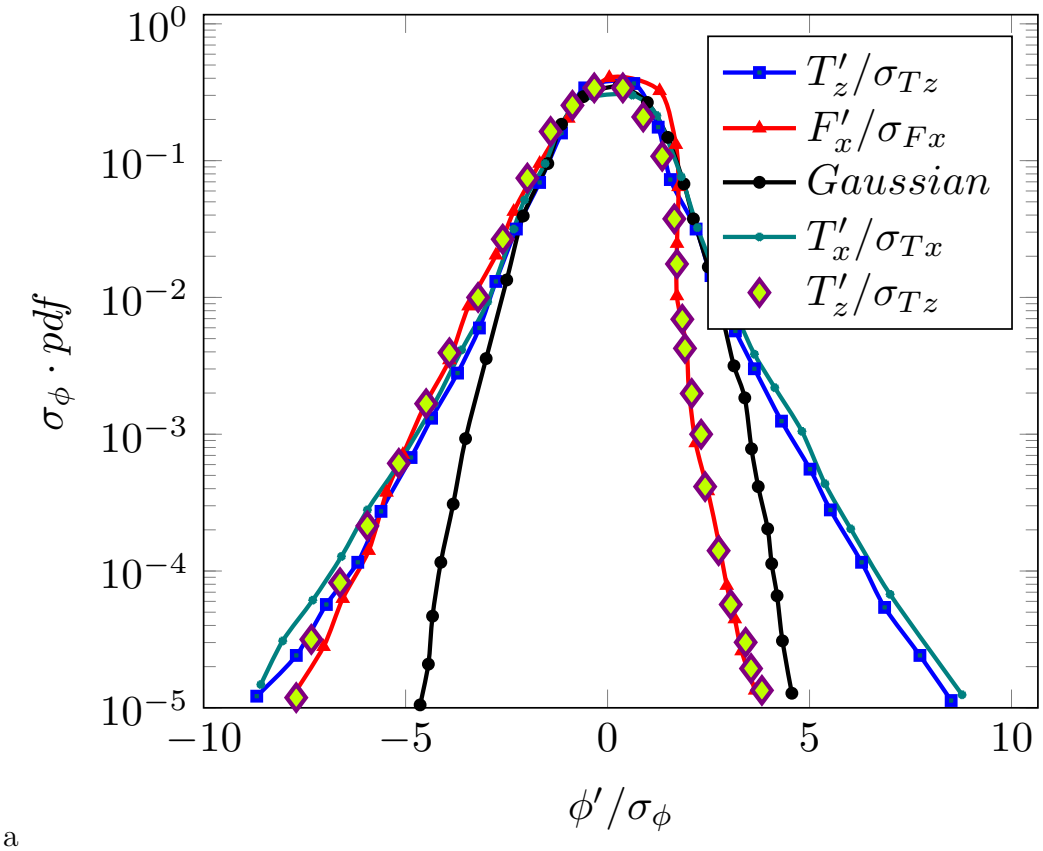
It should be noted that the analogy drawn between shear forces on a square element of a smooth wall channel flow and the corresponding hydrodynamic torque components of spherical particles in the roughness layer can be expected to lose its appeal in the fully rough regime. In that case, which is outside the scope of the present study, pressure induced forces might by far outweigh viscous forces. Therefore, the main utility of the proposed simple model is presumably limited to the regime of transitional roughness.

## 4.5 Time scales of torque fluctuations on a particle

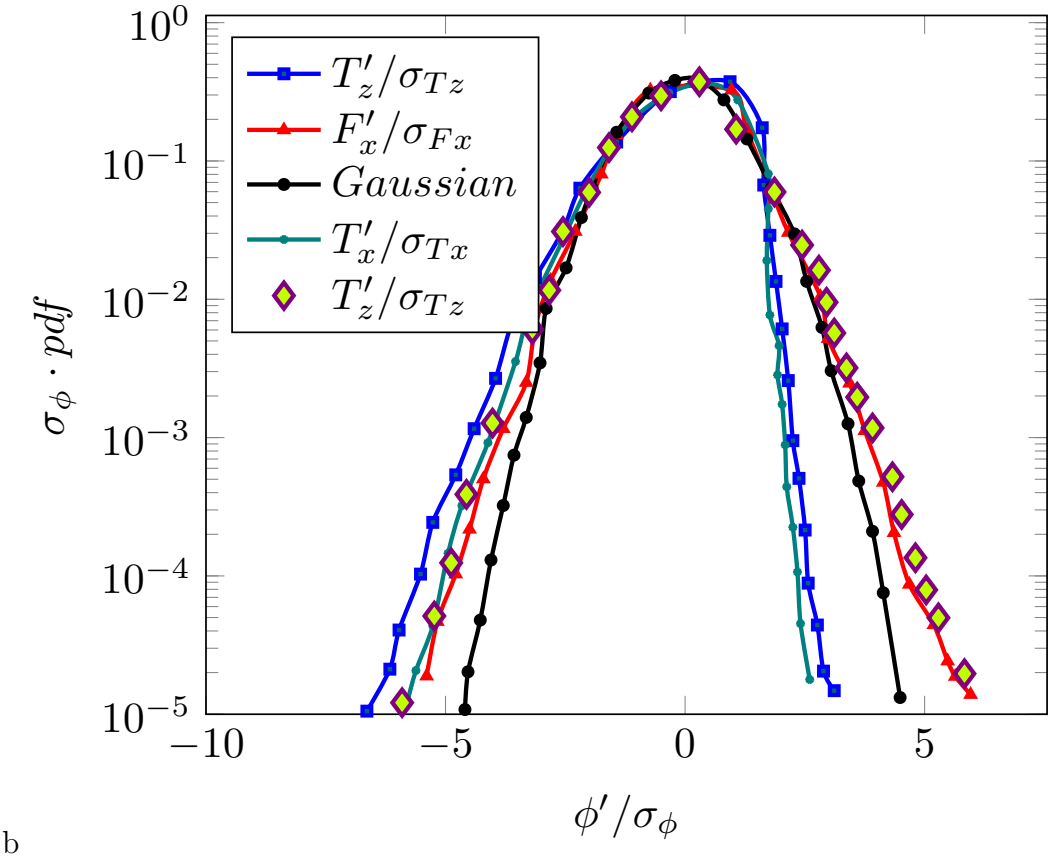
In the following, the auto-correlation, $R_{\phi\phi}(\tau)/\sigma_\phi^2$, of particle torque fluctuation in case M1015 and case P800 as defined by (4.13) are discussed. The auto-correlations are computed from the particle data collected during run-time of the simulations. The results are compared to those of the autocorrelation of force and torque on a square smooth wall surface element of side length $s^+ = 12$, i.e., the components of torque on a particle are compared to smooth wall results as follows: $F_x \rightarrow -T_z, F_y \rightarrow Ty, Fz \rightarrow Tx$. Figure 4.18(a,b,c) shows the auto-correlation of $T_x'$, $T_y'$ and $T_z'$ jointly with the auto-correlation of $F_z'$, $T_y'$ and $F_x'$ for $s^+ = 12$ respectively. The time lag, $\tau$ , is normalised by $\nu/u_\tau^2$ or which good agreement between the curves is obtained. In particular the curves of $T_x'$ and $T_z'$ of case M1015 in panel (a) and (c) overlap with the smooth wall results $F_z'$, and $F_x'$, respectively. Although the differences are somewhat larger in figure 4.18(b), they can be considered small. The correlations of case P800 exceed the values of case M1015 in figure 4.18(a,b) which agrees to the behaviour of the respective components in the smooth wall case when increasing $s^+$ from 12 to 52.

$$R_\phi\Psi(\tau) = \frac{1}{t_1 - t_0}\int_{t_0}^{t_1} \phi(t+\tau)\Psi(t)dt, \tag{4.13}$$

(where $f(t)$ and $y(t)$ are two scalar quantities as a function of time, $t$, such as components of force or torque on a particle or on a smooth wall surface element, is the time lag and $t_0$ and $t_1$ define a time interval. To increase the quality of the correlation defined by (4.13) sample averaging is carried out over the number of considered particles, $N_p$, or over the number of considered smooth wall surface elements).

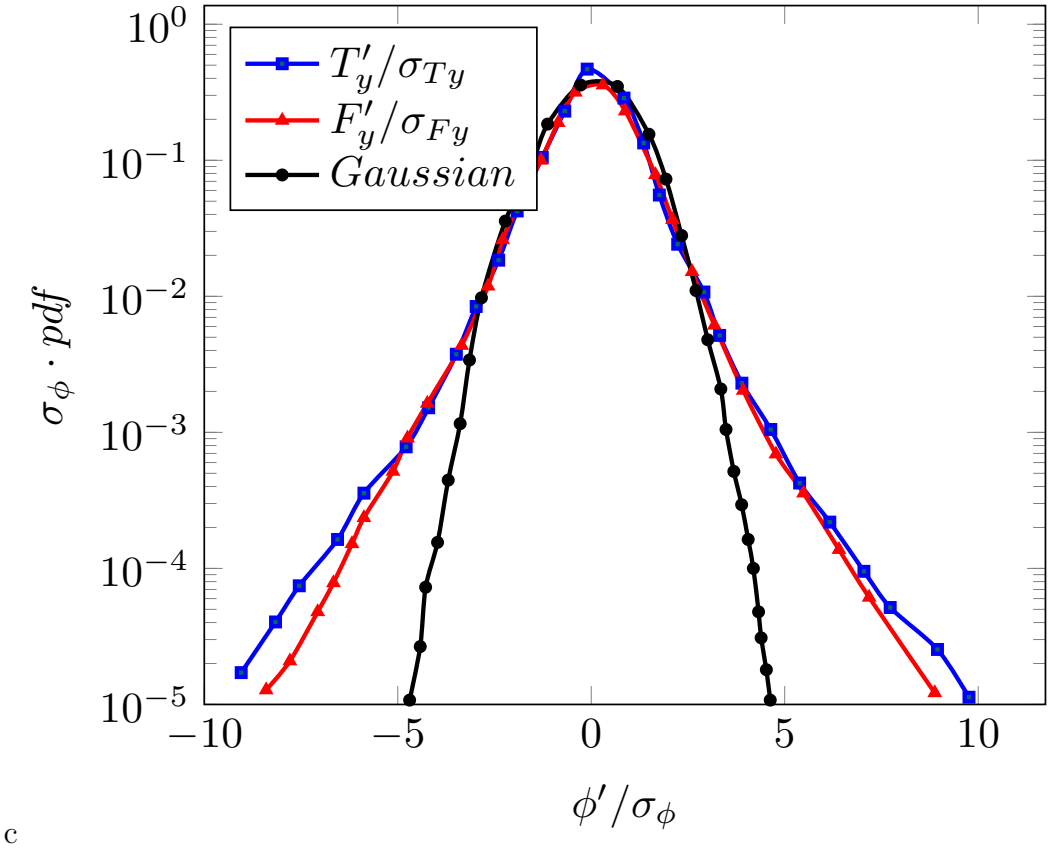



a

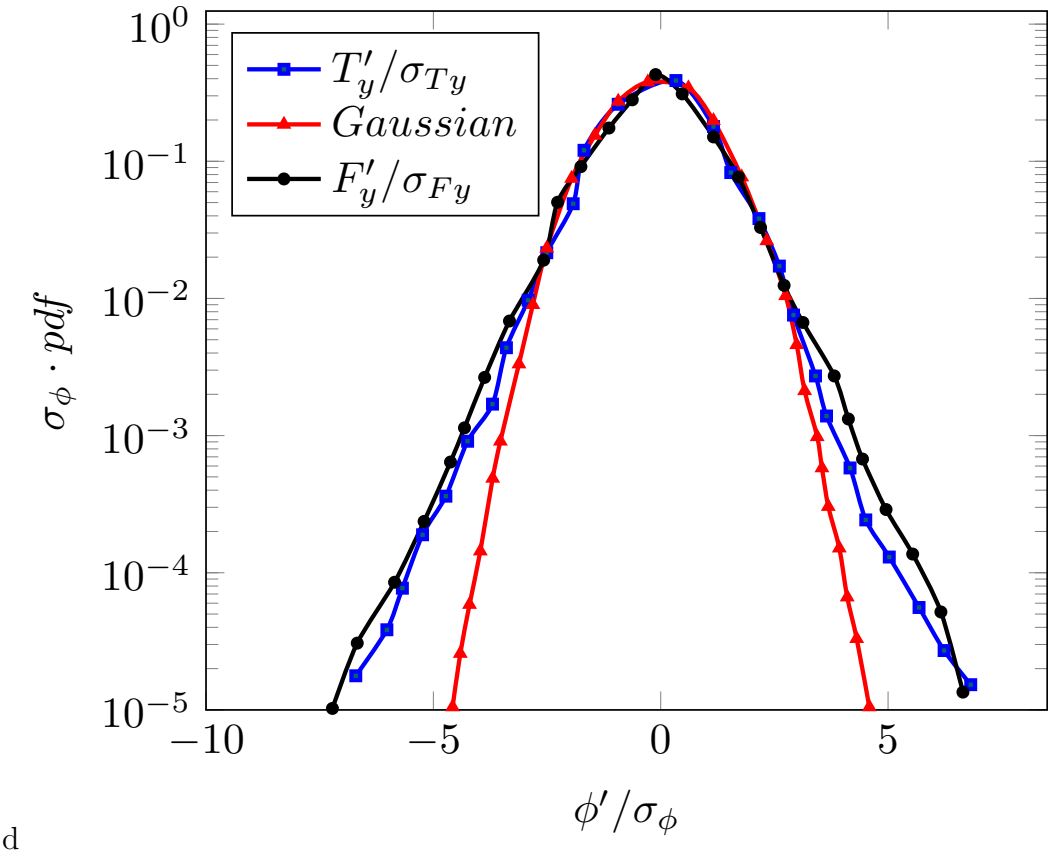



b

Figure 4.16: Normalised pdfs of the quantities for which statistical moments have been shown in figure 4.15.(a,c) Case M1015 compared to simple model with $s^+ = 12$. (b,d) Case P800 compared to simple model with $s^+ = 52$.




c




d

Figure 4.17: Normalised pdfs of the quantities for which statistical moments have been shown in figure 4.15.(a,c) Case M1015 compared to simple model with $s^+ = 12$. (b,d) Case P800 compared to simple model with $s^+ = 52$.

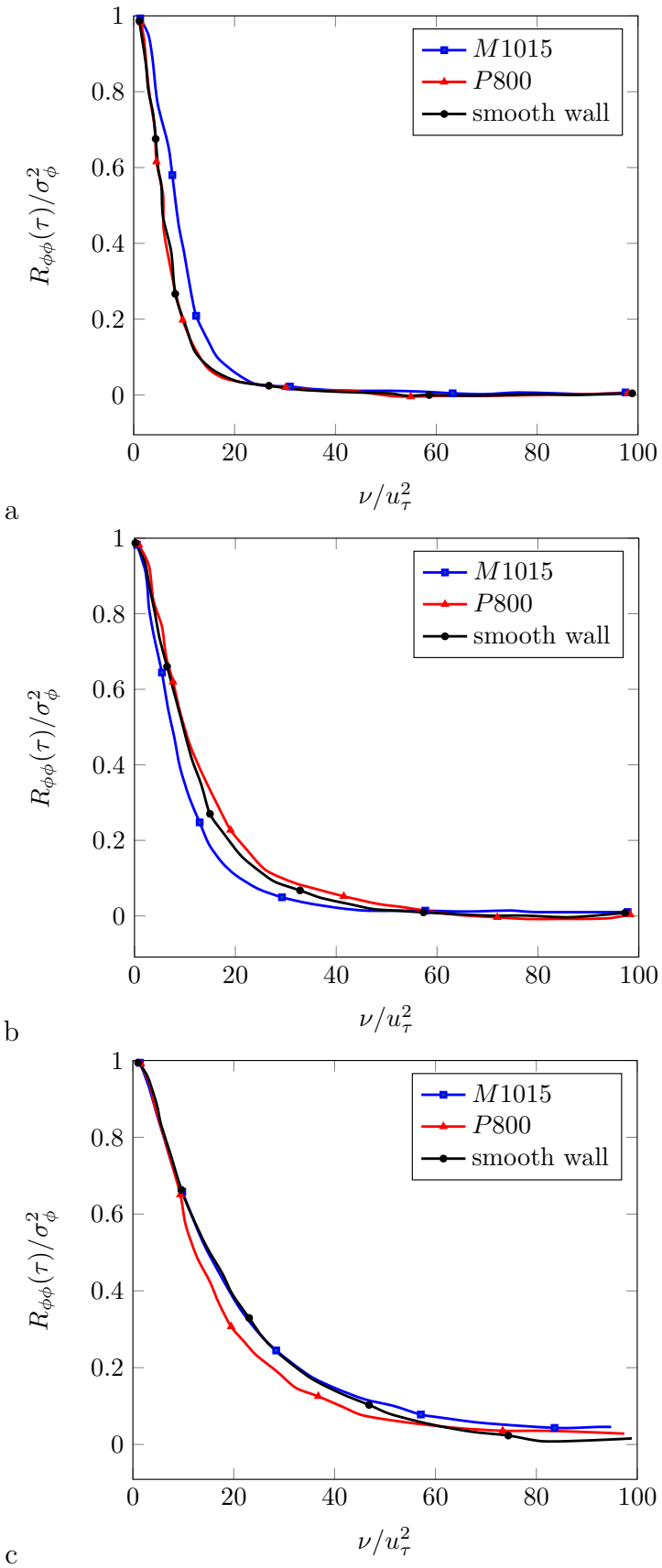



Figure 4.18: Auto-correlation of, $R_{\phi\phi}(\tau)/\sigma_\phi^2$, of particle torque fluctuation as a function of time lag, $\nu/u_\tau^2$. The panels show the results of (a) streamwise torque fluctuation, $T_y'$, (b) wall-normal torque fluctuation, $T_z'$, and (c) spanwise torque fluctuation, $T_x'$. The smooth wall case reference is from Clemens *et al.* (2011).

| Run | $F'_{xm}$ | $F'_{ym}$ | $F'_{zm}$ | $F'_{x\ell}$ | $F'_{y\ell}$ | $F'_{z\ell}$ | $F'_{xmin}$ | $F'_{ymin}$ | $F'_{zmin}$ |
|---|---|---|---|---|---|---|---|---|---|
| M1015 | 0.24 | 0.25 | 0.32 | 0.24 | 0.30 | 0.29 | 0.45 | 1.10 | 0.89 |
| P800 | 0.24 | 0.24 | 0.36 | 0.15 | 0.17 | 0.29 | 0.54 | 0.57 | 0.87 |

Table 4.4: Time scales of force fluctuations on a particle in case M1015 and P800 normalised by $h/U_{bh}$. Considered time scales are the micro time scale, $m$, the integral time scale, $\ell$, and the time-lag related to the first local minimum $min$.

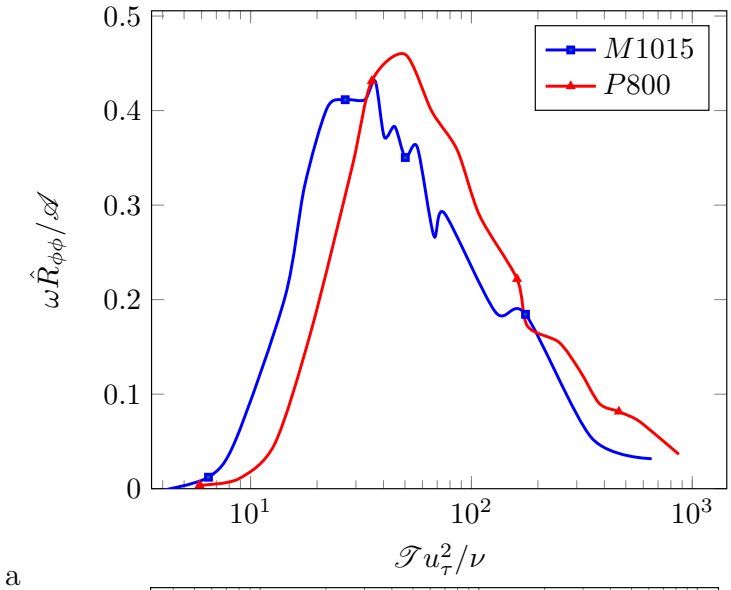
Here however, in the case of autocorrelation of torque on a particle the effect seems to be less strong. The auto-correlation functions of $F_z$ in figure 4.18(c) do not follow this trend, i.e. the correlation is smaller in case P800 than it is in case M1015. This is even more pronounced when scaled in outer units (plot omitted). Table 4.4 provides the time scales, $\tau_m$, $\tau_\ell$ and $\tau_{min}$ of the profiles in figure 4.18. Similar to the force fluctuations, m increases for all torque fluctuations from case M1015 to P800 when scaled in viscous units. As can be seen the values of $\tau\ell u_2^\tau/\nu$ of $T'_x$ and $T'_y$ increase from case M1015 to P800, while the value for $T'_z$ decreases.

Some more insight can be gained from the pre-multiplied spectra of the torque fluctuations shown in figure 4.19. The spectra are computed and normalised similar to figure 4.18, but here $\nu/u_2^\tau$ is used as reference time scale. In agreement with the filter argument the value $\omega\hat{R}_{\phi\phi}/\mathscr{A}$ of $T'_x$ and $T'_y$ decreases from case M1015 to case P800 for small $u_2^\tau/\nu$ and the contribution of time scales to the root-mean-square of particle torque fluctuations shifts to larger values. For large $u_2^\tau/\nu$ the spectrum of case P800 is found to be higher or equal than the spectrum of case M1015, which agrees to the trend observed in the smooth wall case. For the $T'_z$ the spectra appear to be of similar shape. A distinct difference is that the spectra of case M1015 is less smooth and exhibits a pronounced maxima at a period, $u_2^\tau/\nu = 175$. This value is close to twice as large as that in case P800 ($u_2^\tau/\nu = 99$),

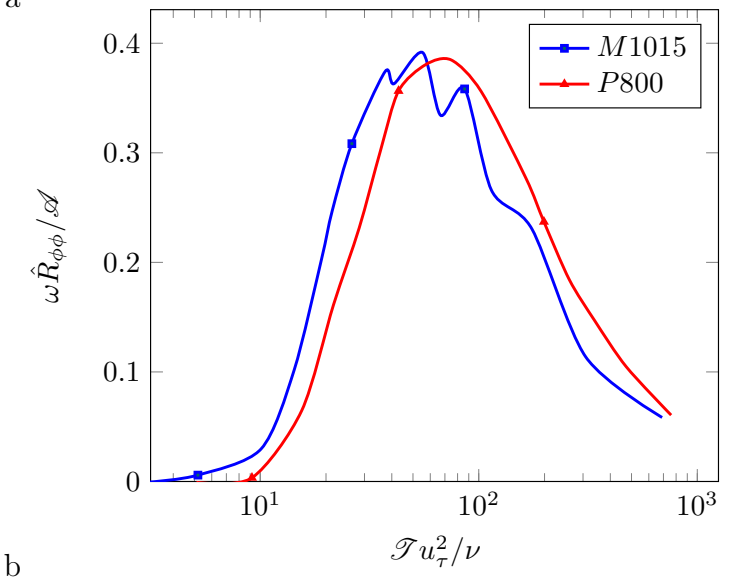
and might be a bias by the restriction of the domain size in streamwise direction. Also, when scaled in outer units $\mathscr{T}_{max}U_{bh}/h = 14$, and thus is comparable to the period related to the effect of the domain size limitation in the smooth wall case. The periods related to the maxima in figure 4.19, $\mathscr{T}_{max}$, are provided in table 3.8, in outer and inner units. It should be pointed out, that these maxima represent a broad range of periods. The values show the trend which was already discussed, i.e. while a shift to somewhat higher values of $\mathscr{T}_{max}u_\tau^2/nu$ can be observed for $T'_x$ and $T'_y$ from case M1015 to P800 (cf. figure 4.19), the value of $\mathscr{T}_{max}u_\tau^2/nu$ decreases from case M1015 to P800 for $T'_z$ . Additionally, the table shows that when scaled in outer flow units $\mathscr{T}_{max}$ decreases for all components of torque fluctuations.

## 4.6 Time scales of force fluctuations on a particle

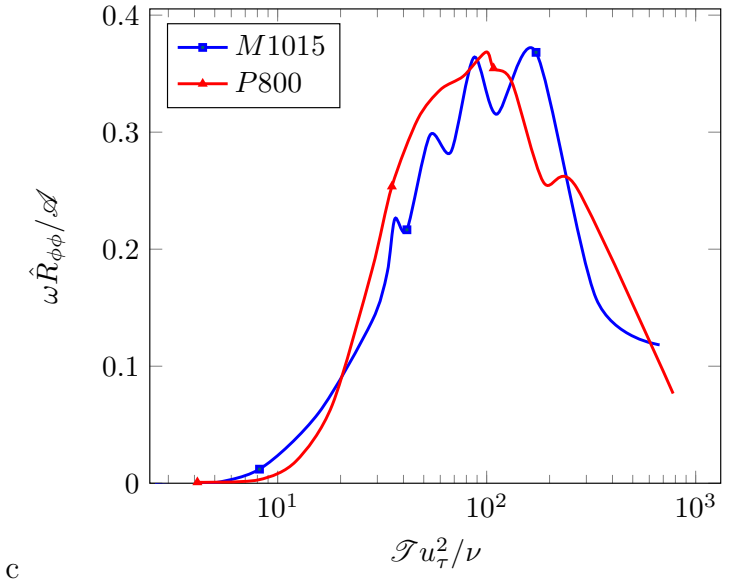
The auto-correlation, $R_{\phi\phi}(\tau)/\sigma_\phi^2$, of particle force fluctuation in case M1015 and case P800 as defined by (4.13) are provided in figures 4.20. As in the case of torque on particles, the auto-correlations are computed from the particle data collected during run-time of the simulations. For comparison, the autocorrelation of drag fluctuation, $F'_x$, and spanwise force fluctuation, $F'_z$, on a smooth wall surface element with $s^+ = 12$ are included in panels (a) and (c). In contrast to the autocorrelation of torque on particles, it is found that the characteristics of the autocor-




a




b




c

Figure 4.19: Pre-multiplied spectra $\omega\hat{R}_{\phi\phi}$ of particle torque fluctuations as a function of period $\mathscr{T}u_\tau^2/\nu$. Spectra are normalised by $\mathscr{A}$ as defined in the text.

relations of force differ between smooth wall case, case M1015 and case P800 (figure 4.20). The profiles of $F'_x$ and $F'_z$ are positive and decrease monotonically in the given range of figure 4.20, while in case P800 the profiles of $F'_x$, F$F'_y$ and $F'_z$ exhibit pronounced local minima of negative value. The profiles of $F'_x$, $F'_y$ and $F'_z$ in case M1015 exhibit local minima, however they are not as pronounced as in case P800. In particular, for the range of $\tau U_{bh}/h$ shown in figure 4.20, the correlations of $F'_x$ and $F'_y$ remain positive. For $F'_z$ the correlations become negative, however the magnitude is close to zero.

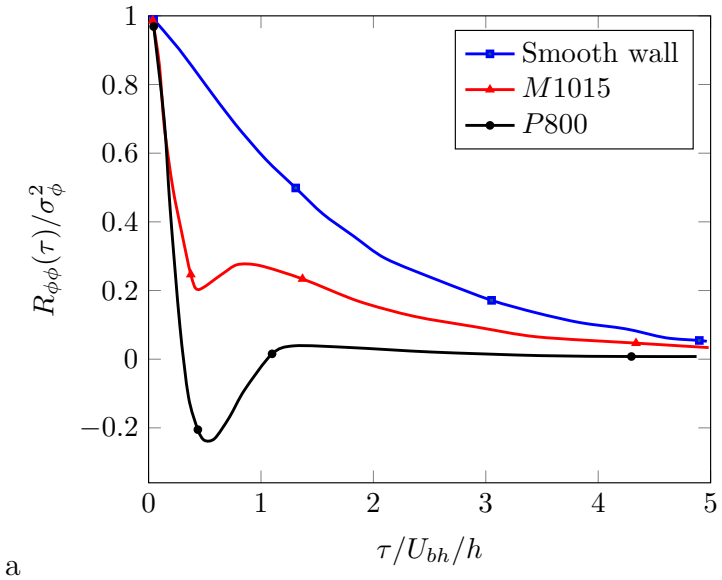
Table 4.4 provides the values of $\tau_m$, $\tau_\ell$ and $\tau_{min}$ for the auto-correlations in figure 4.20. The micro time scales, $\tau_m U_{bh}/h$, are found to be of similar value in both cases for drag and lift fluctuations. In case M1015 (P800) the value of $\tau_m U_{bh}/h$ of $F'_z$ is 33% (50%) larger than the respective value of $F'_x$. These trends differ from the smooth wall results, where $\tau_m U_{bh}/h$ of the force fluctuations increases with increasing $s^+$. Furthermore, $\tau_m U_{bh}/h$ of $F'_x$ was found to be larger than $\tau_m U_{bh}/h$ of $F'_z$. The differences could be related to the different shape of the autocorrelation, which appears to be strongly dominated by the occurrence of a local minimum for the force on a particle. The latter might be linked to the effect of pressure on the force on a particle. Recall, that the autocorrelation of pressure on a smooth wall in a turbulent channel flow is known to have pronounced minima of negative value similar to those in case P800 (see Kim, 1989 for autocorrelation in space, Quadrio & Luchini (2003) for auto-correlation in time). However, it is remarkable that the effect of pressure on the force on a particle in case M1015 should be that pronounced, as here the hydraulically smooth regime is approached for which it is generally assumed that viscous forces on the wall dominate the force behaviour.

It should be noted that, in contrast to the scaling by $h/U_{bh}$, $\tau_m$ increases for all fluctuation components from case M1015 to case P800 when scaled by viscous units, i.e. by $\nu/\tau_\tau^2$ (table omitted). Table 4.4 provides the time lag min, related to the local minimum in the autocorrelation of figure 4.20. In case M1015, the smallest value of $\tau_{min} U_{bh}/h$ is obtained for $F'_x$, the value increases by a factor of 2.4 (1.9) for $F'_y$ ($F'_z$). The strong increase related to lift fluctuations might be heavily biased by a not well pronounced minimum. In case P800, similar values of $\tau_{min} U_{bh}/h$ are obtained for drag and lift fluctuation which increase by 61% for $F'_z$ with respect to $F'_x$. In both cases the values of $\tau_{min} U_{bh}/h$ for $F'_x$ and $F'_z$ are similar, in particular, in case M1015 the values are respectively 17% smaller and 2% larger as in case P800. It is interesting to note, that for the present cases $\tau_{min} U_{bh}/h$ is 1.9 to 2.8 times larger than the value of $\tau_m U_{bh}/h$.

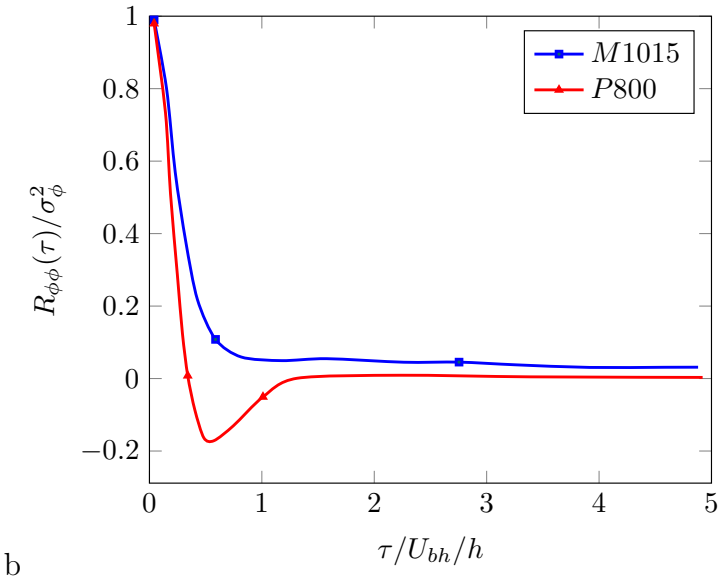
The integral time scale, $\tau_\ell U_{bh}/h$, is comparable to the micro time scale $\tau_m U_{bh}/h$ for all force fluctuation components (table 4.4), which indicates that the integral time scale as defined by (4.13 fails to provide a measure of large time scales in the present cases. A more appropriate definition based on the autocorrelations is difficult to define, as the characteristics of profiles in figure 4.20 vary among the cases.

The influence of the streamwise periodicity on the autocorrelations of particle force fluctuations appears to be weak in figure 4.20. Only in figure 4.20(a) some large scale fluctuations are noticeable in case M1015. However, the amplitude is small and is damped out faster than in the smooth wall case. A possible explanation for the weaker influence might be the contribution of pressure on the force fluctuations. Recall, that pressure is commonly found to have a smaller correlation length than the shear stress at the wall (Kim (1989); Choi & Moin (1990); Quadrio & Luchini (2003)). Thus, its influence might lead to a shortening of the correlation in time.

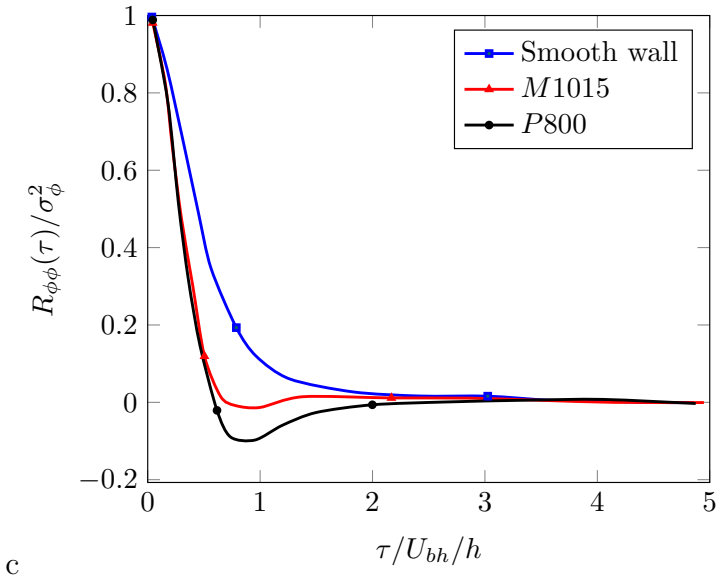
Figure 4.21 shows pre-multiplied spectra of the force fluctuations computed and normalised. Here, the comparison to the respective smooth wall forces is omitted. The figure reveals that most of the energy in the force fluctuation on a particle is contributed to time scales with periods




a




b




c

Figure 4.20: Auto-correlation, $R_{\phi\phi}(\tau)/\sigma_\phi^2$, of particle force fluctuation as a function of time lag, $\tau U_{bh}/h$. The panels show results of (a) drag fluctuation, $F_y'$, (b) lift fluctuation, $F_z'$, and (c) spanwise force fluctuations, $F_x'$.

| $\mathscr{T}_{max}U_{bh}/h$ | $F'_x$ | $F'_y$ | $F'_z$ |
|---|---|---|---|
| M1015 | 1.0 | 1.3 | 1.6 |
| P800 | 1.2 | 1.2 | 1.8 |

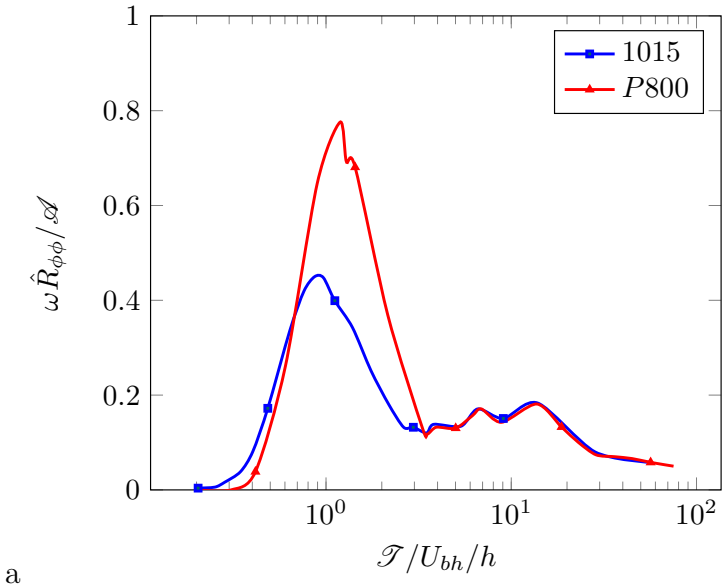
Table 4.5: Period of local maximum in pre-multiplied spectra of force fluctuations, $\mathscr{T}_{max}$, normalised by outer flow time scale, $U_{bh/h}$.

of order $h/U_{bh}$. In particular the curves of $\omega\hat{R}_{\phi\phi}/\mathscr{A}$ exhibit maxima with a period in the range of $\mathscr{T}U_{bh}/h = 1$ to 2 in both cases and for all three force components. The values of $\omega\hat{R}_{\phi\phi}/\mathscr{A}$ in case M1015 exceed the values of case P800 for small and large $\mathscr{T}U_{bh}/h$. In particular for $F'_x$ an increased contribution of time scales with a large period can be observed. This might be linked to an increased bias of the domain size in streamwise direction in this case M1015. The larger values of $\omega\hat{R}_{\phi\phi}/\mathscr{A}$ for small and large periods in case M1015 are compensated by more distinct maxima in case P800. Interestingly, the maxima are most pronounced for $F'_x$ and $F'_y$ with values being nearly twice as large in case P800 than in M1015. In contrast, the differences in the spectra of $F'_z$ are smaller and can be found in particular for smaller periods.

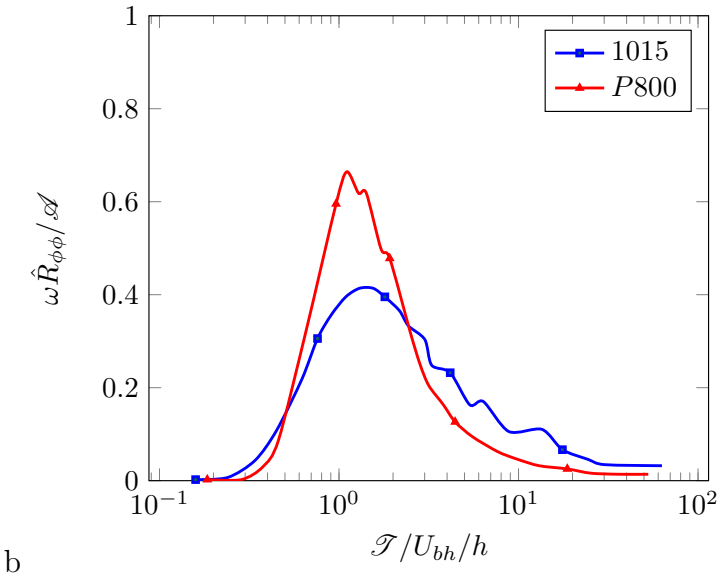
The decrease of $\omega\hat{R}_{\phi\phi}/\mathscr{A}$ with the particle size $D^+$ for small $\mathscr{T}U_{bh}/h$ is in agreement with the filtering argument utilised in the discussion of the autocorrelation of particle torque above. The decrease of $\omega\hat{R}_{\phi\phi}/\mathscr{A}$ with the particle size $D^+$ for large $\mathscr{T}U_{bh}/h$ is more difficult to explain and might be a result of multiple factors. It might be related to the damping of large-scale flow structures in the near wall region by roughness. Also, it could indicate an increased effect of pressure in case P800 which might lead to an amplification of smaller scales and reduce the relative influence of large scales structures.

The periods related to the maxima of the pre-multiplied spectra in figure 4.21, $\mathscr{T}_{max}U_{bh}/h$, are given in table 4.5. Keep in mind, that $\mathscr{T}_max$ represents a range of scales rather than a single pronounced peak (figure 4.21). The table reveals that the value of $\mathscr{T}_{max}U_{bh}/h$ for drag fluctuations is 1.0 in case M1015 and shifts to the somewhat higher value of 1.2 in case P800. The maximum in the premultiplied spectra of lift fluctuations is positioned at a period of $\mathscr{T}_{max}U_{bh}/h = 1.3$ (1.2) in case M1015 (P800) which is 30% (0%) higher than for drag. The value $\mathscr{T}_{max}U_{bh}/h$ of the spanwise force fluctuation is 60% (50%) larger than for drag fluctuation in case M1015 (P800). Comparing the values of $\mathscr{T}_{max}U_{bh}/h$ in table 3.10 with $\tau min U_{bh}/h$ in table 3.9 shows that $\mathscr{T}_{max} \approx 2\tau_{min}$ for most quantities.

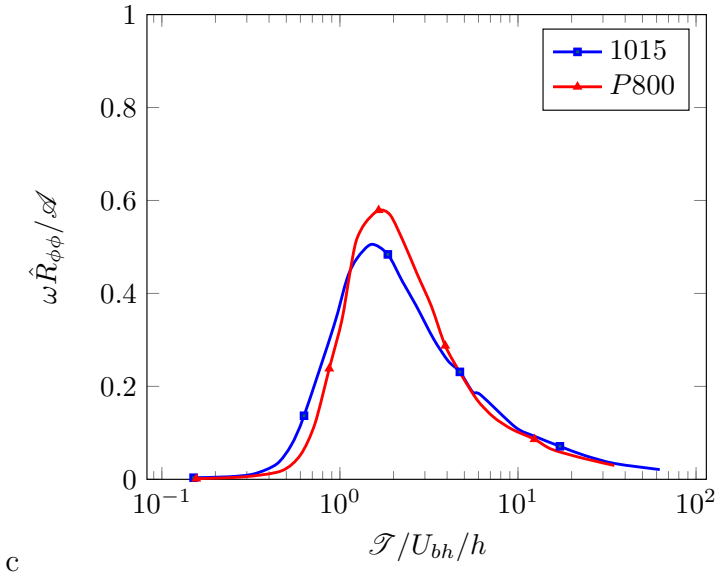
Here, the most dominant scales $\mathscr{T}U_{bh}/h$ are found in the range of 0.4 to 4. This agrees with the study of Hofland *et al.* (2005). The authors estimated drag and lift by the difference of two pressure measurements on a cube with dimensions of about $3300\delta_\nu$ at $Re_b$ of about $1.3 \cdot 10^5$. The ratio of open channel depth to cube height was about six, which is similar to the ratio of $h = D$ in case P800. They found that the highest values in the premultiplied spectra of estimated drag and lift for periods in the range of $\mathscr{T}U_{bh}/h = 0.6$ to 6.




a

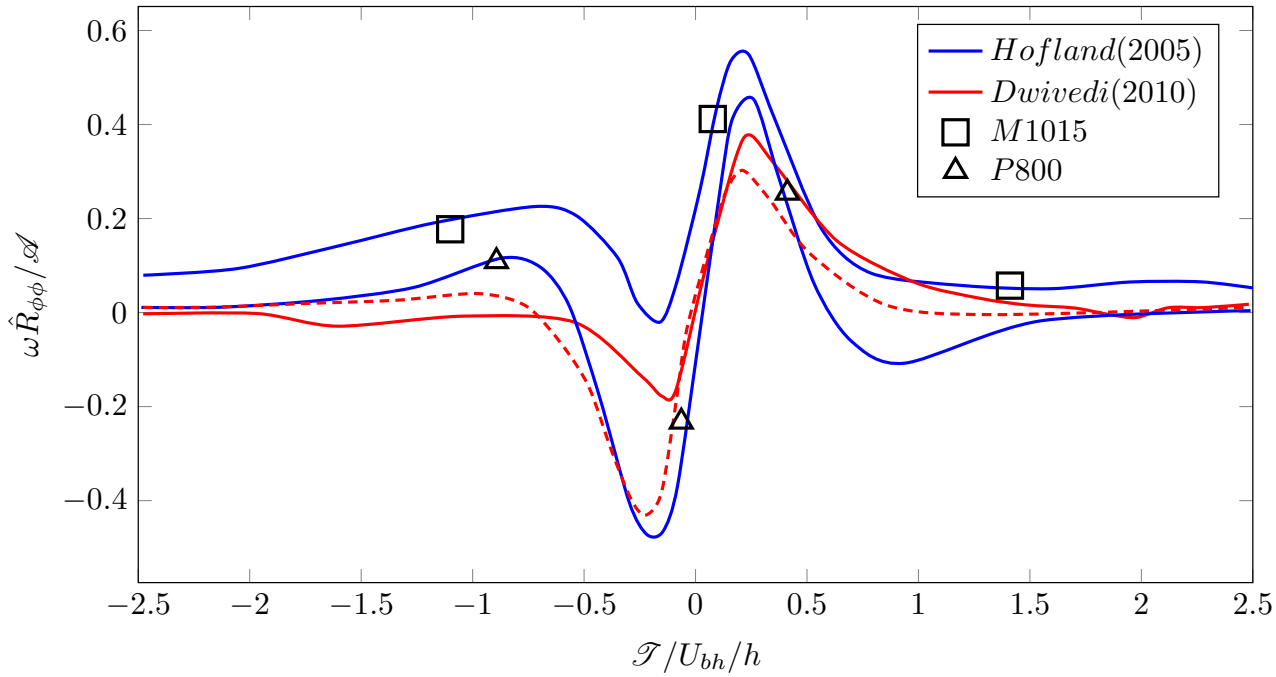



b




c

Figure 4.21: Pre-multiplied spectra $\omega\hat{R}_{\phi\phi}/\mathscr{A}$ of particle force fluctuations as a function of period $\mathscr{T}U_{bh}/h$. Spectra are normalised by $\mathscr{A}$ as defined in the text. The solid line is M1015 and the dashed line represents the P800 case




a

Figure 4.22: Cross-correlation of drag and lift fluctuation, $R_{FxFx}(\tau)/(\sigma_{Fx}\sigma_{Fx})$, as a function of time lag $\tau h/U_{bh}$. Figure shows the results of the case M1015 and case P800 in comparison with Hofland *et al.* (2005) and Dwivedi *et al.* (2010)

### 4.6.1 Time scales of cross-correlation between drag and lift fluctuations on a particle

In previous section it is shown that in the present case the time scales of drag and lift fluctuations, i.e. $\tau_{min}U_{bh}/h$ and $\tau_m U_{bh}/h$, are comparable with each other (table 4.4). Also the spectra in figure 4.21 behave similarly for drag and lift fluctuations. In contrast to this the time scales as well as the decrease of the spectra for large periods from case M1015 to P800 were found to differ for spanwise force fluctuations. This could be seen as an indication that, in the current setup, drag and lift fluctuations are related to similar flow structures and might be closely correlated in time, while spanwise force fluctuations are relate to somewhat different flow structures.

Figure 4.22 presents the cross-correlation of drag and lift fluctuations defined by (4.13) with $\phi = F_x'$ and $\omega = F_y'$. For $\tau = 0$, the correlation of drag and lift fluctuations is small, i.e., 0.23 (-0.06) in case M1015 (P800). However, a significant correlation occurs at a non-zero-time lag. The cross-correlation reaches a maximum value of $R_{FxFx}(\tau)/(\sigma_{Fx}\sigma_{Fx}) = 0.550$ (0.450) for a time lag of $\tau h/U_{bh} = 0.19$ (0.24) in case M1015 (P800). Thus, on average lift fluctuation follow drag fluctuation of equal sign with a time lag of about $0.2h/U_{bh}$. The cross-correlation reaches a local minimum of value $R_{FxFx}(\tau)/(\sigma_{Fx}\sigma_{Fx})$ = -0.03 (-0:49) for a time lag of $\tau U_{bh}/h$ = -0.17 (-0.20) in case M1015 (P800). While in case M1015 the correlation is essentially zero at the local minimum, in case P800 it reaches negative values, indicating that drag and lift fluctuations are on average of opposite sign at a time lag of $\tau U_{bh}/h$ = -0.20. As the time lag reaches higher negative values the correlation becomes positive once more, such that zero correlation is approached from above as the time lag goes to $-\infty$.

In addition to the results of case M1015 and P800, the results of two experimental studies

| Case | $\tau_\Delta U_{bh}/D$ | $\tau_\Delta U_{bh}/h$ | $\tau_\Delta u_\tau/D$ | $\tau_\Delta u_\tau/h$ | $\tau_\Delta u_\tau^2/\nu$ | $\tau_\Delta (u_\tau U_{bh})/\nu$ |
|---|---|---|---|---|---|---|
| M1015 | 6.01 | 0.34 | 0.40 | 0.023 | 4.3 | 65 |
| P800 | 2.01 | 0.42 | 0.16 | 0.034 | 7.9 | 98 |
| DW110 | 2.05 | 0.38 | 0.21 | 0.038 | 637 | 6373 |
| HOF05 | 2.56 | 0.46 | 0.36 | 0.065 | 1199 | 8437 |

Table 4.6: Difference of time-lag related to maximum and minimum in cross correlation of drag and lift, $\tau_\Delta$, in case M1015 and P800. The difference is normalised by various time scales and compared to the value obtained from the results of Hofland *et al.* (2005) (HOF05) and Dwivedi *et al.* (2010)(DWI10).

are presented in figure 4.22. One data set was taken from Hofland *et al.* (2005) at his lowest protrusion height. The author indirectly measured drag and lift by the difference of two pressure measurements on a cube with a height of $3300\delta_\nu$ at $Re_b = 1.3 \cdot 10^5$. The ratio of channel width to open channel height was 3.0 and the ratio of cube height to open channel height 5.6. The other data set is taken from Dwivedi *et al.* (2010), who directly measured drag and lift on a spherical particle with $D^+ = 3100$ in a hexagonal packing of spheres with zero protrusion at $Re_b = 1.68 \cdot 10^5$. The ratio of $H/D$ was 5.4 and thus comparable to the one of case P800 and the measurements of Hofland *et al.* (2005). The width of the open channel flow was $W/H$ = 2.1 which is also comparable to the one of Hofland *et al.* (2005). The latter ratio should be considered low and in both experiments strong influences of secondary currents have to be expected. In spite of the different Reynolds numbers and particle shapes considered in the experiments, the obtained cross-correlations agree well with the results of case M1015 and P800. Largest differences are found in the value of the maximum and the minimum.

To study the comparison in more detail and address some scaling issues table 4.6 lists the difference between the time lag of maximum and minimum in figure 4.22, $\tau_\Delta$, normalised by the six time scales. As can be seen, the value of $\tau_\Delta$ normalised by a scaling which involves $u_{tau}$ increases with increasing $D^+$. Scaling $\tau_\Delta$ using $D/U_{bh}$ leads to strong difference between case M1015 and the other results. The best agreement is found when $\tau_\Delta$ is scaled by $h/U_{bh}$, i.e, $\tau_\Delta U_{bh}/h = 0.40 \pm 0.6$.

To conclude, it was found that drag and lift are related though with a shift in time. Profiles of drag and lift correlations from experiments at much higher Reynolds numbers are of comparable shape. As one of the experiments approximated the drag and lift by few pressure measurements only, the agreement with direct measurements of the forces and the present results point towards a strong influence of pressure on the relation. This interpretation is in favour of a model approach proposed by Hofland *et al.* (2005)) based on a convected frozen pressure field. Also, the agreement might be partly explained by a lack of scale separation. In the simulation this is due to the small Reynolds number considered, but also due to a small ratio of $h/D$. In the experiments the particle Reynolds numbers are large, and force fluctuation on the particle might be expected to be independent of the viscous scale. However, the ratio of open channel height to characteristic roughness length is small and thus $h/U_{bh}$ might be the relevant time scale for these configurations.

## 4.7 Summary, conclusion and recommendation for future work

Direct numerical simulation of open channel flow over a geometrically rough wall was performed at a frictional Reynolds number of $Re_\tau \approx 300$. The wall consisted of a layer of monodispersed spheres touching a layer of polydisperse particles. The results of case P800 with $D^+ = 10.7$ ($Re_\tau = 188$), were compared with case M1015 with $D^+ = 49.3$ ($Re_\tau = 235$). In case M1015 the effect of roughness on the flow field statistics was small, and the limit of the hydraulically smooth flow regime is approached. In case P800 the roughness effect was stronger, and the flow is in the transitionally rough flow regime.

The complexity of the time-averaged three-dimensional flow field within the roughness layer was discussed in detail. In both cases a re-circulation forms downstream of the spheres that is connected over the entire spanwise direction, being more pronounced in the large-sphere case. Three dimensionalities above the roughness layer are lost rapidly with wall distance, yielding a time-averaged flow field which is essentially one-dimensional beyond two particle diameters.

A main result of this chapter is the characterisation of the force and torque acting on a particle due to the turbulent flow. It was found that the mean drag on a sphere is 4% (case M1015) and 15% (case P800) higher than the reference force $F_R = \rho_f u_\tau^2 A_R$, where $A_R$ is the wall-normal projected area of the wall per particle. Given the definition of the friction velocity, these numbers reflect the fact that the drag force on the roughened bottom wall (below the fixed spheres) is small. In both cases a strong positive lift was obtained in agreement with previous experiments, exceeding values of 18% and 32% for M1015 and P800, respectively, of the corresponding drag. The values of the mean spanwise torque on a particle are comparable to $-F_R r_R$, where $r_R$ is the distance from the particle centre to the position of the virtual wall, located at a distance of $y_0 = 0.8D$ from the plane part of the solid wall. It was shown that in both cases the mean drag, lift and spanwise torque are to a large extent produced in a region of the particle surface which is located above the virtual wall ($y > y_0$). The spatial distribution over the particle surface of the stresses that lead to time-averaged drag, lift and spanwise torque are found to be similar in shape in the two cases.

It was observed that the intensity of particle force fluctuations (when normalised by $F_R$) is significantly larger in the large-sphere case. Conversely, when analysing the torque it is found that only the fluctuation intensity of the spanwise component is larger in the large-sphere case, whereas the two remaining components exhibit smaller fluctuation intensities when the sphere is larger. By means of a simplified model it was argued that the torque fluctuations might be explained by the spheres acting as a filter with respect to the size of the flow scales which can effectively generate torque fluctuations. As a model the shear forces and torque exerted by the flow on a square wall element in a smooth wall configuration were considered. By systematically varying the linear dimension of the wall element the influence of the length scale was analysed. Here it is found that the normalised fluctuation intensity of the streamwise and spanwise shear forces monotonically decreases with the filter size, while the wall-normal torque experiences a maximum of normalised fluctuation intensity for intermediate filter sizes of approximately 70 wall units. By if the largest part of the particle torque fluctuations is generated in a small area around the particle tops, the results from the simplified model carry over to the corresponding components of the particle torque. Indeed, a reasonable agreement was obtained between standard deviation and kurtosis of shear forces and torque acting on a

square wall element on the one hand and respective particle torque components on the other hand. However, since only two cases were considered, it cannot be stated with certainty that wall-normal particle torque fluctuations are indeed most intense at the above-mentioned scale of 70 wall units. Similarly, based on the current data it is not possible to judge whether the model can provide insight into the fully rough flow regime. These points should be clarified in future studies.

Fluctuations of both force and torque were found to exhibit strongly non-Gaussian probability density functions with particularly long tails. The deviation from a Gaussian distribution was significantly smaller in the large-sphere case, which was attributed to the smaller effect that highly intermittent small scales have on the larger-particle surface area. Moreover, it was observed that the spanwise torque component has a marked negative skewness. In the light of the analogy with a wall element in a smooth wall configuration, this finding is consistent with the positive skewness of the streamwise velocity fluctuations near the wall in a smooth wall channel flow.

The time scales of force and torque fluctuations were studied by means of auto-correlation functions. In the present case, a separation of small- and large-time scales does not exist, because of the small Reynolds number considered. The time scales are of order one when scaled by the bulk velocity and effective channel height. An exception is the time scale of spanwise torque on the particle which appears to be biased by the streamwise domain size. In the large sphere case, the autocorrelation of force on the particle reveals pronounced minima with negative values. Local minima are also found in the small sphere case but of much lesser extent. The autocorrelation of torque on the particles differ little in both cases and do not exhibit a similar minimum. It was speculated, that the minima are related to the pressure contribution to drag. Some support for this hypothesis comes from the autocorrelation of pressure at a smooth wall which is known to exhibit a pronounced minimum of negative value. The maximum of the pre-multiplied spectra reveals that the scale related to the minima in the autocorrelation contributes most to the force fluctuations on the particle.

The cross-correlation between drag and lift shows that the two particle quantities are closely related with a shift in time. The time scales of the correlation compare best when scaled by outer flow units. Comparison to experiments point towards a strong influence of pressure on the correlation, which is in favour of the model by Hofland (2005) that approximates the drag-lift correlation by results from a converted pressure field.

The convection velocity of force and torque on particles were studied with the aid of space-time correlations. In the M1015 case, the convection velocities are in the range commonly reported for smooth wall simulations when scaled with outer flow units ($U_c/U_{bh} = 0.56 to 0.71$), but somewhat lower than the values in the literature when scaled in viscous units ($U_c/u_\tau = 8.5 to 10.8$). In the P800 case, the convection velocities are smaller ($U_c/U_{bh} = 0.46 to 0.61, U_c/u_\tau = 5.6 to 7.5$), which can possibly be linked to the effect of roughness on the flow above the spheres.

The regions of significant correlation between the flow field and particle force and torque fluctuations are of sizes comparable to the effective open channel height. For the correlation between particle quantities and streamwise velocity fluctuations, the regions of significant positive correlation are elongated in streamwise direction over several channel heights. The regions are flanked by regions of significant correlation with alternating signs at a spanwise distance comparable to the distance of high-speed streaks to low-speed streaks in smooth wall flows. The correlations of drag fluctuations and streamwise velocity fluctuations were compared to the correlations of spanwise torque and streamwise velocity fluctuations as well as to the correlations of

drag fluctuations to pressure fluctuations. The results show that pressure is strongly correlated to drag fluctuations in both cases. The results can be interpreted in favour of the idea that pressure has a large effect on the characteristics of drag on a particle in the large sphere case and a profound effect in the small sphere case, although here the hydraulically smooth regime is approached. The regions of significant correlations between flow field and spanwise force fluctuations or streamwise torque fluctuations are of sizes comparable to the channel height and exhibit complex shapes.

The overall picture is that in the present cases force and torque on a fixed particle are related to velocity fluctuations in a region with a size comparable to the effective channel height. The time scales as well as the velocity scales related to force and torque are of order one when scaled with outer units. Future direct numerical simulations at higher Reynolds numbers would be beneficial to further address scaling aspects of the results above. Also, experiments at high ratios of channel height to particle diameter would be needed to deepen the understanding of the correlation of turbulent flow to force and torque on particles.

*"The task is not so much to see what no one has yet seen; but to think what nobody has yet thought, about that which everybody sees."*

Erwin Schrodinger (1887 - 1961)

# 5

# Sediment transport in open channel flow at low relative submergence

This part presents a DNS of sediment entrainment events. The simulation setup is like the fixed sphere configuration, however, here truly mobile particles are considered that can erode from the bed. The simulations follow the approach of Clemens *et al.* (2011) and are a first step towards deepening the understanding of the fundamentals involved in the onset of sediment erosion. However, it must appreciate that due to intense computational requirements and the number of particles studied, there is a considerable amount of research required to fully understand the complexities which, dictate a particle to move. Still, the simulations provide comprehensive data to guide future research and is not limited to systematically arranged lattice beds. The approach to model, closer to a natural sediment bed will facilitate in progressing the research field to direct numerical simulations of the onset of sediment transport.

## 5.1 Numerical setup

The setup of the simulations is equivalent to the setup of case M1015 and case P800 introduced in chapter 4. In contrast to these fixed sphere simulations, here $N_p^f$ particles are mobile and can erode from the initial bed configuration. To account for the particleparticle contact the artificial repulsion potential of Glowinski *et al.* (1999) is applied. Note, that a model to account for particlewall contact is not needed in the present simulations, due to the roughening of the rigid wall below the layer of particles by particle caps. The particle caps support the particles in their initial position.

In the following, the simulations of sediment erosion are classified into simulations of multiple particle erosion (M) and simulations of single particle erosion (S). In simulations of multiple particle erosion, all particles in the layer are mobile. In simulations of single particle erosion, only 10 particles are mobile while the other particles remain fixed. The 10 mobile particles have been selected such that they are positioned in regions of high force events during simulations

| Case | $N_p^f$ | $\rho_p/\rho_f$ | $gh/U_{bh}^2$ | $\theta_s$ | $\tau_c U_{bH}/H$ | *erosion* |
|---|---|---|---|---|---|---|
| S10-L1 | 10 | 1.25 | -0.69 | 0.43 | 6 | no |
| S10-L2 | 10 | 1.25 | -0.35 | 0.87 | 10 | no |
| S10-L3 | 10 | 1.25 | -0.14 | 2.17 | 19 | yes |
| S10-L4 | 10 | 1.25 | -0.07 | 4.35 | 8 | yes |
| S10-L5 | 10 | 1.25 | -0.03 | 8.70 | 8 | yes |
| S10-H1 | 10 | 1.7 | -0.14 | 0.78 | 6 | no |
| S10-H2 | 10 | 1.7 | -0.07 | 1.55 | 6 | yes |
| M10H1 | 800 | 1.7 | -1.38 | 0.08 | 13 | no |
| M10H2 | 800 | 1.7 | -0.69 | 0.16 | 10 | yes |
| M50H1 | 1015 | 1.7 | -0.39 | 0.11 | 26 | no |
| M50H2 | 1015 | 1.7 | -0.26 | 0.17 | 13 | yes |
| M50H3 | 1015 | 1.7 | -0.17 | 0.26 | 12 | yes |

Table 5.1: Parameter of simulations to study the onset of single particle (S) and multiple particle (M) erosion. The setup is analogously to that of case M1015 and case P800 introduced in chapter 4. However here, $N_p^f$ particles are mobile and able to erode from the initial bed configuration. The ratio of particle density and fluid density is $\rho_p/\rho_f$, two ratio were considered a low value (L) of $\rho_p/\rho_f = 1.25$ and a somewhat higher value (H) of $\rho_p/\rho_f = 1.7$, $gh/U_{bh}^2$ is the normalised gravitational volume force $\theta_s$ is the Shields parameter defined by 2.2, $\tau_c U_{bH}/H$ is the total observation time of the simulation, the last column indicates whether or not particle erosion occurred.

involving only fixed spheres. Furthermore, the mobile particles are located far away from each other to minimise possible collective effects. Figure 5.1 illustrates the position of the released particles in cases S10 by coloured circles.

Table 5.1 summarises the details of the considered cases. At the current state of the research, the small sphere case is investigated in most detail. Single as well as multiple particle erosion was studied. Two ratios of particle density to fluid density were considered, one with a low ratio of $\rho_p/\rho_f = 1.25$ (L) and one with a somewhat higher ratio $\rho_p/\rho_f = 1.7$ (H). Both ratios are smaller than the commonly found value of $\rho_p/\rho_f = 2.65$ for rock material in water (for example Van Rijn *et al.* (1993); Vanoni (1975)) but compare well to previous experiment using Nylon spheres, Ping-Pong balls or artificial stones (Hofland *et al.* (2005), $\rho_p/\rho_f = 1.5$, Cameron *et al.* (2008), $\rho_p/\rho_f = 1.12$ - 1.34). For the large sphere case only multiple particle erosion events were carried out. In all simulations gravity was applied in direction perpendicular to the wall and successively increased until the particles did not erode. That is, particles moved less than half a radius from their initial position during the run-time of the simulations. The initial flow field was taken from case M1015 and case P800. A specific conditioning of the instant of time was not needed as local high force events occur evenly distributed over the entire run-time of case M1015 and case P800. The duration of each simulation is provided in table 5.1. Note, that the observation times are moderate and longer durations would be preferable. The durations of the simulations are a compromise between computational costs and the minimal time needed for sediment erosion to occur in some cases.

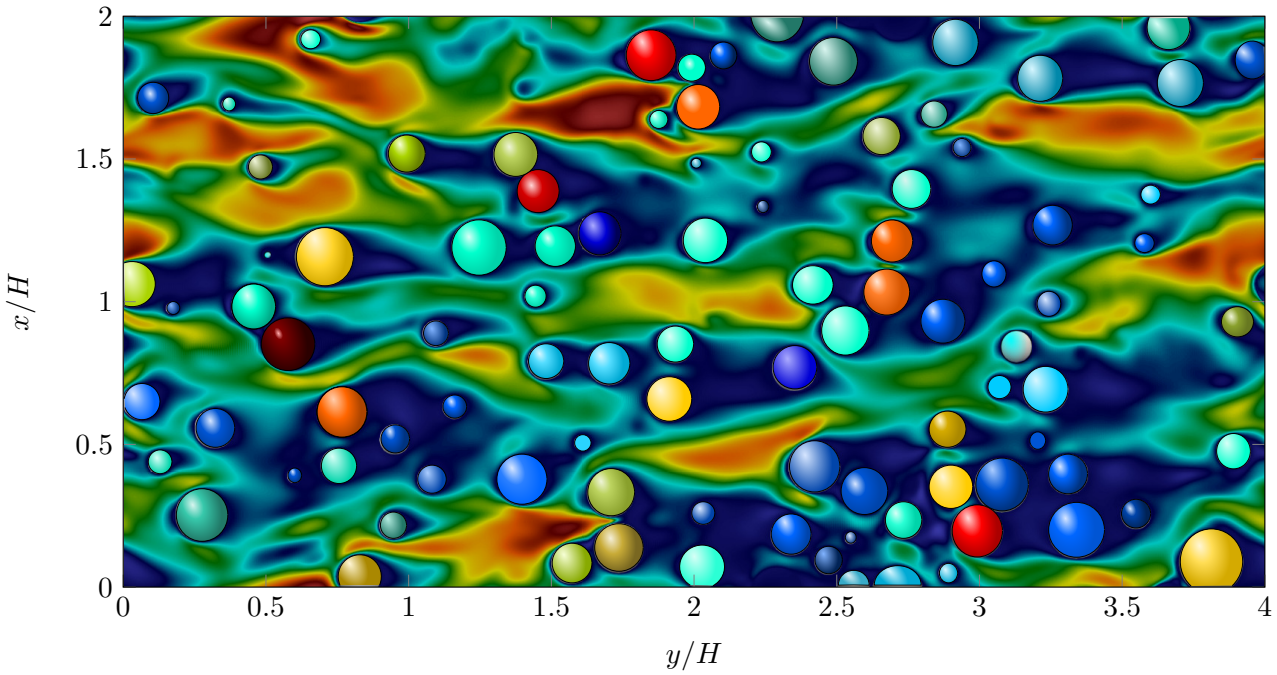



Figure 5.1: Snapshot of mobile particles in turbulent channel flow

## 5.2 Results

Figure 5.2 illustrates the results of table 5.1. Additionally, the figure shows the area given by Shields (1936) to distinguish the parameter range in which sediment erode (above) and in which particle remain at rest (below). It should be stressed once more, that the results presented here are the results of few simulations. Therefore, the results do not represent mean values and thus do not represent averaged critical Shields numbers. Figure 5.2 indicates that the critical Shields number are higher for the larger sphere case for multiple particle erosion. This is in good agreement with Clemens *et al.* (2011)who carried out similar simulations, albeit in a smaller box and considering particles with sizes of $D^+ = 12.3$ and $D^+ = 108.0$. In the study of Clemens *et al.* (2011) the critical Shields parameter above which sediment erosion occurs was $\theta_{thres} = 0.12$ in the small sphere case and $\theta_{thres} = 0.17$ in the large sphere case. These values match well with the present data. The observed trend of an increase in the critical Shields number increases with increasing $D^+$ from 12 to 108 is in agreement with Shields (1936). Figure 4.25 illustrates the trend of the literature by the shaded area provided by Shields (1936). While the trend of the present simulations matches the experimental evidence, the value of the critical Shields numbers are exceptionally high and do not compare with either the results of Shields (1936) with the results of other researchers (Buffington & Montgomery (1997)). This is even more pronounced in case of single sphere erosion, for which the critical Shields number, $\theta_{thres}$, is obtained an order of magnitude higher than the values commonly reported. Possible explanation of this shortcoming might be the limitation to short simulations times in the present simulations or the limited number of mobile particles. However, other explanations exist, for example it is well known that the exposure of particles strongly influences the value of the critical Shields number (Fenton & Abbott (1977); Cameron *et al.* (2008)). In the present case the eroding particles are initially fully submerged inside of the particle layer. In case of single particle erosion this remains true during the simulation prior of erosion. This aspect might contribute to the obtained higher values of the critical Shields number in particular for the

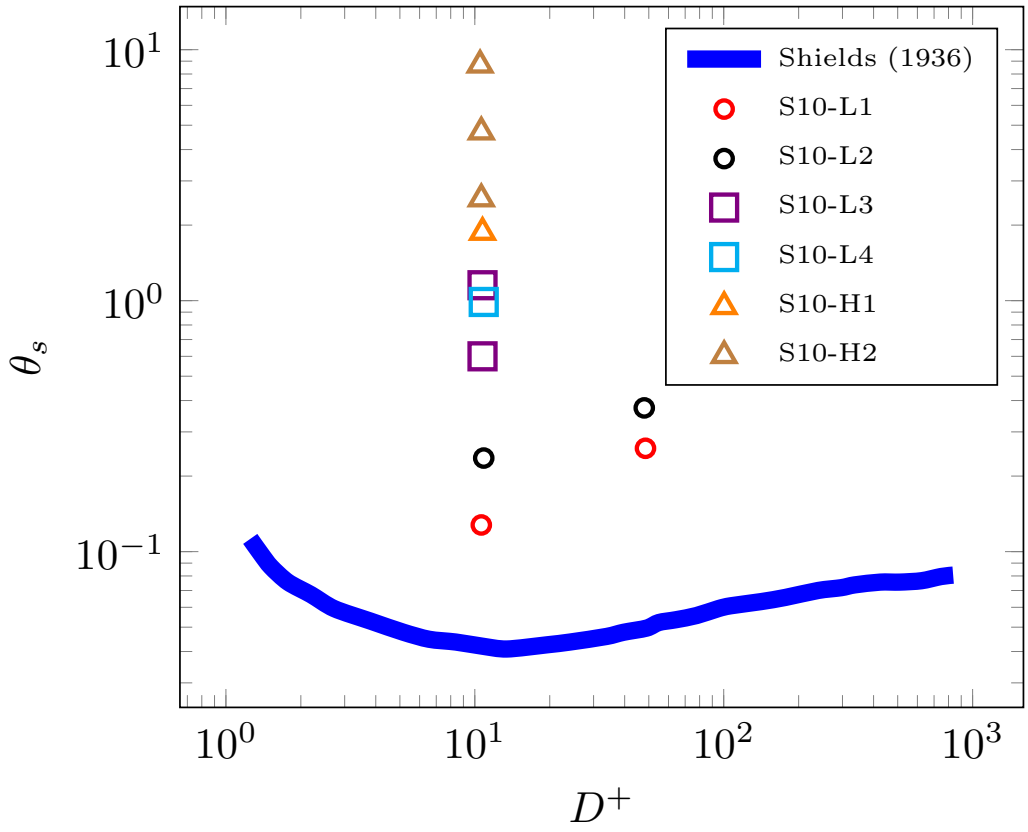


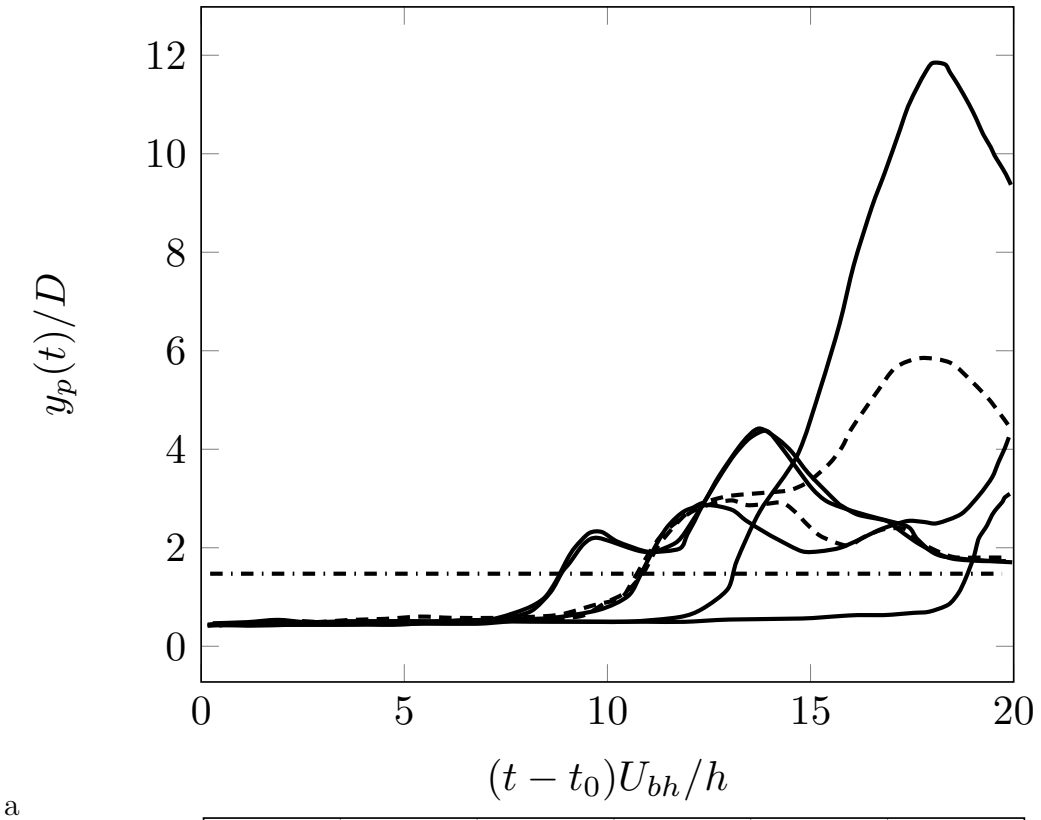

Figure 5.2: Shields parameter $\theta_s$ in simulations of table 5.1 as function of particle diameter in viscous units $D^+$.

single particle erosion cases.

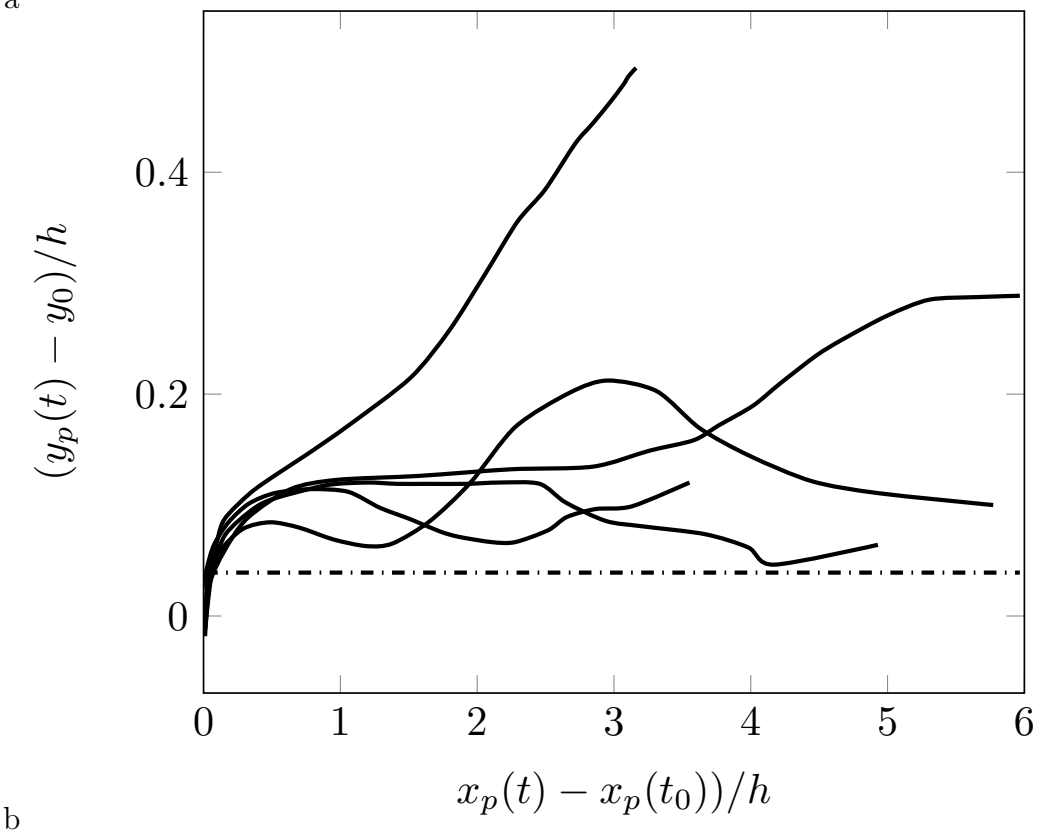
Figures 5.3 and 5.4 analyse particles quantities during entrainment in simulations S10L3. Figure 5.3(a,b) shows the vertical position of the particle centres as a function of time and streamwise distance, respectively. Figure 5.3(b) illustrates that most particles in the simulation reach a height of $(y - y_0)/h$=0.12 within their initial movement. From there they are convected downstream prior to moving back towards the wall or further away from it. However, some particles do not follow this trend. For example the first eroding particle, which erodes around $6h/U_{bh}$ after the start of the simulation, reaches heights of about $(y - y_0)/h$=0.09, moves back towards the wall after the initial erosion prior to reaching higher values of $(y - y_0)/h$ up to 0.2. Another particle, eroding around $(t - t_0)U_{bh}/h$=13, is dispersed rapidly far into the outer flow. Here, $t_0$ is the time at the beginning of the simulations.

Figure 5.4 shows the time signals of the entrained particles with reference to $t_{thres}$ defined as the time for which $y_p(t)$ equals 1.5D, i.e. $y_p(t_{thres}) = 1.5D$. Figure 5.4(a) shows that the particles reach a wall-normal distance of $y_p = D = 2.2$ within an interval of less than $2h/Ubh$. Remarkable is, that the eroding particles in this simulation are already somewhat lifted from their initial position prior to the entrainment. Figure 5.4(b) shows the wall-normal velocity of the particles. The particles are strongly accelerated from about $(t - t_{thres})U_{bh}/h = 1$ until $t_{thres}$. The particles wall-normal velocities vary in the range of about $1u_\tau$ to $2u_\tau$. This is in agreement with the results of Cameron (2006) who similarly reported wall-normal particle velocities of the order of $u_\tau$ during the entrainment process.

These velocities can be regarded as high, i.e. they are higher than the maximum standard




a




b

Figure 5.3: Wall-normal position of particle centres, $y_p(t)$, of mobile particles in case S10L3, (a) as a function of time $(t-t_0)U_{bh}/h$, (b) as a function of streamwise distance from initial position, $(x_p(t)-x_p(t_0))/h$. Here, $t_0$ is the initial time of the simulations and $x_p(t_0) = (x_p(t_0), y_p(t_0), z_p(t_0)$ the initial position of a particle. Dashed lines are introduced to guide the eye and show location of $y = 1.5D$ which is the location of a particle centre positioned on top of a particle with $y_p = D/2$.

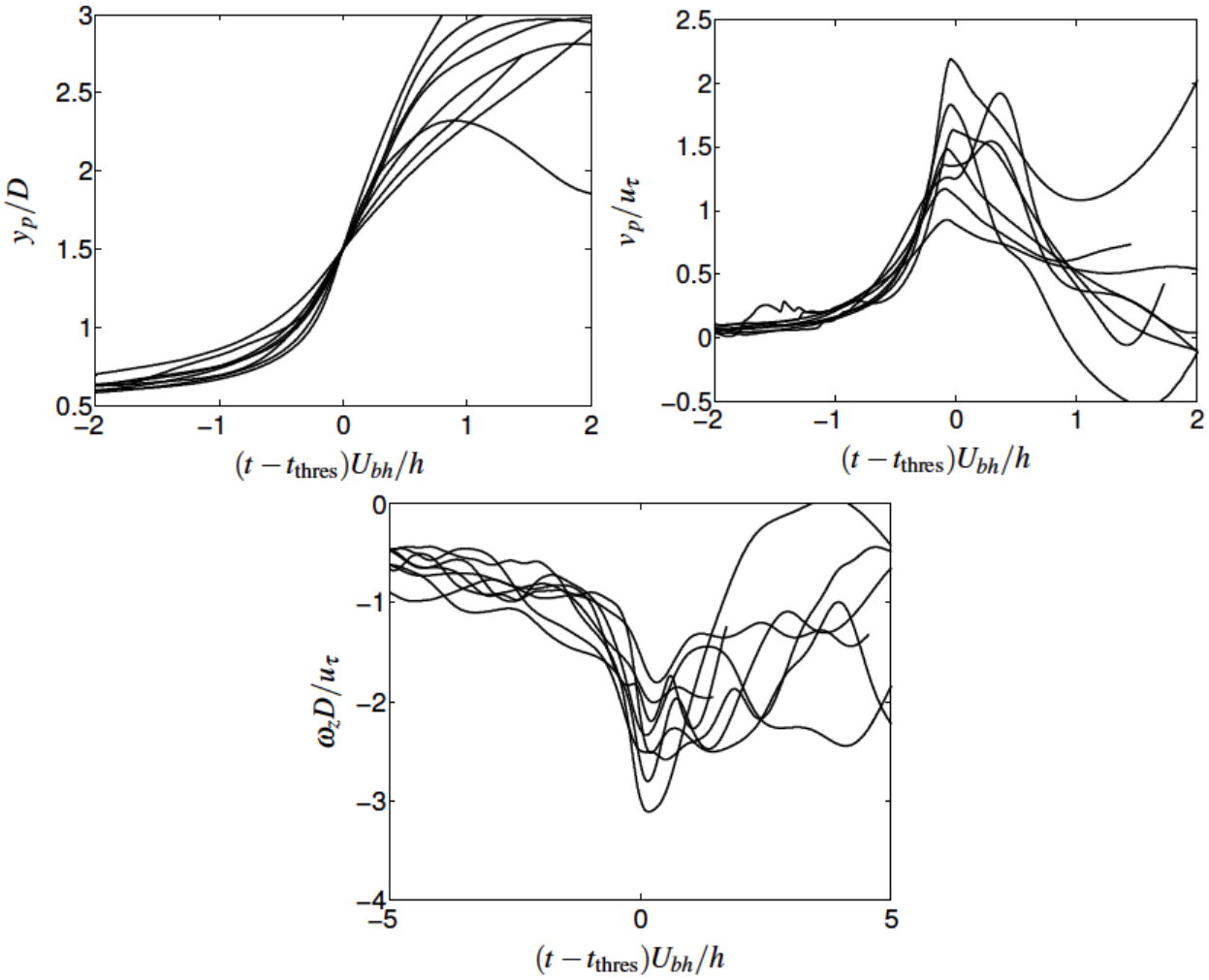



Figure 5.4: Time signals of mobile particles in case S10L3. (a) Wall-normal particle position, $y_p/D$, (b) wall-normal particle velocity, $/nu_p/u_\tau$ and (c) spanwise angular velocity, $/u_tau$. Time signals are shown as a function of $(t - t_{thres}U_{bh}/h$ where $t_{thres}$ is chosen as the time the respective particle reaches a wall-normal position of 1.5D, i.e., $y_p(t_{thres}) = 1.5D$.

deviation of wall-normal velocity close to the wall in case M1015. Along with the high acceleration in wall-normal direction the particles are exposed to high angular acceleration in spanwise direction (figure 5.4). This could be an indication that high values of lift and spanwise torque and related to this also drag coincide in the moment of erosion in the present case. It is remarkable that the wall-normal acceleration of the particle appears to stop as soon as the particle loses its contact from the surrounding particles, i.e. at $t_{thres}$. It was found that the results of most simulations close the critical Shields number exhibit similar characteristics as those discussed above (plots omitted). This was found to be true not only for the single particle erosion, but also for the cases with multiple particle erosion. While in the small sphere case similar values are obtained, the time of acceleration is about twice as long in the large sphere case. Also, in this case the wall-normal velocities of the particles and the wall-normal positions reached are higher. The following summarises the picture of the erosion process which is derived from analysing the data of the simulations analogously to figure 5.4 as well as with video-clip of the erosion process (Tait *et al.* (1992)). In the present simulations, mobile particles start to rotate preferentially along the spanwise axis. Note, that the angular velocity of most particles is non-zero within the time range shown in figure 5.4(c). This is caused by the simple contact model employed in the present simulations, that does not consider tangential forces during contact. Such forces would prevent rotation in case of resting particle. In case of multiple particle erosion, mobile particles rotate around the spanwise axis. During erosion particles exhibit a strong acceleration and move away from the wall. This is often related to a duration of about $2h/U_{bh}(4h/U_{bh})$ in the small (large) sphere case. During entrainment the particles are exposed to both high acceleration in wall-normal direction as well as high angular acceleration around the spanwise axis. In case of multiple particle erosion, the motion of particles appears to be strongly correlated along streamwise rows. This collective motion expands in streamwise distances over several $h$ lengths. In the small sphere case the collective motion appears to be smaller than the streamwise length of the domain. In the large sphere case the collective motion extents over the entire domain length and entire rows begin to move collectively downstream. A similar phenomenon was reported by Uhlmann & Fröhlich (2008)). This among others, indicates that collective effects play an important role for multiple particle erosion in the present cases. Interestingly, the details of sediment erosion as analysed analogously to figure 5.4 are rather similar for multiple as well as single particle erosion.

From the results of Clemens *et al.* (2011) it might be speculated, that for the present small sphere cases single as well as multiple particle erosion might be linked with the passing of a high-speed streak above the eroding particle in combination of a near-by low-speeding streak and hairpin like vortices. The results are agreement with findings of Hofland *et al.* (2005)and Cameron *et al.* (2008) that the entrainment of particle appears to be correlated with events of high streamwise velocity fluctuation jointly with negative wall-normal velocity fluctuations. The authors also reported that the erosion appears to be related with the occurrence of pronounced spanwise vortices. Similar conclusions for the large sphere case would require additional analysis.

## 5.3 Summary, conclusion and recommendation for future work

This chapter focused on the study of sediment erosion. First the implications of fixed sphere results were considered, then direct numerical simulations with mobile particles were studied.

To investigate events in fixed sphere simulations that could be related to sediment erosion, a criterion is required that predicts sediment erosion on the basis of force and torque on fixed spheres. Such a criterion might be defined by a critical threshold of drag, lift or spanwise torque above which sediment erosion is predicted. More elaborate criteria consider possible motion of particles during erosion based on the given geometry. Here two motions are taken into account, translational motion tangentially to the plane of contact with the supporting particles, and rotational motion around the axis of contact points. The onset of sediment erosion can then be defined by thresholds of the force tangential to the contact plane, or the torque around the axis of support. However, for the present cases it is found that these criteria are equivalent to consider a threshold of drag, i.e. the cross-correlation coefficient of the tangential force with drag is approximately one for the present cases, as is the magnitude of the cross-correlation coefficient of torque around the axis of support and drag. A similar equivalence between the criteria of drag, lift or spanwise torque could not be established for the present cases. The various cross-correlations coefficients between the quantities exceed moderate values. Additionally, the two-dimensional probability density function of drag and lift was examined for time-lags that maximise the correlation coefficient. The results suggest, that although drag and lift are correlated, they might lead to different predictions of the onset of sediment erosion.

The implications of a certain threshold on the conditioning criteria are studied by the number and the mean duration of time intervals. The time intervals are defined as the sequences in which the time series of drag, lift and spanwise force exceed a given threshold. Events of high drag or lift, i.e. with a value of five standard deviation higher than the mean, are rare and on average part of a time sequence with a pronounced single maximum. The mean duration of these sequences is found to be of the order of the smallest scales. In case of spanwise torque, a criterion of five standard deviations above the mean similarly selects rare events with a short mean duration. However, the results of the analysis indicate that even for short durations the signals of spanwise torque contain several local maxima.

Conditionally averaged time signals of drag, lift and spanwise torque on fixed particles are presented. The conditioning criteria was drag, lift and negative spanwise torque five standard deviations higher than the mean. It is found, that the conditionally averaged time signals depend heavily on the conditioning criteria. In particular, the shape of each profile is closely related to the correlation function of the conditioning quantity and the averaged quantity. This appears to be true despite the high threshold employed. The results show, that high drag events correlate to high lift events and vice versa. The conditionally averaged time signals have common features between the small and the large sphere case. In contrast to this, the averaged profiles of spanwise torque conditioned to high drag or lift differ in their characteristics from the small sphere case to the large sphere case. Also, the magnitudes of the profiles are small for the large sphere case. Considering both cases, the highest magnitudes of conditionally averaged drag, lift and spanwise torque are obtained with drag as a conditioning criterion.

Instantaneous flow fields conditioned to high drag events show, that particles of high drag are often located close-by highly negative pressure fluctuations in the vicinity of a pair of high- and low-speed streaks. Frequently, the particles are within a region of high turbulence activity which might resemble burst events. However, in particular for the small sphere case particles can also be in regions where the flow is less active. Similar to the conditionally averaged time signals of force and torque on a particle, the conditionally averaged flow field compares in shape to the correlation function between flow field and conditioning quantity. A possible explanation of the agreement is to assume, that high drag events dominate the correlation

function. However, given the high threshold criterion considered, i.e. five standard deviations higher than the mean, it seems unlikely that these rare force events of small probability should dominate the correlation. Another explanation is to assume, that the flow structures related to drag events are similar in shape independently of the strength of the force and torque. Some support for such an assumption can be gained from the results of Johansson *et al.* (1987). The authors found that pressure signals in a boundary layer conditionally averaged to high and low peaks are similar in shape albeit with opposite sign. This aspect deserves further clarification in future research.

The conditionally averaged flow fields were compared with the results of Detert *et al.* (2010). The authors studied experimentally the conditionally averaged flow over natural gravel at much higher Reynolds numbers. Their conditioning criterion might be interpreted as a strong increase in lift on the particle. Despite the differences in flow configuration and conditioning criterion, the conditionally averaged velocities exhibit similar characteristics in strength and in size. In particular, the authors report high streamwise velocity fluctuations above the particle, elongated in streamwise direction over several particle diameter. Also, the authors observed averaged velocity fluctuations directed towards the wall close-by the particle. The conditionally average spanwise velocities in the vicinity of the particle are directed away from the particle, similar to the results in this study. In contrast to the good agreement of the conditionally averaged velocity fields, the conditionally averaged pressure field in the experiment differs to the present cases. Detert *et al.* (2010) report averaged pressure fluctuations of negative value upstream and of positive value downstream of the particle which, taking the conditionally averaged flow motion into account, appears to be counter intuitive. In the present cases the conditionally averaged pressure fluctuations are of similar size but of opposite sign.

The definition of a Shields number based on instantaneous lift and the gravitational force on fixed particles was used to assess the potential for sediment erosion. From the histograms of lift it was concluded, that the critical Shields number to define the onset of erosion is smaller in the large-sphere case as compared to the small-sphere case. The same trend was found when considering Shields numbers based on the forces projected onto the direction tangential to the downstream contact point between spheres in neighbouring positions as well as when evaluating the balance of angular moments around the contact point. Experiments in the literature with truly mobile particles seem to indicate the opposite trend (increasing critical Shields number with increasing particle size in the range of D+ 10 to 100). However, these opposite trends do not necessarily imply a contradiction, since additional effects which might play a role in the dynamical process of erosion are not addressed when considering fixed particles. Two important idealisations with respect to real-world sediment erosion are made in the considerations above: the regularity of the geometrical arrangement and the immobility of the particles. Concerning the geometry, it is expected that different particle arrangements, size distributions and shapes will lead to a modification of the forces acting upon sediment particles. In particular, varying the protrusion of individual particles has been shown to have a significant effect on the onset of erosion (Fenton & Abbott (1977); Cameron *et al.* (2008)). In this respect, the fixed particle configuration studied in the present work can be considered as a case where mutual sheltering of particles is high due to their uniform diameter, spherical shape and regular arrangement.

Concerning the immobility of the particles, several consequences arise from this idealisation which could potentially affect the implications for sediment erosion: (i) the modification of the flow field by the particles during the incipient motion; (ii) the determination of the temporal duration of force- and torque-generating flow events which is necessary in order to achieve irreversible onset of particle motion; (iii) the influence of collective mobility. In order to evaluate

some of these mobility effects, additional simulations of sediment erosion with mobile particles were carried out.

The simulations with mobile particles require a model to account for the particle-particle contact. Here, a simple repulsion force model was applied which only considers contact forces normal to the plane of contact and does not account for tangential friction forces. For both cases erosion events are simulated in which all spheres of the particle layer are mobile. The ratio of particle density to fluid density was 1.7 in both cases. The gravity towards the wall was varied to achieve different Shields numbers. For the few simulations considered the critical Shields number was found to be higher for the large sphere case than for the small sphere case. Thus the simulations are in line with the trend of previous experiments. However, the value of the critical Shields numbers in the simulations are considerably higher than the values in the literature. This could be related to the limitation of the direct numerical simulations to small observation times and moderate numbers of mobile particles. Another explanation could be, that for the present setup sheltering effects might be strong (see discussion above).

Particle erosion with an entire layer of mobile spheres exhibit collective motion of particles. To assess the implications of collective effects on the onset of erosion, additional simulations of particle erosion were carried out in which single, isolated spheres are mobile and erode from an otherwise fixed layer of spheres. These simulations have been considered for the small sphere case only. The critical Shields numbers was much higher in these simulations, which suggests that collective effects indeed play a role in the previous simulations.

*"I wanted a perfect ending. Now I have learned the hard way, that some poems don't rhyme, and some stories don't have a clear beginning, middle and end."*

Gilda Radner (1946-1989)

# 6

# Conclusions and future work

Open channel flow, sediment erosion and sediment transport are of particular interest for hydraulic engineering. For example the control of rivers and hydraulic structures, such as weirs or dams, require formulae to estimate the flow behaviour, the onset of sediment erosion and sediment transport rate. Current formulae are mostly based on empirical relations and on bulk quantities of the flow. The predictive power of these formulae is low. This reflects to some degree a lack of sound understanding of the underlying physics and a need for data with sufficient resolution of flow field and particle related quantities. This thesis contributes to close these gaps of knowledge by providing and analysing highfidelity data of open channel flow, sediment erosion and sediment transport. The data is generated by direct numerical simulations employing an immersed boundary method to resolve the particle boundary. Three different configurations are studied: (i) open channel flow over fixed mono and poly disperse spheres and (ii) open channel flow with sediment transport of many mobile particles. The analysis of the data focused on three aspects: (a) the characterisation of force and torque on fixed particles and the related flow structures, (b) the characterisation of events that lead to sediment erosion based on results of fixed sphere simulations and simulations of erosion events with mobile particles and (c) the effect of many mobile particles on the statistics of flow field and particle related quantities. A brief summary with conclusions on each of these aspects is given below, followed by recommendations for future work. A more detailed discussion on the aspects (ac) is provided at the ends of chapters 4 and 5.

## 6.1 Open channel flow over fixed spheres

Direct numerical simulations of open channel flow over a layer of fixed spheres in a poly and monodisperse arrangement were performed. Two cases have been considered. In the first case, the spheres are monodisperse (with diameters equivalent to 10.7 wall units) and the limit of the hydraulically smooth flow regime is approached. In the second case, the spheres are polydisperse (49.3 wall units) and the flow is in the fully rough flow regime.

The flow field was studied with respect to its space and time-averaged statistics, the influence of roughness as well as the statistics of its three-dimensional time-average. The analysis of the flow over fixed spheres focused on the characterisation of force and torque on a particle and the related flow structures. The thesis provides a discussion of the statistics of force and torque, the correlation functions of force and torque in time and space-time as well as the correlation functions of force and torque fluctuations to flow field fluctuations. It is found, that the mean values of streamwise force (drag) and wall normal force (lift) are positive, while the mean spanwise torque is negative. The mean values are to a large extent produced at the top region of the particle surface. The intensity of the particle force fluctuations is significantly larger in the large-sphere case, while the trend differs for the fluctuations of the individual components of the torque. For the present simulations, time scales of force and torque fluctuations are of the order of outer flow units. In agreement with this, the correlation of particle force and torque fluctuations and flow field fluctuations have length scales comparable to the channel depth. Flow structures related to force and torque fluctuations appear to travel with a convection velocity of 46% to 71% of the bulk velocity in the small sphere case. Lowest convection velocities were obtained in the large sphere case, which agrees with the finding in the literature that roughness reduces the convection velocity of structures. Some aspects of force and torque on the particles can be explained by simplified considerations that link flow structures to particle force and torque

## 6.2 Sediment transport in open channel flow

Sediment transport was studied based on the simulations of flow over fixed and mobile eroding spheres. First, several approaches were assessed, to predict the onset of sediment erosion by force and torque on fixed spheres. It was found, that criteria based on high drag, lift or spanwise torque might lead to different results. In contrast to this, the criteria based on drag are, for the present cases, equivalent to more elaborate criteria such as the force tangential to the plane of support as well as the moment around the axis of support. Next, conditionally averaged time-signals of drag, lift and spanwise torque on fixed particles were studied. As conditioning criteria served drag, lift and spanwise torque with a threshold of five standard deviation higher, in case of torque lower, than the mean. It was found, that the shape of the conditionally averaged time-signals heavily depend on the conditioning criteria. In particular, the conditionally averaged time-signals resemble in shape the correlation (in time) between the respective conditioning quantity and the respective averaging quantity. Instantaneous flow fields, conditioned to high drag on fixed particles, often exhibit a pair of high speed and low speed streaks in the vicinity of the particle. Also, strong vortices as identified by highly negative pressure fluctuations are observed near-by the particle and the region around the particle is often characterised by high turbulence activity. The conditionally averaged flow field around particles with high drag show large elongated structures of positive streamwise velocity fluctuations above the particles. The conditionally averaged velocity fluctuations in wall-normal are directed towards the particle while in spanwise direction they are directed away from the particle. As in the case of time signals, the conditionally averaged flow field resembles in shape the correlation between flow field and particle drag. This indicates, that flow structures which might be related to the onset of sediment transport do not differ much from structures that are commonly related to force events.

The potential for sediment erosion of fixed spheres can be assessed by a Shields number based on

instantaneous lift. For the present cases, this approach predicts lower critical Shields number for the large sphere case which is in contrast to experimental evidence in the literature. A possible explanation of this discrepancy is that in this approach possible collective effects during erosion are not taken into account. The few direct numerical simulation of erosion events with mobile particles indicate that these collective effects might play a role in the present cases. The numerical simulation of erosion events with mobile particle further show, that during erosion, particles are strongly accelerated in wall-normal direction and along their spanwise axis. Wall normal velocities of the order of the friction velocity are reached within one or two outer flow units. The few studied flow fields during erosion events for the small sphere case exhibit similar flow structures as the flow fields related to high drag events in the fixed sphere case.

## 6.3 Recommendation of future work

This thesis provides high-fidelity data of two simulations of open channel flow over fixed spheres within the transitionally rough and fully rough regime. Additional experimental or numerical studies are needed to further explore in particular the fully-rough flow regime and draw conclusions on the effect of the Reynolds number. In future studies, it would be highly beneficial to consider setups in a parameter range that overcomes some problems of existing studies. Most works related to flow over fixed spheres or to the onset of sediment erosion considered small aspect ratios of channel height to particle diameter. Thus, often the flow has to be considered as flow over large obstacles rather than flow over a rough surface. However, a large aspect ratio of channel height to particle diameter is required to establish a certain level of independence of the turbulent flow from the geometry of the wall and thus allow for generalisation of the results. Note that, Jimnez (2004) proposes channel heights of more than 50 characteristic particle sizes. Furthermore, experimental studies are needed that realise large aspect ratios of channel width to channel height. Some evidence exists, that the aspect ratio of 5 proposed by (Nezu & Nakagawa (1993)) to assume negligible effects of the wall in the channel centre is to small and higher aspect ratio are needed. The parameter range for future studies outlined above poses a challenge to both, experimental and numerical studies.

The present study identified a need for data related to force and torque on fixed particles immersed in a layer of spheres. In particular additional experiments at higher Reynolds numbers would be highly beneficial to assess scaling aspects of force and torque and related structures. It might be preferable if direct measurement techniques of force (and torque) would be utilised in such studies. This might be the most accurate method to measure force the more as it was found here, that the distribution of stresses which contribute to force and torque vary strongly across the particles surfaces. Thus measurement techniques that estimate the force on a particle based on single point measurements along the particle surface might be subject to large uncertainties. More insight to scaling aspects based on existing data, could be gained from analysing flow structures related to force and torque on a square surface element in smooth wall flows. Clearly, the force and torque on a particle involves a larger range of complexity and differ in particular with respect to the effect of pressure from the force and torque on a square surface element.

With respect to the studies of sediment erosion of mobile particles, additional experimental and numerical studies are needed. A deeper understanding of the processes involved can only be gained by providing enough samples of erosion events to carry out statistical analysis. Experimentally, the approach of Hofland *et al.* (2005) appears to be an attractive option to reach

this goal. The author used a spring to move a particle into its initial position after erosion by rotational motion. Furthermore, the spring was used to trigger the recording of the erosion movement. Numerically, the simulation of the erosion of might be seen suited to reduce the numerical costs as several, only weakly correlated, erosion events can be studied within one simulation. However, before considering additional numerical simulations of similar erosion events, future studies should clarify the influence of the contact model on the sediment erosion.

In the future, the simulations of sediment transport presented here should be further analysed to understand some aspects of the flow and particle statistics presented. Questions of interest, which were only addressed briefly here, are the effect of the moving phase on the turbulence structure, possible explanations of the velocity lag of the particle and the higher correlation between streamwise and wall-normal particle velocities compared to fluid velocity. Also a comparison of erosion events of particles at rest in simulation with and without sediment transport would be beneficial to reveal if the erosion events are of similar nature or if they differ.

# Bibliography


1958 Secondary currents in straight channels. *Eos, Transactions American Geophysical Union* **39** (6), 1085–1088.

Akiki, G., Jackson, T. L. & Balachandar, S. 2017 Pairwise interaction extended point-particle model for a random array of monodisperse spheres. *Journal of Fluid Mechanics* **813**, 882–928.

Amir, M., Nikora, V. I. & Stewart, M. T. 2014 Pressure forces on sediment particles in turbulent open-channel flow: a laboratory study. *Journal of Fluid Mechanics* **757**, 458497.

Bagchi, Prosenjit & Balachandar, S 2003 Effect of turbulence on the drag and lift of a particle. *Physics of fluids* **15** (11), 3496–3513.

Balachandar, Sivaramakrishnan 1989 Particle coagulation in homogeneous turbulence. .

Balachandar, S & Maxey, MR 1989 Methods for evaluating fluid velocities in spectral simulations of turbulence. *Journal of Computational Physics* **83** (1), 96–125.

Basset, A. 1888 On the motion of a sphere in a viscous liquid. *Phil. Trans. Roy. Soc. London* **179**, 43–63.

Batchelor, G. K. 1976 Brownian diffusion of particles with hydrodynamic interaction. *Journal of Fluid Mechanics* **74** (1), 129.

Bathurst, J. C., Hey, R. D. & Thorne, C. R. 1985 *Theoretical aspects of flow resistance in Gravel-Bed Rivers*. John Wiley, New York.

Bayazit, M. 1976 Free surface flow in a channel of large relative roughness. *Journal of Hydraulic Research* **14** (2), 115–126.

Boussinesq, Joseph 1877 *Essai sur la théorie des eaux courantes*. Impr. nationale.

Bradshaw, P 2000 A note on critical roughness height and transitional roughness. *Physics of Fluids* **12** (6), 1611–1614.

Brayshaw, A. C. 1985 Bed microtopography and entrainment thresholds in gravel-bed rivers. *GSA Bulletin* **96** (2), 218.

Brayshaw, C. A., Frostick, L. E. & Reid, I. 1983 The hydrodynamics of particle clusters and sediment entrapment in coarse alluvial channels. *Sedimentology* **30** (1), 137–143.

Buffington, John M 1999 The legend of af shields. *Journal of Hydraulic Engineering* **125** (4), 376–387.

Buffington, John M & Montgomery, David R 1997 A systematic analysis of eight decades of incipient motion studies, with special reference to gravel-bedded rivers. *Water Resources Research* **33** (8), 1993–2029.

Cameron, S. M., Nikora, V. I. & Coleman, S. E. 2008 Double-averaged velocity and stress distributions for hydraulically-smooth and transitionally-rough turbulent flows. *Acta Geophysica* **56** (3), 642–653.

Charru, François, Larrieu, E, Dupont, Jean-Baptiste & Zenit, Roberto 2007 Motion of a particle near a rough wall in a viscous shear flow. *Journal of Fluid Mechanics* **570**, 431.

Cherukat, P., Na, Y., Hanratty, T.J. & McLaughlin, J.B 1998 Direct numerical simulation of a fully developed turbulent flow over a wavy wall. *Theoretical and Computational Fluid Dynamics* **11** (2), 109–134.

Choi, Haecheon & Moin, Parviz 1990 On the space-time characteristics of wall-pressure fluctuations. *Physics of Fluids A: Fluid Dynamics* **2** (8), 1450–1460.

Clemens, Chan-Braun, García-Villalba, M. & Uhlmann, M. 2011 Force and torque acting on particles in a transitionally rough open-channel flow. *Journal of Fluid Mechanics* **684**, 441–474.

Colebrook, Cyril Frank, Blench, T, Chatley, H, Essex, EH, Finniecome, JR, Lacey, G, Williamson, J & Macdonald, GG 1939 Correspondence. turbulent flow in pipes, with particular reference to the transition region between the smooth and rough pipe laws.(includes plates). *Journal of the Institution of Civil engineers* **12** (8), 393–422.

Coleman, S. E., Nikora, V. I. & Aberle, J. 2011 Interpretation of alluvial beds through bed-elevation distribution moments. *Water Resources Research* **47** (11).

Darcy, H. 1857 Recherches experimentales relatives au mouvement de l'eau dans les tuyaux. *Paris: Mallet-Bachelier* p. 268.

Davidson, Peter Alan 2015 *Turbulence: an introduction for scientists and engineers*. Oxford university press.

De Angelis, V., Lombardi, P. & Banerjee, S. 1997 Direct numerical simulation of turbulent flow over a wavy wall. *Physics of Fluids* **9** (8), 2429–2442.

Derksen, J. J. & Larsen, R. A. 2011 Drag and lift forces on random assemblies of wall-attached spheres in low-reynolds-number shear flow. *Journal of Fluid Mechanics* **673**, 548573.

Detert, Martin, Nikora, V & Jirka, Gerhard H 2010 Synoptic velocity and pressure fields at the water-sediment interface of streambeds. *Journal of Fluid Mechanics* **660**, 55.

Dwivedi, Ambuj, Melville, Bruce & Shamseldin, Asaad Y 2010 Hydrodynamic forces generated on a spherical sediment particle during entrainment. *Journal of Hydraulic Engineering* **136** (10), 756–769.

Einstein, H. A. & El-Samni, E. A. 1949 Hydrodynamic forces on a rough wall. *Reviews of Modern Physics* **21** (3), 520–524.

Faxn, H. 1922 Der widerstand gegen die bewegung einer starren kugel in einer zhen flssigkeit, die zwischen zwei parallelen ebenen wnden eingeschlossen ist. *Ann. Phys* **373**, 89–119.

Fenton, D. J. & Abbott, E. J. 1977 Initial movement of grains on a stream bed: the effect of relative protrusion. *Proceedings of the Royal Society of London A: Mathematical, Physical and Engineering Sciences* **352** (1671), 523–537.

Flores, O & Jimeńez, J 2006 Effect of wall-boundary disturbances on turbulent channel flows. *Journal of Fluid Mechanics* **566**, 357376.

Frisch, Uriel 1995 *Turbulence: the legacy of AN Kolmogorov*. Cambridge university press.

Garcia, Marcelo 2008 Sedimentation engineering: processes, measurements, modeling, and practice. American Society of Civil Engineers.

Gatignol, R. 1983 The faxen formulae for a rigid particle in an unsteady non-uniform stokes flow. *J. Mec. Theor. Appl.* **1(2)**, 143–160.

Glowinski, Roland, Pan, T-W, Hesla, Todd I & Joseph, Daniel D 1999 A distributed lagrange multiplier/fictitious domain method for particulate flows. *International Journal of Multiphase Flow* **25** (5), 755–794.

Grass, AJ, Stuart, RJ & Mansour-Tehrani, M 1991 Vortical structures and coherent motion in turbulent flow over smooth and rough boundaries. *Philosophical Transactions of the Royal Society of London. Series A: Physical and Engineering Sciences* **336** (1640), 35–65.

Hagen, G. 1854 Uber den einfluss der temperatur auf die bewegung des wassers in rohren. *Math. Abh. Akad. Wiss Berlin* pp. 17–98.

Hall, D. 1988 Measurements of the mean force on a particle near a boundary in turbulent flow. *Journal of Fluid Mechanics* **187**, 451466.

Hofland, Bas, Battjes, Jurjen A & Booij, Robert 2005 Measurement of fluctuating pressures on coarse bed material. *Journal of Hydraulic Engineering* **131** (9), 770–781.

Hoyas, Sergio & Jiménez, Javier 2006 Scaling of the velocity fluctuations in turbulent channels up to re $\tau$= 2003. *Physics of fluids* **18** (1), 011702.

Ikeda, Syunsuke 1982 Incipient motion of sand particles on side slopes. *Journal of the Hydraulics Division* **108** (1), 95–114.

Ikeda, T. & Durbin, P. A. 2007 Direct simulations of a rough-wall channel flow. *Journal of Fluid Mechanics* **571**, 235263.

Ji, C., Munjiza, A., Avital, E., Ma, J. & Williams, J. J. R. 2013 Direct numerical simulation of sediment entrainment in turbulent channel flow. *Physics of Fluids* **25** (5), 056601, arXiv: https://doi.org/10.1063/1.4807075.

Jimeńez, J. 2004 Turbulent flows over rough walls. *Annual Review of Fluid Mechanics* **36** (1), 173–196.

Jiménez, Javier, Hoyas, Sergio, Simens, Mark P & Mizuno, Yoshinori 2010 Turbulent boundary layers and channels at moderate reynolds numbers. *Journal of Fluid Mechanics* **657**, 335.

Jiménez, Javier & Pinelli, Alfredo 1999 The autonomous cycle of near-wall turbulence. *Journal of Fluid Mechanics* **389**, 335–359.

Jimnez, Javier & Moin, Parviz 1991 The minimal flow unit in near-wall turbulence. *Journal of Fluid Mechanics* **225**, 213240.

Johansson, Arne V, Her, Jen-Yuan & Haritonidis, Joseph H 1987 On the generation of high-amplitude wall-pressure peaks in turbulent boundary layers and spots. *Journal of Fluid Mechanics* **175**, 119–142.

Kaftori, D, Hetsroni, G & Banerjee, S 1995 Particle behavior in the turbulent boundary layer. ii. velocity and distribution profiles. *Physics of Fluids* **7** (5), 1107–1121.

Kennedy, John F 1995 The albert shields story. *Journal of Hydraulic Engineering* **121** (11), 766–772.

Kidanemariam, A. G. & Uhlmann, M. 2017 Formation of sediment patterns in channel flow: minimal unstable systems and their temporal evolution. *Journal of Fluid Mechanics* **818**, 716–743.

Kiger, KT & Pan, C 2002 Suspension and turbulence modification effects of solid particulates on a horizontal turbulent channel flow. *J. Turbul* **3** (19), 1–17.

Kim, John 1989 On the structure of pressure fluctuations in simulated turbulent channel flow. *Journal of Fluid Mechanics* **205**, 421–451.

Kim, J., Moin, P. & Moser, R. 1987 Turbulence statistics in fully developed channel flow at low reynolds number. *Journal of Fluid Mechanics* **177**, 133–166.

Kirchner, J. W., Dietrich, W. E., Iseya, F. & Ikeda, H. 1990 The variability of critical shear stress, friction angle, and grain protrusion in water-worked sediments. *Sedimentology* **37** (4), 647–672.

Koll, Katinka 2006 Parameterisation of the vertical velocity profile in the wall region over rough surfaces. , vol. 1.

Kolmogorov, Andrey Nikolaevich 1941 The local structure of turbulence in incompressible viscous fluid for very large reynolds numbers. *Cr Acad. Sci. URSS* **30**, 301–305.

Komori, Satoru, Nagaosa, Ryuichi, Murakami, Yasuhiro, Chiba, Satoshi, Ishii, Katsuya & Kuwahara, Kunio 1993 Direct numerical simulation of threedimensional openchannel flow with zeroshear gasliquid interface. *Physics of Fluids A: Fluid Dynamics* **5** (1), 115–125.

Lee, H. & Balachandar, S. 2010 Drag and lift forces on a spherical particle moving on a wall in a shear flow at finite re. *Journal of Fluid Mechanics* **657**, 89125.

Leonardi, S., Orlandi, P. & Antonia, R. A. 2007 Properties of d- and k-type roughness in a turbulent channel flow. *Physics of Fluids* **19** (12), 125101.

Ligrani, Phillip M & Moffat, Robert J 1986 Structure of transitionally rough and fully rough turbulent boundary layers. *Journal of Fluid Mechanics* **162**, 69–98.

Lobkovsky, Alexander E, Orpe, Ashish V, Molloy, Ryan, Kudrolli, Arshad & Rothman, Daniel H 2008 Erosion of a granular bed driven by laminar fluid flow. *arXiv preprint arXiv:0805.0086* .

Loth, E 2008 Computational fluid dynamics of bubbles, drops and particles. *Cambridge: Cambridge* **679**.

Lucci, Francesco, Ferrante, Antonino & Elghobashi, Said 2010 Modulation of isotropic turbulence by particles of taylor length-scale size. *Journal of Fluid Mechanics* **650**, 5.

Manes, C., Pokrajac, Dubravka & McEwan, Ian Kenneth 2007 Double averaged open channel flows with small relative submergence. *Journal of Hydraulic Engineering* **133** (8), 896–904.

Marusic, Ivan, McKeon, Beverley J, Monkewitz, Peter A, Nagib, Hassan M, Smits, Alexander J & Sreenivasan, Katepalli R 2010 Wall-bounded turbulent flows at high reynolds numbers: recent advances and key issues. *Physics of Fluids* **22** (6), 065103.

Maxey, M. R. & Riley, J. R. 1983 Equation of motion for a small rigid sphere in a nonuniform flow. *The Physics of Fluids* **26** (4), 883–889.

Mazzuoli, M. & Uhlmann, M. 2017 Direct numerical simulation of open-channel flow over a fully rough wall at moderate relative submergence. *Journal of Fluid Mechanics* **824**, 722–765.

Mehdi, Faraz, Klewicki, J. C. & White, C. M. 2013 Mean force structure and its scaling in rough-wall turbulent boundary layers. *Journal of Fluid Mechanics* **731**, 682712.

Milici, B., De Marchis, M., Sardina, G. & Napoli, E. 2014 Effects of roughness on particle dynamics in turbulent channel flows: a dns analysis. *Journal of Fluid Mechanics* **739**, 465478.

Miyake, Yutaka, Tsujimoto, Koichi & Nakaji, Masaru 2001 Direct numerical simulation of rough-wall heat transfer in a turbulent channel flow. *International Journal of Heat and Fluid Flow* **22** (3), 237–244.

Moin, Parviz & Mahesh, Krishnan 1998 Direct numerical simulation: a tool in turbulence research. *Annual review of fluid mechanics* **30** (1), 539–578.

Mollinger, AM & Nieuwstadt, FTM 1996 Measurement of the lift force on a particle fixed to the wall in the viscous sublayer of a fully developed turbulent boundary layer. *Journal of Fluid Mechanics* **316**, 285–306.

Muste, M, Yu, K, Fujita, I & Ettema, R 2009 Two-phase flow insights into open-channel flows with suspended particles of different densities. *Environmental fluid mechanics* **9** (2), 161–186.

Naden, Pamela 1987 An erosion criterion for gravel-bed rivers. *Earth Surface Processes and Landforms* **12** (1), 83–93.

Nagano, Yasutaka, Hattori, Hirofumi & Houra, Tomoya 2004 Dns of velocity and thermal fields in turbulent channel flow with transverse-rib roughness. *International Journal of Heat and Fluid Flow* **25** (3), 393–403.

Nagib, Hassan M. & Chauhan, Kapil A. 2008 Variations of von krmn coefficient in canonical flows. *Physics of Fluids* **20** (10), 1015–18.

Nakagawa, Hiroji & Nezu, Iehisa 1977 Prediction of the contributions to the reynolds stress from bursting events in open-channel flows. *Journal of fluid mechanics* **80** (1), 99–128.

Nakagawa, H. & Tsujimoto, T. 1980 A stochastic model for bed load transport and its applications to alluvial phenomena. *Tech. Rep.*.

Nakagawa, Hiroji, Tsujimoto, Tetsuro & Shimizu, Yoshihiko 1991 Turbulent flow with small relative submergence. In *Fluvial Hydraulics of Mountain Regions*, pp. 33–44. Berlin, Heidelberg: Springer Berlin Heidelberg.

Nezu, I. & Nakagawa, H. 1993 *Turbulence in Open-Channel Flows*. Rotterdam Balkema.

Niño, Y. & García, M. H. 1996 Experiments on particleturbulence interactions in the nearwall region of an open channel flow: implications for sediment transport. *Journal of Fluid Mechanics* **326**, 285319.

Nikora, Vladimir 2007 3 hydrodynamics of gravel-bed rivers: scale issues. *Developments in Earth Surface Processes* **11**.

Nikora, Vladimir, Koll, Katinka, McEwan, Ian, Mclean, Stephen & Dittrich, Andreas 2004 Velocity distribution in the roughness layer of rough-bed flows. *Journal of Hydraulic Engineering-asce - J HYDRAUL ENG-ASCE* **130**.

Nikora, Vladimir, Koll, K., Mclean, S. R., Ditrich, A. & Aberle, J. 2002 *Zero-plane displacement for rough-bed open-channel flows.*, pp. 83–92.

Nikora, V. I., Goring, D., McEwan, I. & Griffiths, G. 2001 Spatially averaged open-channel flow over rough bed. *Journal of Hydraulic Engineering* **127** (2), 123–133.

Nikora, V. I., Goring, D. G. & Biggs, B. J. F. 1998 On gravel-bed roughness characterization. *Water Resources Research* **34** (3), 517–527.

Nikora, V. I. & McLean, S. R. 2001 Environmental flows over rough beds: a spatial averaging approach. *Proc, 3rd Int. Symp, on Environmental Hydraulics* .

Nikuradse, J. 1933 Stromungsgesetze in rauhen rohren. *VDI-Forsch* **361**.

Niño, Yarko, Lopez, Fabian & Garcia, Marcelo 2003 Threshold for particle entrainment into suspension. *Sedimentology* **50** (2), 247–263.

Orlandi, P. & Leonardi, S. 2008 Direct numerical simulation of three-dimensional turbulent rough channels: parameterization and flow physics. *Journal of Fluid Mechanics* **606**, 399415.

Orlandi, P., Leonardi, S., Tuzi, R. & Antonia, R. A. 2003 Direct numerical simulation of turbulent channel flow with wall velocity disturbances. *Physics of Fluids* **15** (12), 3587–3601.

Oseen, C. 1911 *ber die Stoke'sche Formel und über eine verwandte Aufgabe in der Hydrodynamik*. Almqvist & Wiksell.

Oseen, C. 1913 *eber den Gltigkeitsbereich der Stokesschen Widerstandsformel*. Arkiv för Matematik, Astronomi och Fysik. Friedlnder.

Pan, Y & Banerjee, S 1997 Numerical investigation of the effects of large particles on wall-turbulence. *Physics of Fluids* **9** (12), 3786–3807.

Papanicolaou, AN, Diplas, P, Evaggelopoulos, N & Fotopoulos, S 2002 Stochastic incipient motion criterion for spheres under various bed packing conditions. *Journal of Hydraulic Engineering* **128** (4), 369–380.

Peskin, Charles 1973 Flow patterns around heart valves: a digital computer method for solving the equations of motion. *IEEE transactions on biomedical engineering* (4), 316–317.

Peysson, Y, Ouriemi, Malika, Medale, M, Aussillous, P & Guazzelli, E 2009 Threshold for sediment erosion in pipe flow. *International Journal of Multiphase Flow* **35** (6), 597.

Pimenta, MM, Moffat, RJ & Kays, WM 1975 The turbulent boundary layer: An experimental study of the transport of momentum and heat with the effect of roughness[interim report] .

Poggi, D, Porporato, A & Ridolfi, L 2003 Analysis of the small-scale structure of turbulence on smooth and rough walls. *Physics of Fluids* **15** (1), 35–46.

Poisson, S. 1831 Memoire sur les mouvements simultanes d un pendule et de l air. *Environnemant. Mem. V Acad. des Sci. Paris* **9**, 521–523.

Pokrajac, Dubravka & Manes, Costantino 2009 Velocity measurements of a free-surface turbulent flow penetrating a porous medium composed of uniform-size spheres. *Transport in porous media* **78** (3), 367.

Pope, S. B. 2000 *Turbulent Flows*. Cambridge University Press.

Quadrio, Maurizio & Luchini, Paolo 2003 Integral space–time scales in turbulent wall flows. *Physics of fluids* **15** (8), 2219–2227.

Raupach, Michael R, Antonia, Robert A & Rajagopalan, Sundara 1991 Rough-wall turbulent boundary layers .

Reynolds, Osborne 1883 An experimental investigation of the circumstances which determine whether the motion of water shall be direct or sinuous, and of the law of resistance in parallel channels. *Philosophical Transactions of the Royal society of London* (174), 935–982.

Reynolds, Osborne 1895 On the dynamical theory of incompressible viscous fluids and the determination of the criterion. *Philosophical transactions of the royal society of london.(a.)* (186), 123–164.

Rice, S. & Church, M. 1998 Grain size along two gravel-bed rivers: statistical variation, spatial pattern and sedimentary links. *Earth Surface Processes and Landforms* **23** (4), 345–363.

Richardson, Lewis Fry 2007 *Weather prediction by numerical process*. Cambridge university press.

Righetti, M & Romano, Giovanni Paolo 2004 Particle-fluid interactions in a plane near-wall turbulent flow. *Journal of Fluid Mechanics* **505**, 93.

Robert, A. 2003 *River processes: An introduction to fluvial dynamics*. Routledge.

Roma, Alexandre M, Peskin, Charles S & Berger, Marsha J 1999 An adaptive version of the immersed boundary method. *Journal of computational physics* **153** (2), 509–534.

Rouse, Hunter 1963 *History of Hydraulics, by Hunter Rouse and Simon Ince*. Dover Publications.

Schlichting, H. 1936*a* Experimentelle untersuchungen zum rauhigkeitsproblem. *Ing Arch* **7**, 1–34.

Schlichting, H. 1936*b* Grenzschicht-theorie. *Verlag G. Braun.* **5**, 20.

Shields, A. 1936 Anwendung der aehnlichkeitsmechanik und der turbulenzforschung auf die geschiebebetrieb. mitteilungen der preussischen versuchsanstalt fur wasserbau und schiffbau **Heft 26**.

Shockling, MA, Allen, JJ & Smits, AJ 2006 Roughness effects in turbulent pipe flow. *Journal of Fluid Mechanics* **564**, 267.

Singh, K M., Sandham, N. D. & Williams, J. J. R. 2007 Numerical simulation of flow over a rough bed. *Journal of Hydraulic Engineering* **133** (4), 386–398.

Spalart, Philippe R 1988 Direct simulation of a turbulent boundary layer up to r $\theta$= 1410. *Journal of fluid mechanics* **187**, 61–98.

Stokes, G. 1845 On the theories of internal friction of the fluids in motion. *Trans. Cambridge Philos. Soc.* **8**, 287–319.

Sutherland, A. J. 1967 Proposed mechanism for sediment entrainment by turbulent flows. *Journal of Geophysical Research* **72** (24), 6183–6194.

Tait, J. S., Willetts, B. B. & Maizels, J. K. 1992 Laboratory observations of bed armouring and changes in bedload composition. *Dynamics of Gravel-bed Rivers* **20** (1), 205–225.

Taniere, A, Oesterle, B & Monnier, JC 1997 On the behaviour of solid particles in a horizontal boundary layer with turbulence and saltation effects. *Experiments in Fluids* **23** (6), 463–471.

Tennekes, H & Lumley, JL 1972 *Turbulence MIT Press*. Cambridge.

Townsend, A. A. 1965 The response of a turbulent boundary layer to abrupt changes in surface conditions. *Journal of Fluid Mechanics* **22** (4), 799822.

Uhlmann, M. 2005 An immersed boundary method with direct forcing for the simulation of particulate flows. *Journal of Computational Physics* **209**, 448–476.

Uhlmann, M. 2006 Direct numerical simulation of sediment transport in a horizontal channel. *Tech Rep. 1088* pp. 1135–9420.

Uhlmann, Markus & Fröhlich, Jochen 2008 Transport of heavy spherical particles in horizontal channel flow. In *High Performance Computing in Science and Engineering07*, pp. 351–369. Springer.

Van Rijn, Leo C & others 1993 *Principles of sediment transport in rivers, estuaries and coastal seas*, , vol. 1006. Aqua publications Amsterdam.

Vanoni, V. A. 1975 *Sedimentation engineering: Manuals and reports on engineering practice*. ASCE, New York, USA.

Verzicco, R & Orlandi, P 1996 A finite-difference scheme for three-dimensional incompressible flows in cylindrical coordinates. *Journal of Computational Physics* **123** (2), 402–414.

Yalin, Mehmet Selim 1977 *Mechanics of Sediment Transport: 2d Ed*. Pergamon Press.

Yang, D. & Shen, L. 2010 Direct-simulation-based study of turbulent flow over various waving boundaries. *Journal of Fluid Mechanics* **650**, 131180.

Zeng, Lanying, Balachandar, S, Fischer, Paul & Najjar, Fady 2008 Interactions of a stationary finite-sized particle with wall turbulence. *Journal of Fluid Mechanics* **594**, 271.

Zhou, Jigen, Adrian, Ronald J & Balachandar, S 1996 Autogeneration of near-wall vortical structures in channel flow. *Physics of Fluids* **8** (1), 288–290.